The Boeing Company
Engineering Test and Technology
Boeing Research and Technology

CLEEN Phase III Sustainable Aviation Fuels Project: UDRI Phase 1 Test Report

FAA/Boeing Continuous Lower Energy, Emissions, and Noise (CLEEN)
Phase III Technology Demostration Program

Cooperative Agreement # 693KA9 – 21 – T – 00001
November 3, 2023

Prepared for:
Arthur Orton
CLEEN Phase III Program Manager
Federal Aviation Administration
800 Independence Ave, S.W.
Washington, DC 20591

Contracts Administrator: Adam Iwanow
Phone Number: (314) 451-6270
Email: adam.m.iwanow@boeing.com

Presented by:
Ilya Kosilkin (PI) Phone Number: (425) 239-9481 Email: ilya.v.kosilkin@boeing.com

The Boeing Company
PO Box 516, M/C S102-2067, Saint Louis, MO 63166

SEALANTS AND ELASTOMERS LABORATORY
NONSTRUCTURAL MATERIALS DIVISION
300 College Park • Dayton Ohio 45469-7751
937.229.2877 FAX 937.229.2503

University of Dayton Research Institute

Report No. UDR-TR-2023-77

18 September 2023

Material Compatibility Testing for CLEEN III Phase 1 Summary Report

Report No. UDR-TR-2023-77
Proposal No. R-25894
PO No. 2145658

Prepared For:

The Boeing Company
Ilya Kosilkin

Prepared By:

John L. Graham, Ph.D.
Distinguished Research Engineer

ANAB ACCREDITED ISO/IEC 17025 TESTING LABORATORY
Certificate # L2021-1 Testing

ISO 9001 Registered Quality System

Unlimited Distribution

BACKGROUND

In 2003 the University of Dayton Research Institute (UDRI) began a program with the Air Force Research Laboratory (AFRL) in support of the United States Department of Defense (U.S. DoE) Flexible JP-8 Program. This program was designed to investigate the development and fielding of jet turbine fuels derived from non-petroleum sources such as coal and biomass. A major concern with these fuels was that they were often compositionally different than conventional fuels and that they may not be compatible with all of the materials in a modern fuel system that have evolved to accommodate petroleum distillate fuels. Of primary concern was the role of aromatic components which were known to interact with fuel system elastomers and these components were often absent from the alternative jet turbine fuel being developed. While there was considerable evidence that the levels of aromatics in jet turbine fuel could have a significant impact on material compatibility as well as fuel performance, there was little detailed information on the specific role of aromatics in material compatibility in general and its impact on the performance of O-ring seals in particular.

The initial effort executed by UDRI in support of AFRL was to develop a fundamental understanding of exactly how jet turbine fuels in general, and the aromatics in particular, interact with polymeric fuel system materials. This work was successful and a detailed understanding of how all the major fuel components interact with fuel systems polymers. Furthermore, a unique set of laboratory, data analysis, and computational tools were developed to support this research. In 2006 these research tools were employed as testing tools to support the first flight tests of 50% alternative fuel blends and later were used as screening tools as part of the Tier 2 and Tier 3 material compatibility testing protocol developed in support of ASTM D4054.

In 2009 UDRI began an effort in support of The Boeing Company's participation in the FAA's CLEEN program. This effort examined the fluid compatibility of synthetic paraffinic kerosene (SPK) fuels and SPK/Jet A fuel blends with selected polymeric materials found in commercial aircraft. This effort also expanded earlier work which suggested that SPK fuel that were high in cycloparaffins could offer enhanced material compatibility and reduced reliance on aromatic components. (See J. Graham, T. Rahmes, M. Kay, J. Belières, J. Kinder, S. Millett, J. Ray, W. Vannice, J. Trela, "Evaluating the Impact of SPK Fuels and Fuel Blends on Non-metallic Materials used in Commercial Aircraft Fuel Systems," DTFA WA-10-C-0030, Final Report, The Boeing Company, Seattle, WA, December 2013.)

In 2013 UDRI began a series of programs for the Defense Logistics Agency (DLA) to examine the impact of the intermittent use of SPK/JP-8 fuel blends on the performance of O-ring seals. This work expanded the testing and evaluation capabilities to include component-level work under representative service conditions and resulted in the development of new test methods to evaluate the effects of alterative jet turbine fuels on the short-term behavior of O-rings seals; principally the changes that occur within the first 7 days following the switching between a conventional jet turbine fuel and a

low-aromatic SPK/JP-8 fuel blend (fuel switch-loading). These results showed that O-ring seals were very robust and should tolerate a low-aromatic SPK/JP-8 fuel blends until the seals are near the end of their service life.

The body of previous work indicated that nitrile rubber O-ring seals will likely present the greatest challenge to the implementation of a low-aromatic SPK/JP-8 fuel blends as this material shows the greatest response to changes in fuel composition. The primary objective of the proposed work was to generate appropriate data for understanding variability of properties of nitrile rubber with fuels containing various aromatic and cycloparaffinic content. This evaluation included an assessment of the fluid compatibility in a manner described in previous work, as well as chronic effects on function critical physical properties, most notably compression set and compressive stress relaxation and its influence on sealing performance. The collected data will be used to help establish a base line for material properties and to more precisely define conditions for testing with synthetic aviation fuels with high cycloparaffin content. Therefore, an additional objective of the project is to predict compatibility of zero aromatic, high cycloparaffin content synthetic fuels with new and aged aircraft fuel systems.

To accomplish the goals of this project a program consisting of 6 technical tasks as listed in Table 1 was proposed. As shown, these tasks are grouped as Tasks 1-3 in Phase 1 and 4-6 in Phase 2. The pages that follow summarize the results from Phase 1.

Table 1. Technical Tasks

Phase	Task	Description
1	1	Material Acquisition and Baseline Testing
	2	Compression, Compression Set, and Volume Swell
	3	Compression and Compression Set with fuel Switch-loading
2	4	Compression and Compression Set with Cycloparaffinic Fuels
	5	Optical Cell Leak Testing
	6	Compressive Stress Relaxation with Thermal Cycling

RESULTS AND DISCUSSION

Task 1 - Material Acquisition and Baseline Testing

In this Task the specific test materials were selected and acquired. This included a set of nitrile rubber O-rings qualified to AMS5315 and listed on the DLA QPL and a stock Jet A with mid-range aromatics (16.2%v/v). (Nota that unless otherwise noted all blends and concentrations are on a volume basis.) A portion of the Jet A was blended with Aromatic 100 to increase the aromatic content to 25%v/v, referred to as Jet A_25. A second portion of the Jet A was blended with a synthetic paraffinic kerosene (SPK) reduce the aromatic content to 4%v/v, referred to as Jet A_4. Together, these three fluids were considered representative of a Jet A with low, mid-range, and high aromatics.

In addition to the Jet A and Jet A blends described above a stock quantity of a cycloparaffinic kerosene (CPK-0) was supplied by Shell Aviation. CPK-0 is a predominantly cycloparaffinic blending stock produced using Shell's IH^2 process. In a manner like the Jet A, this stock of CPK-0 was blended as needed to compose fuels with various levels of CPK-0.

Once the test materials and fuels had been procured a series of baseline tests were performed as given in Table 2. This included type M hardness, tensile strength, ultimate elongation, and modulus. Note that the modulus was measured concurrently with the tensile strength and ultimate elongation.

The compression set was measured using conditions comparable to those specified for AMS5315 in ASTM D4054; 28 days at 160˚F with 25% compression. One variance is that these tests were performed using UDRI compression set fixtures that capture the O-rings in a model gland as shown in Figure 1. This provides data that is comparable with in-service conditions and the aged O-rings can be used for follow-on leak testing as described under Task 5.

The glass transition temperature was measured using thermomechanical analysis as described in ASTM E1545. Briefly, this evaluation was performed with a Mettler TMA/SDTA841e using a round-tip thermal expansion probe and an applied force of 0.02N. The sample temperature was ramped from -100˚C to +50˚C at 5˚C/min.

As a general characterization of the interaction between the test materials and fuels the volume swell at room temperature (75˚F) was measured for each of the test materials in each of the test fluids using an optical dilatometry method developed by UDRI and was previously used as part of the CLEEN I program. At the conclusion of this analysis the solubility of the major class fractions of the test fuels (paraffins, cycloparaffins, alkyl benzenes, and alkyl naphthalenes) was determined using GC-MS analysis of the swollen O-ring materials.

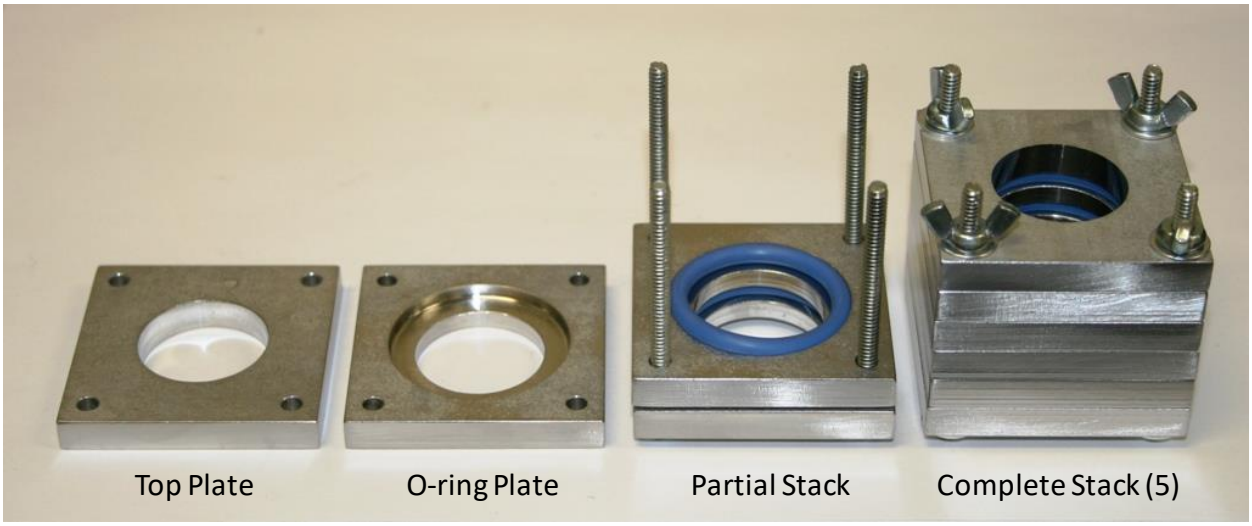

Figure 1. The UDRI compression set fixtures designed to constrain O-rings in a model gland to mimic the conditions of an internally pressurized seal and produce aged samples that will fit in the UDRI O-ring flow and optical cells.

Material Acquisition

A review of nitrile rubber O-rings qualified to AMS5315 present on the Qualified Products List (QPL) showed that only 3 products were available: N0602, N400 and 4457. Consequently, a stock supply of size 214-70 O-rings were obtained from each supplier for this project.

Baseline Physical Properties

The baseline physical properties of the as-received O-rings are summarized in Table 2 and Figures 2-7. Note that the hardness is reported as the average of 3 values and the tensile, elongation, and modulus are the average of 5 values. Note that the modulus is reported at 100% elongation and at the inflection point in the stress/strain curve. The 90% confidence intervals are also given.

Table 2. Baseline Physical Properties

Property	Method	O-ring	Value	90% CI
Hardness, Type M	ASTM D2240	N0602	76.5	0.2
		N400	79.0	0.7
		4457	77.1	0.6
Tensile, psi	ASTM D1414	N0602	1798	30.6
		N400	1997	49.9
		4457	1429	13.1
Elongation, %	ASTM D1414	N0602	315	5.6
		N400	264	6.3
		4457	234	4.3
Modulus, psi 100% EL	ASTM D1414	N0602	474	8.9
		N400	728	17.9
		4457	680	18.6
Modulus, psi Inflection	ASTM D1414	N0602	752	8.4
		N400	911	16.4
		4457	728	14.9

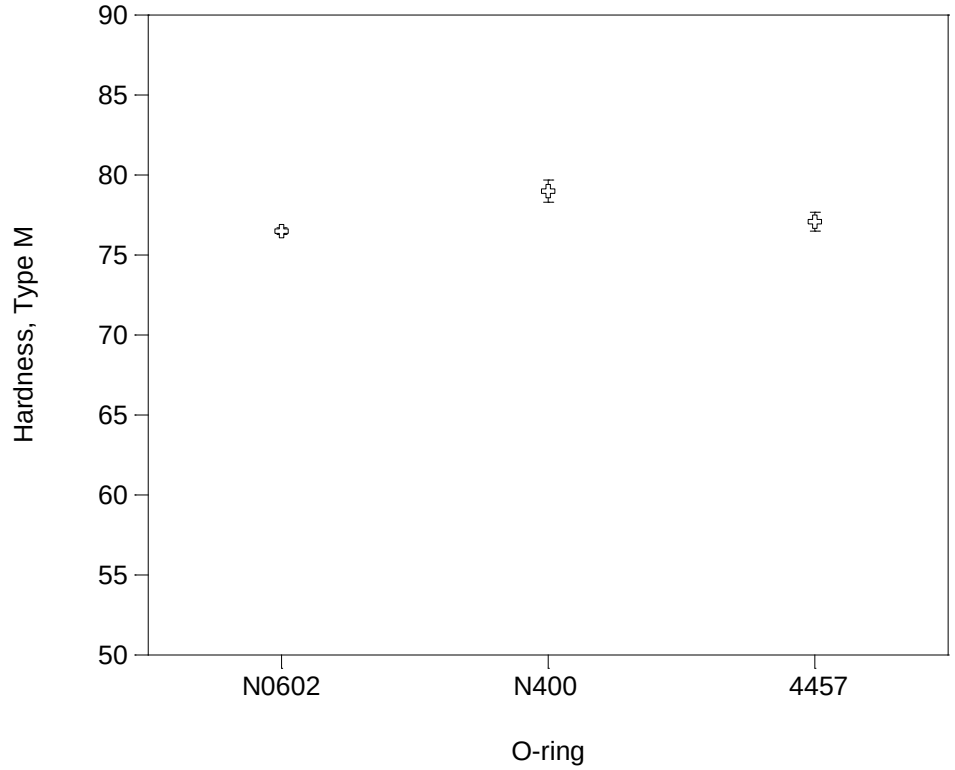

Figure 2. Baseline hardness (Type M) for the as-received O-rings.

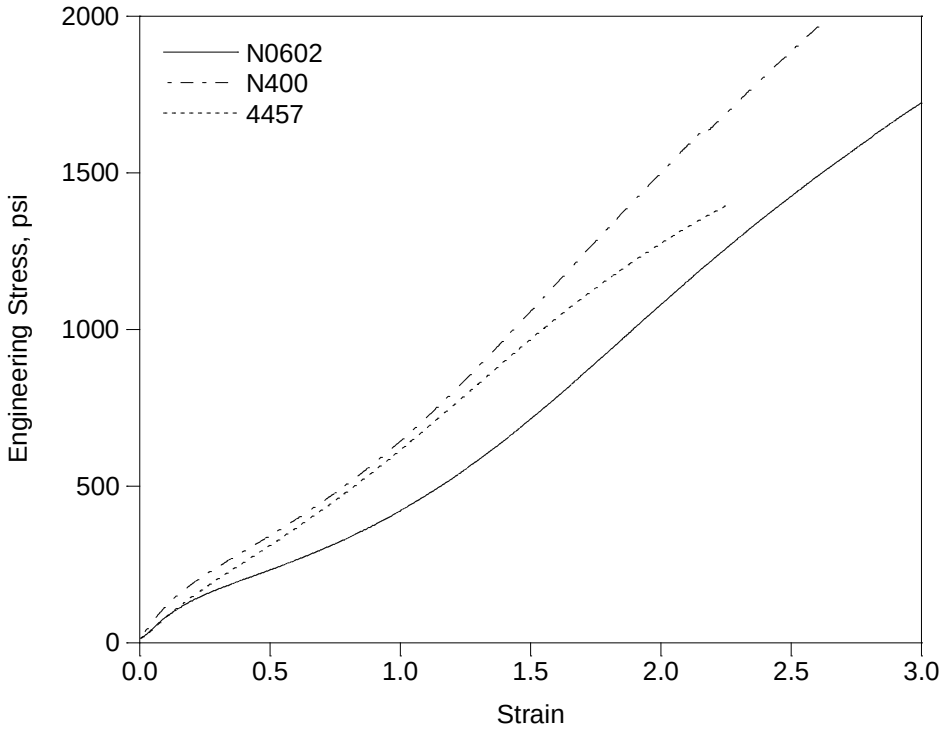

Figure 3. Engineering stress versus strain.

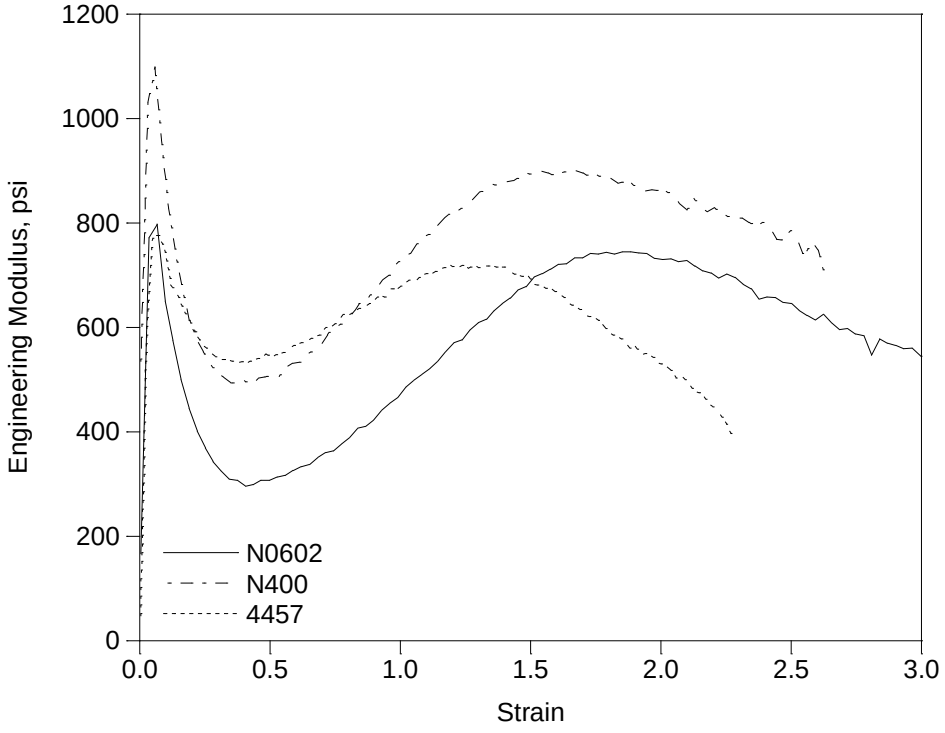

Figure 4. Engineering modulus versus strain. Note that the second peak corresponds to the primary inflection region in the stress/strain curve.

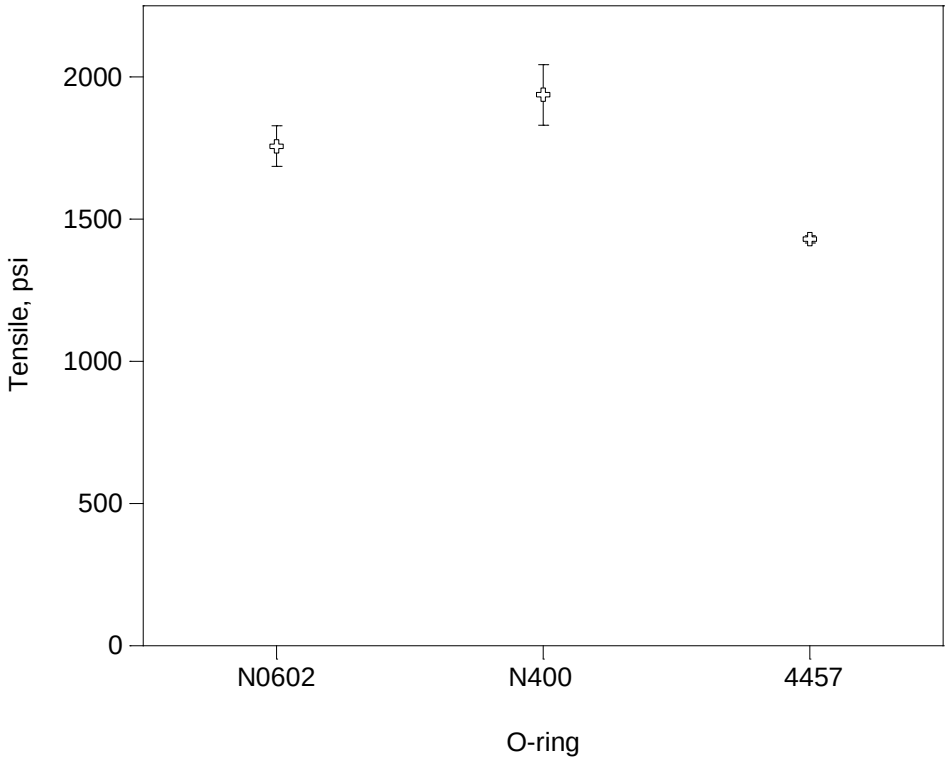

Figure 5. Baseline tensile (psi) for the as-received O-rings.

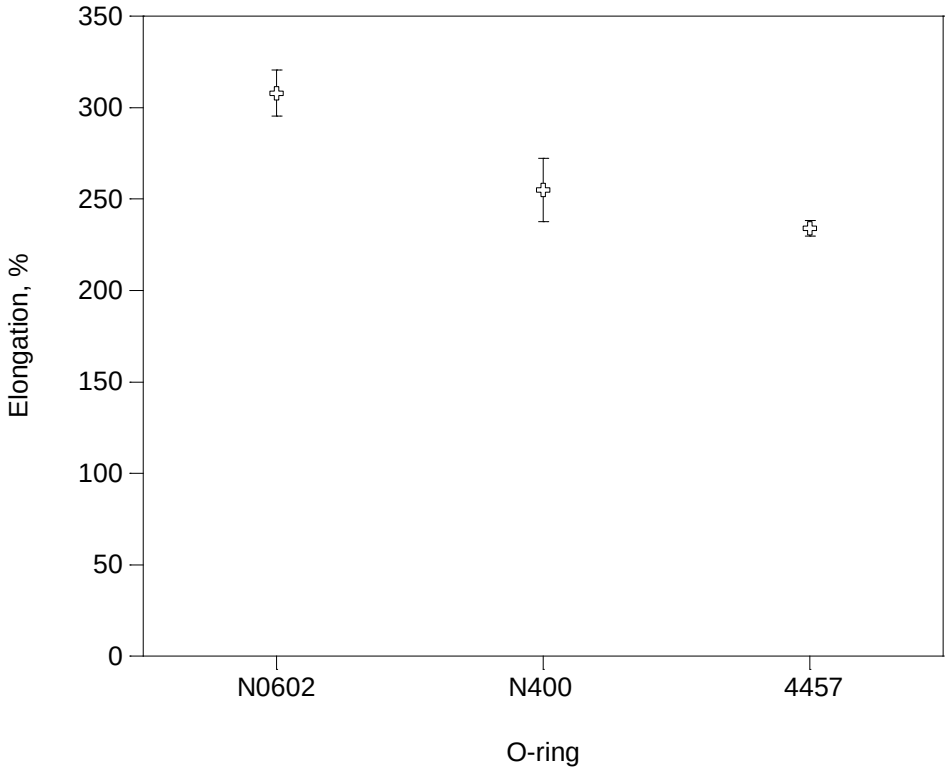

Figure 6. Baseline elongation (%) for the as-received O-rings.

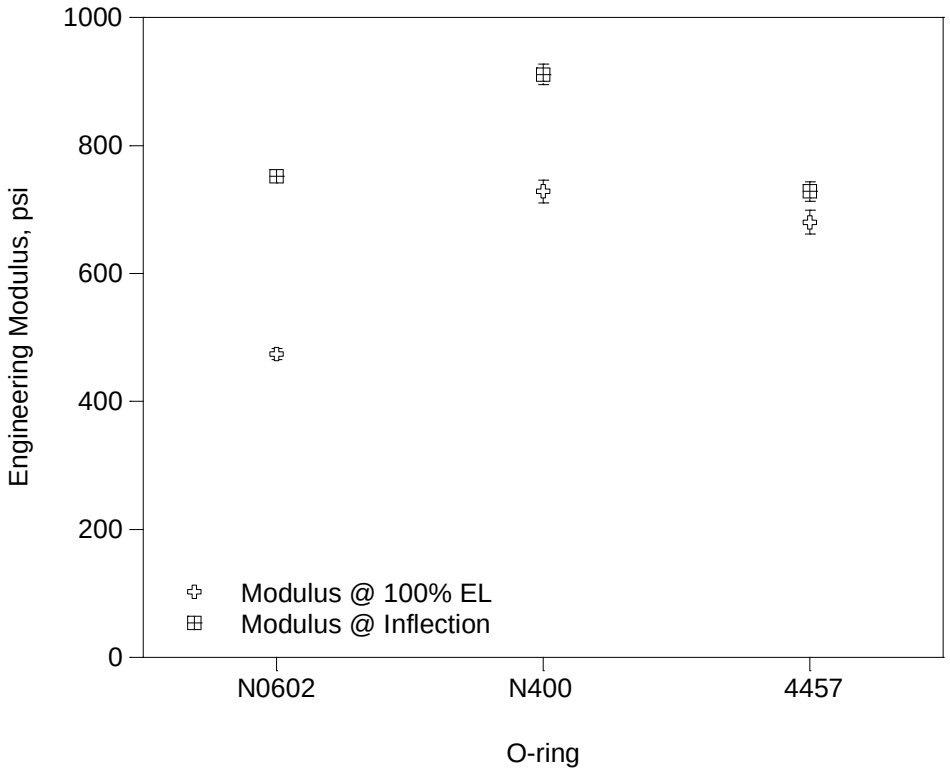

Figure 7. Baseline modulus (psi) at 100% elongation and at the inflection of the stress/strain curve for the as-received O-rings.

Baseline Compression Set

The baseline compression set was measured for each of the as-received O-rings material at 160˚F using the UDRI compression set fixtures as shown in Figure 1. Note that these fixtures constrain the O-rings with 25% compression in the same manner as the face seal used in the UDRI flow cells. The dimensions of the O-rings were measured in 3 locations at 14-day intervals giving the average compression set values summarized in Table 3 and Figure 8. Note that in lieu of 90% confidence intervals the span of the replicate values is shown.

Table 3. Average Baseline Compression Set

	Average Compression Set, %		
Time, days	N0602	N400	4457
0	0.0	0.0	0.0
14	46.7	32.6	36.8
28	63.5	42.3	49.0

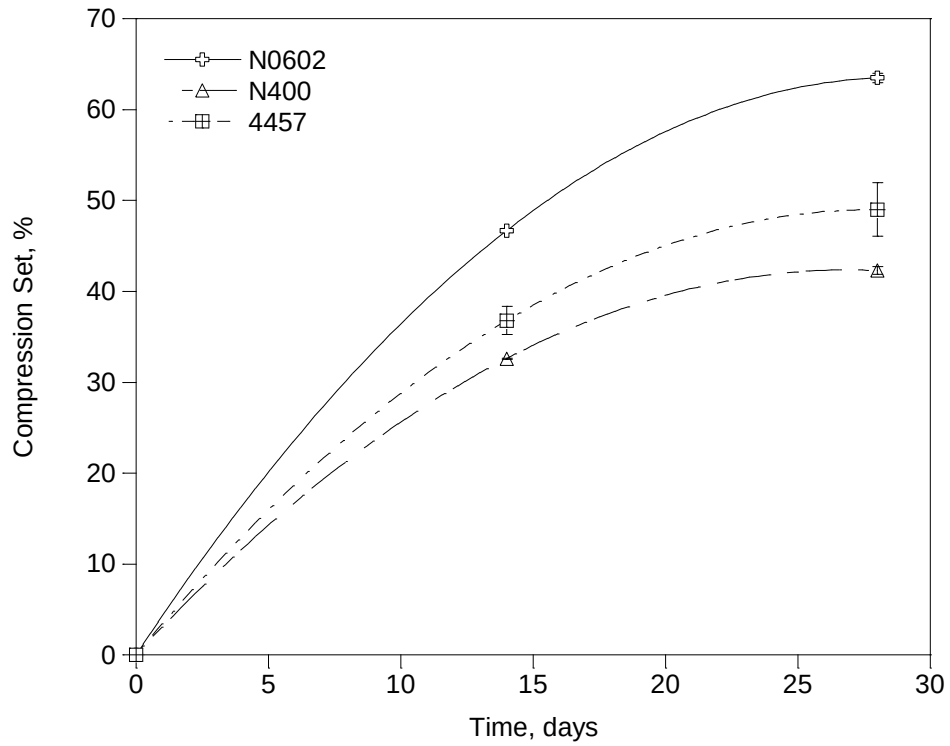

Figure 8. Baseline compression set (%) at 160F for the as-received O-rings. Note that the span of the replicate source values is indicated.

IR Spectra

Examples of the as-received O-rings were examined by Fourier-transform infrared spectroscopy using a germanium micro-ATR crystal sampling technique. An initial inspection of the samples suggest that the O-rings contain significant amounts of carbon black. Initial attempts at obtaining spectra yielded the result seen in Figure 9. Carbon black absorbs strongly in the entire mid-infrared region. The sloping baseline seen in absorbance mode is due to the increased penetration depth of the low-energy/long wavelength infrared photons during attenuated total reflectance. The small peak seen at 3650 wavenumbers (cm^{-1}) is due to the presence of magnesium silicate (i.e. talc), a common additive to polymers that are exposed to prolonged elevated temperatures. An overlay of talc and the N400 is shown in Figure 10.

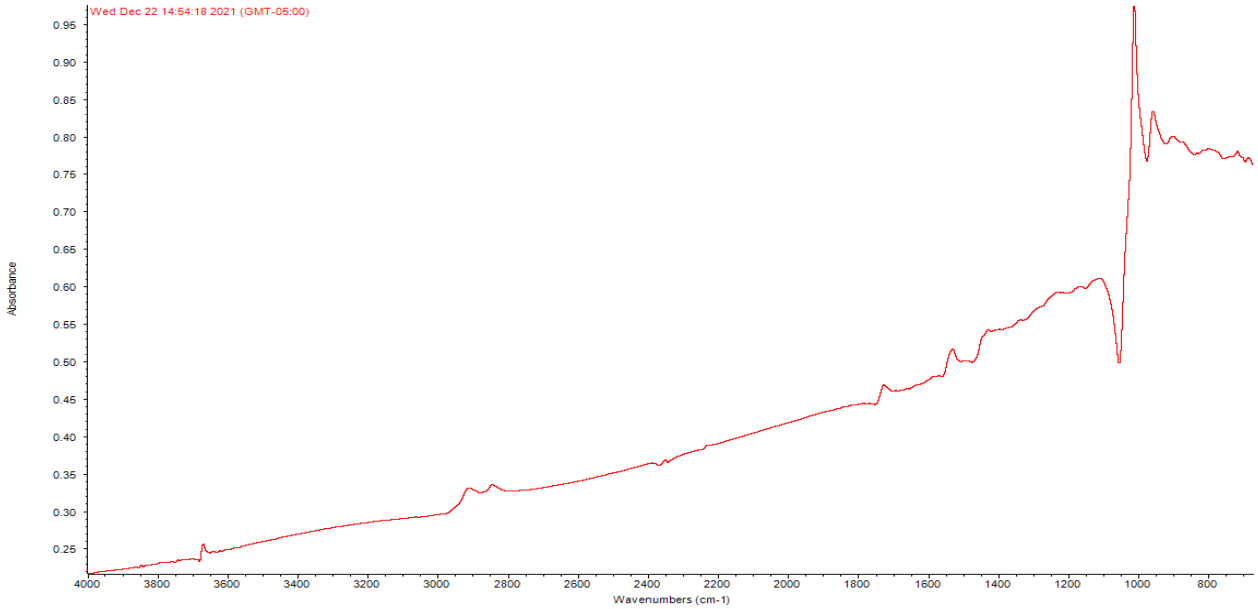

Figure 9. Initial raw uncorrected spectrum of an N400 O-ring.

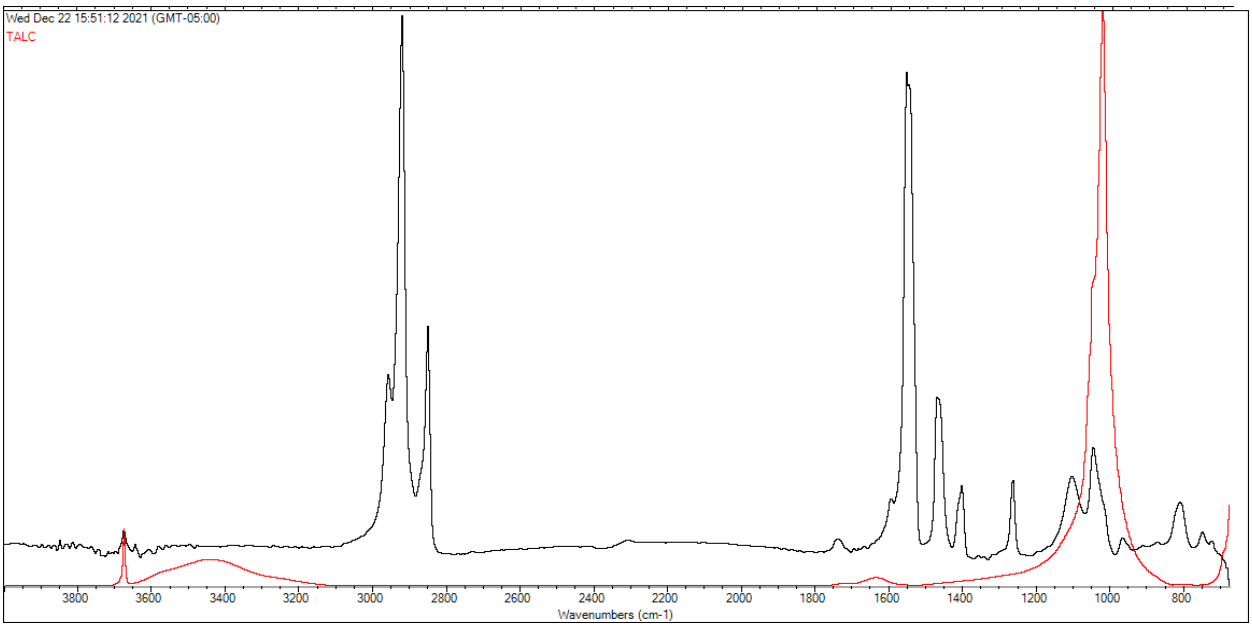

Figure 10. Overlay of baseline and ATR-corrected N400 with a talc library spectrum.

Subsequent attempts at obtaining spectra of the carefully cleaned exterior O-ring surface were more successful, and produced the spectra seen in Figure 11. These spectra indicate that N400, N0602, and N4457 appear to be identical in composition.

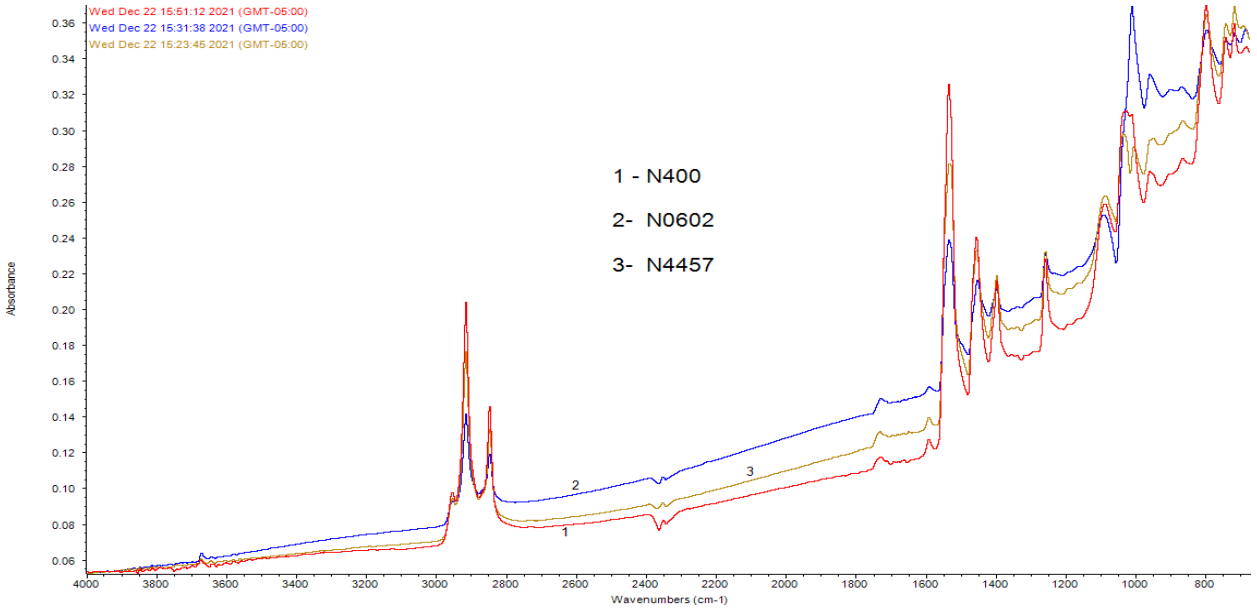

Figure 11. Spectral overlay of all three O-rings without ATR or baseline correction.

The spectra were then corrected for the sloping baseline discussed above. Further correction was implemented to compensate for spectral distortion caused by the ATR sampling which makes peaks on the right side of the spectrum larger than they would be in comparison to transmission. N400 thus corrected is shown in Figure 12.

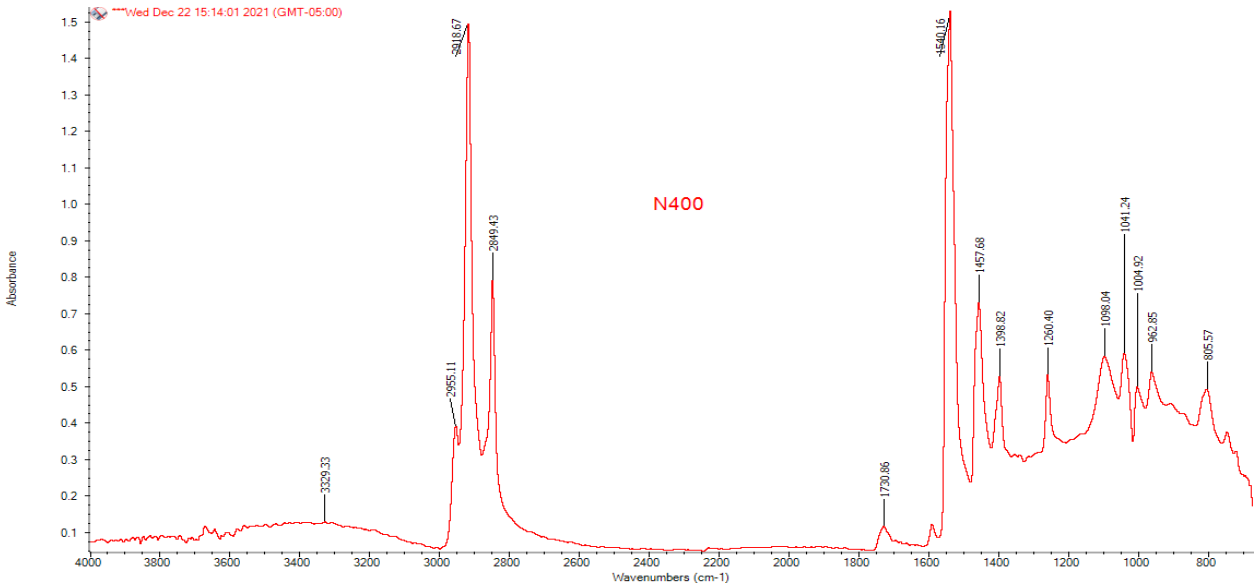

Figure 12. ATR and baseline corrected spectrum of N400.

The spectra shown in Figures 9-12 were from the exterior surface of the O-rings. There appears to be residual silicone mold release agent manifest in these spectra. This can be seen in the spectral overlay shown in Figure 13 below.

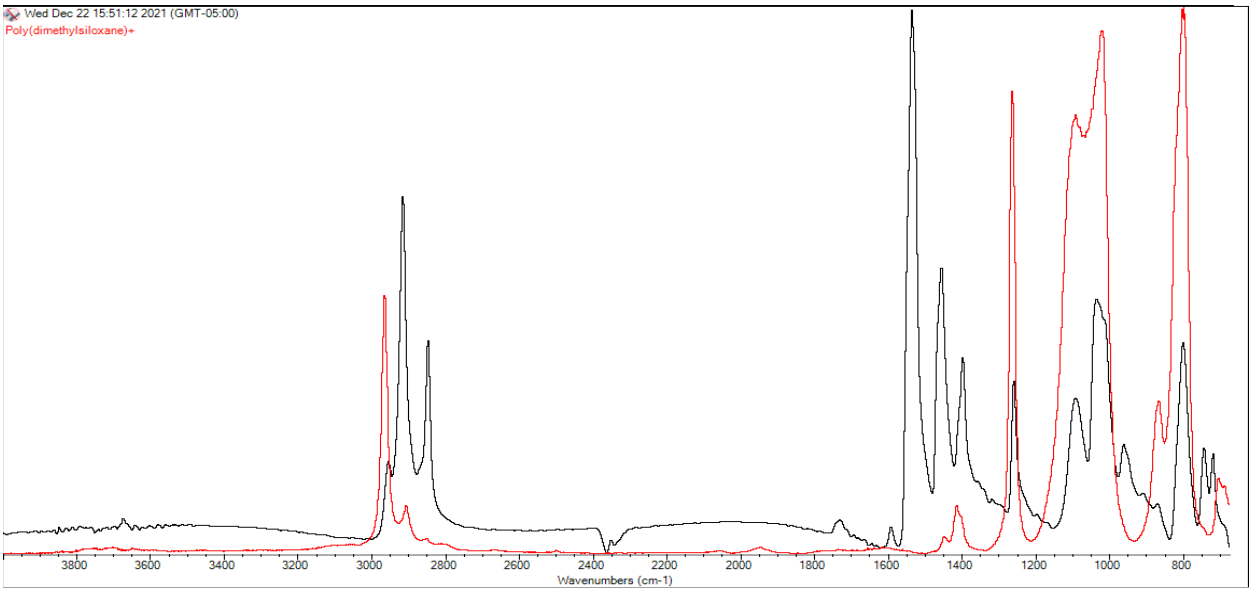

Figure 13. Spectral overlay of the surface of N400 with a silicone.

The O-rings were then sectioned to facilitate spectroscopic interrogation of the interior material of the rings. The resultant uncorrected spectra are shown in Figure 14.

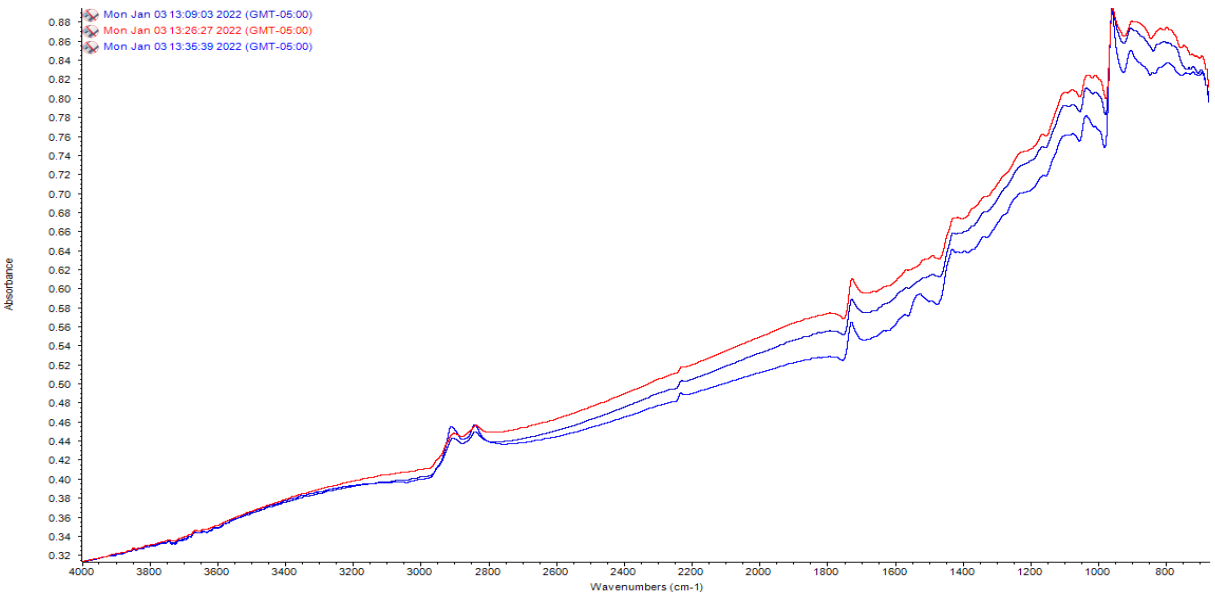

Figure 14 – Spectral overlay of the interior material of all three O-rings.

With the interior spectra the emergence of the characteristic nitrile peak at 2250 wavenumbers becomes apparent. An overlay of the N400 interior material with a library search result of poly(butadiene acrylonitrile) is shown in Figure 15. Overall, these results suggest that the loading of carbon black in the O-ring material makes using IR spectra as a means of quantifying the nitrile content of the O-ring problematic.

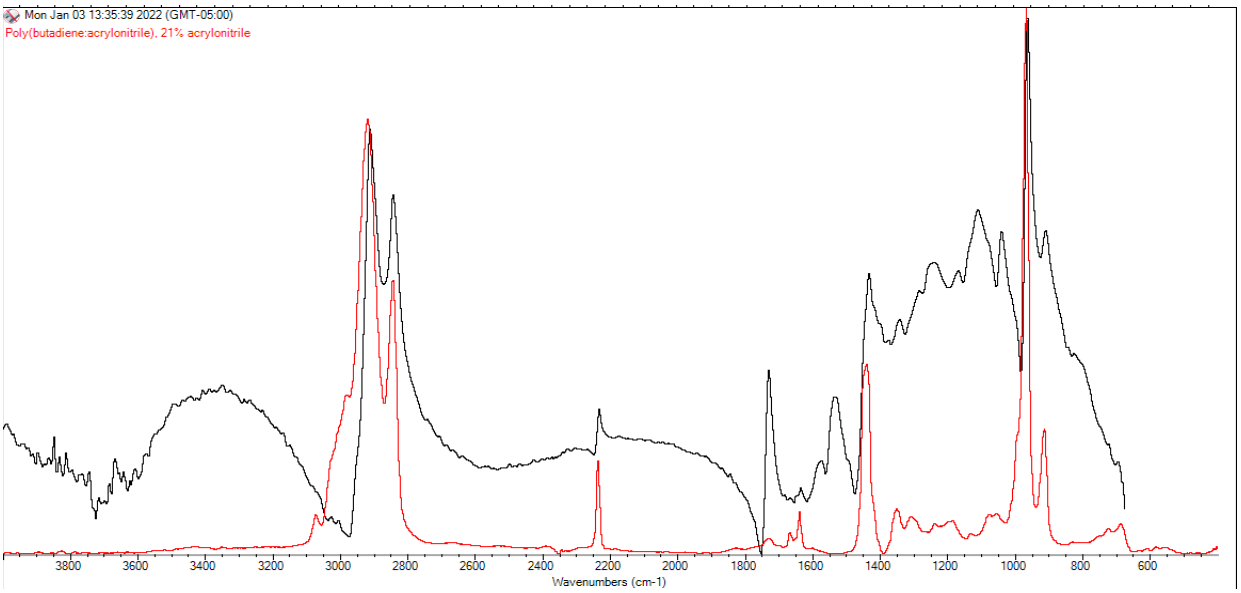

Figure 15. Spectral overlay of the interior material of N400 and a library search of nitrile rubber.

Glass Transition

The glass transition temperatures (Tg) of the as-received O-rings were evaluated using thermomechanical analysis in accordance with ASTM E1545. The results are summarized in Table 4.

Table 4. Glass Transition Temperatures of the Source O-rings

O-ring	Tg, ˚C	90% CI, ˚C
N0602	-51.2	1.4
N400	-49.5	0.6
4457	-50.8	0.7

Volume Swell

The volume swell of the O-ring materials was evaluated in each of the test fuels listed in Table 5. The equilibrium volume swell was measured at 75˚F using the method of optical dilatometry. The average values obtained from at least 4 samples are summarized in Table 6 and Figures 16-18. The 90% confidence intervals are also given. Note that the linear fits were selected to present the interpolation between the source Jet A and its blends. This is because in weakly bound systems the volume swell tends to vary linearly with blending ratio and in this case the source Jet A is blended with two different diluents; SPK and Aromatic 100. Hence, linear trends between the source Jet A and its blends. Furthermore, comparing the volume swell of the CPK-0 with the SPK/Jet A trend line suggests that the average volume swell character of the CPK-0 is comparable to a Jet A with 11.3% aromatics.

Table 5. Test Fuels

Fuel	Aromatics % v/v	Notes
CPK-0	0.0	CPK-0 with 0% aromatics
Jet A_4	4.0	Jet A blended with SPK
Jet A	16.2	Stock Jet A
Jet A_25	25.0	Jet A blended with Aromatic 100

Table 6. Volume Swell Results

Material	Fuel	Aromatics % v/v	Swell % v/v	90% CI % v/v
N0602	CPK-0	0.0	4.7	0.5
	Jet A_4	4.0	0.4	0.3
	Jet A	16.2	9.8	0.4
	Jet A_25	25.0	15.4	0.5
N400	CPK-0	0.0	8.1	0.3
	Jet A_4	4.0	0.8	0.3
	Jet A	16.2	10.2	0.9
	Jet A_25	25.0	16.6	0.4
4457	CPK-0	0.0	-0.1	0.3
	Jet A_4	4.0	-4.4	0.2
	Jet A	16.2	3.1	0.4
	Jet A_25	25.0	8.4	0.2

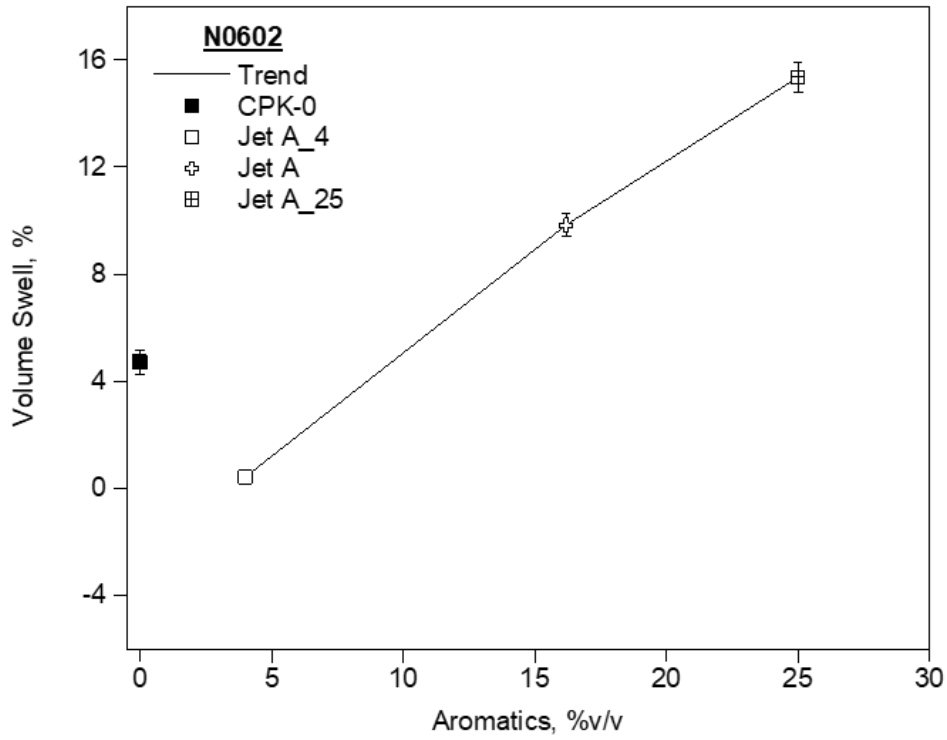

Figure 16. Equilibrium volume swell of the N0602 O-rings at 75˚F as measured by optical dilatometry.

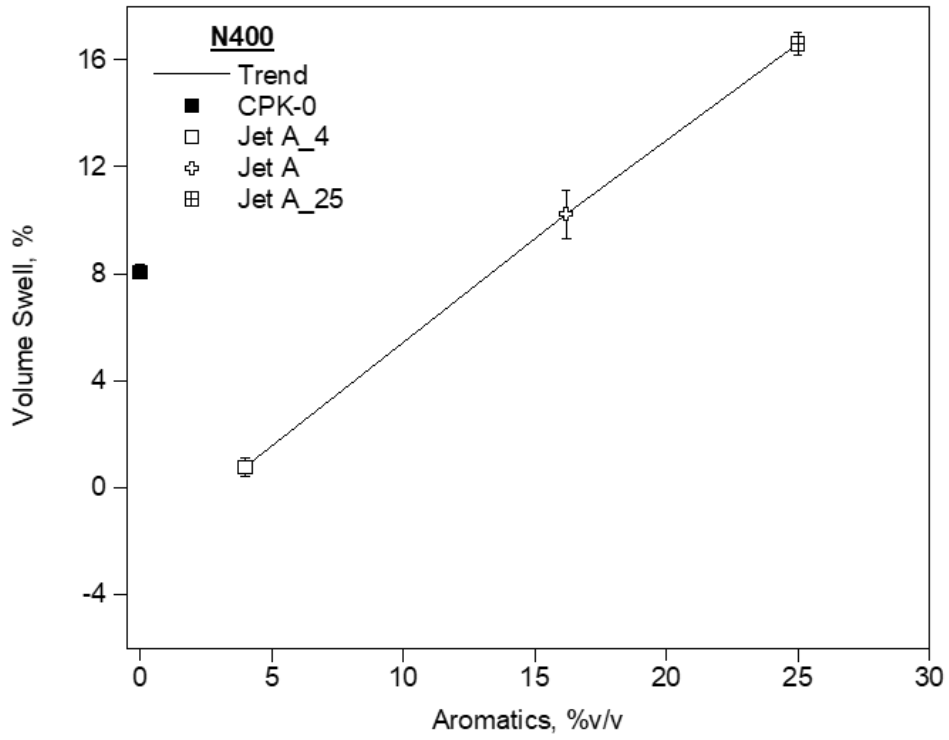

Figure 17. Equilibrium volume swell of the N400 O-rings at 75˚F as measured by optical dilatometry.

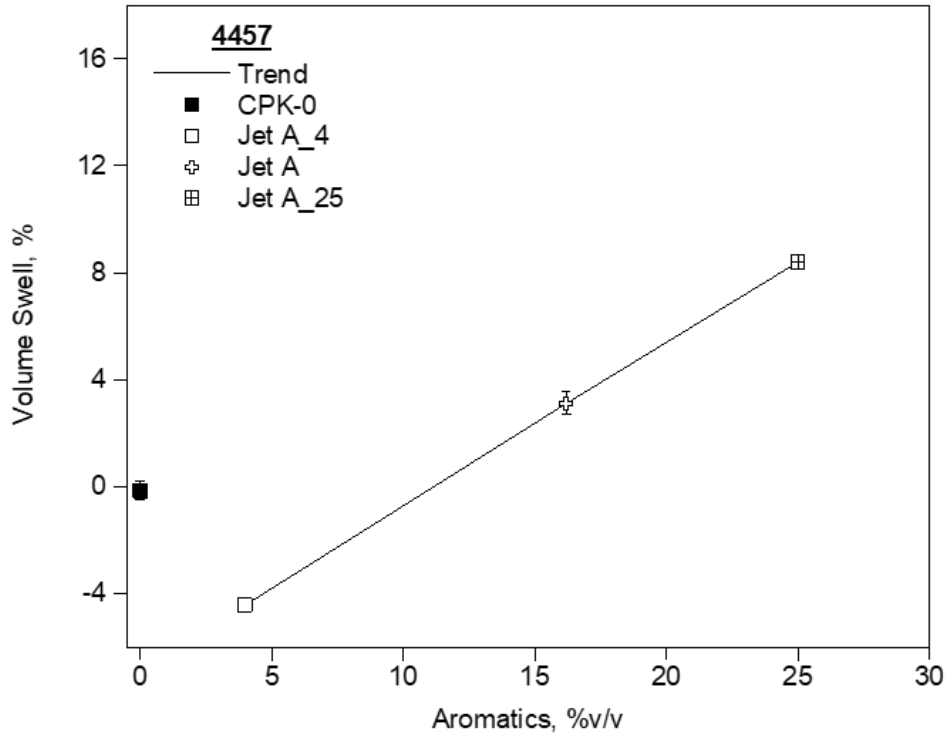

Figure 18. Equilibrium volume swell of the 4457 O-rings at 75˚F as measured by optical dilatometry.

Linear Swell and its Influence on Nominal O-ring Compression

Volume swell is often used to quantify how an elastomer responds to a fluid and as noted above, reflects the overall exchange that occurs between a fluid and an elastomer in terms of components extracted by the fluid and absorbed by the elastomer resulting in the final equilibrium state. However, in the design and performance of O-ring seals volume is rarely mentioned and usually only influences the width of the O-ring gland to give the O-ring a free volume into which it can swell without extruding from the gland. (The volume of an O-ring gland is typically 30% larger than the volume of the source O-ring and can therefore accommodate up to 30% volume swell.) The primary metric of interest in the design and performance of a compression seal is the depth of the gland as this determines the initial compression of the O-ring seal. For example, static O-ring seals are typically compressed 25% while dynamic O-ring seals are often compressed from 12-15%. The O-ring being used in this study are size 214 O-rings with a nominal width of 0.139" +/- 0.004". A static seal providing 25% compression would therefore have a depth of 0.104", compressing the seal 0.035", or 25% of its initial dry width.

The impact of volume swell on the true compression of an O-ring can be estimated by expressing the swell in terms of its effects on the diameter if the O-ring in the direction of compression. In other words, expressing the volume swell as a linear swell as summarized in Table 7 and Figure 19. The estimated changes in the diameter of the O-ring can be used to estimate how the volume swell influences the compression as summarized in Table 8 and Figures 20 and 21. These figures also show the nominal end of service life condition of 50% compression set. Note that prior work suggests that that actual end of service life where leaks can occur is closer to 80-90% compression set.

Table 7. Linear Swell Results

Material	Fuel	Aromatics % v/v	Linear Swell % l/l	90% CI % l/l
N0602	CPK-0	0.0	1.5	0.1
	Jet A_4	4.0	0.1	0.1
	Jet A	16.2	3.2	0.1
	Jet A_25	25.0	4.9	0.2
N400	CPK-0	0.0	2.6	0.1
	Jet A_4	4.0	0.3	0.1
	Jet A	16.2	3.3	0.3
	Jet A_25	25.0	5.3	0.1
4457	CPK-0	0.0	0.0	0.1
	Jet A_4	4.0	-1.5	0.1
	Jet A	16.2	1.0	0.1
	Jet A_25	25.0	2.6	0.2

*v/v = volume/volume, l/l = length/length

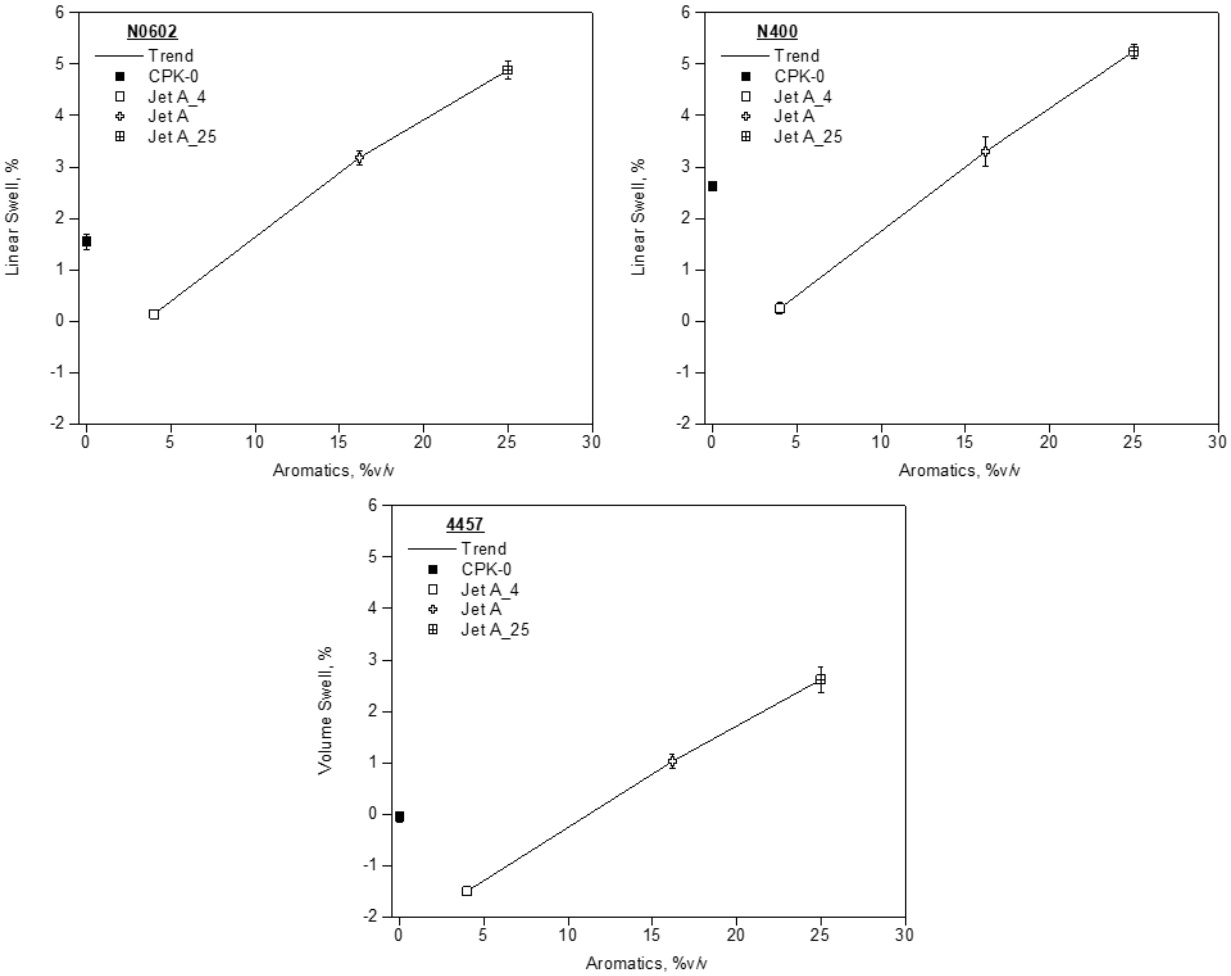

Figure 19. Equilibrium linear swell of the test O-rings at 75˚F as measured by optical dilatometry.

Table 8. Nominal O-ring Width & Compression*

Material	Fuel	Aromatics % v/v	Nom Width, in.	Nom Comp
N0602	CPK-0	0.0	0.141	26.3%
	Jet A_4	4.0	0.139	25.3%
	Jet A	16.2	0.143	27.5%
	Jet A_25	25.0	0.146	28.7%
N400	CPK-0	0.0	0.143	27.1%
	Jet A_4	4.0	0.139	25.4%
	Jet A	16.2	0.144	27.6%
	Jet A_25	25.0	0.146	28.9%
4457	CPK-0	0.0	0.139	25.1%
	Jet A_4	4.0	0.137	24.0%
	Jet A	16.2	0.140	25.9%
	Jet A_25	25.0	0.143	27.1%

*Initial nominal width of 0.139” and 25% compression.

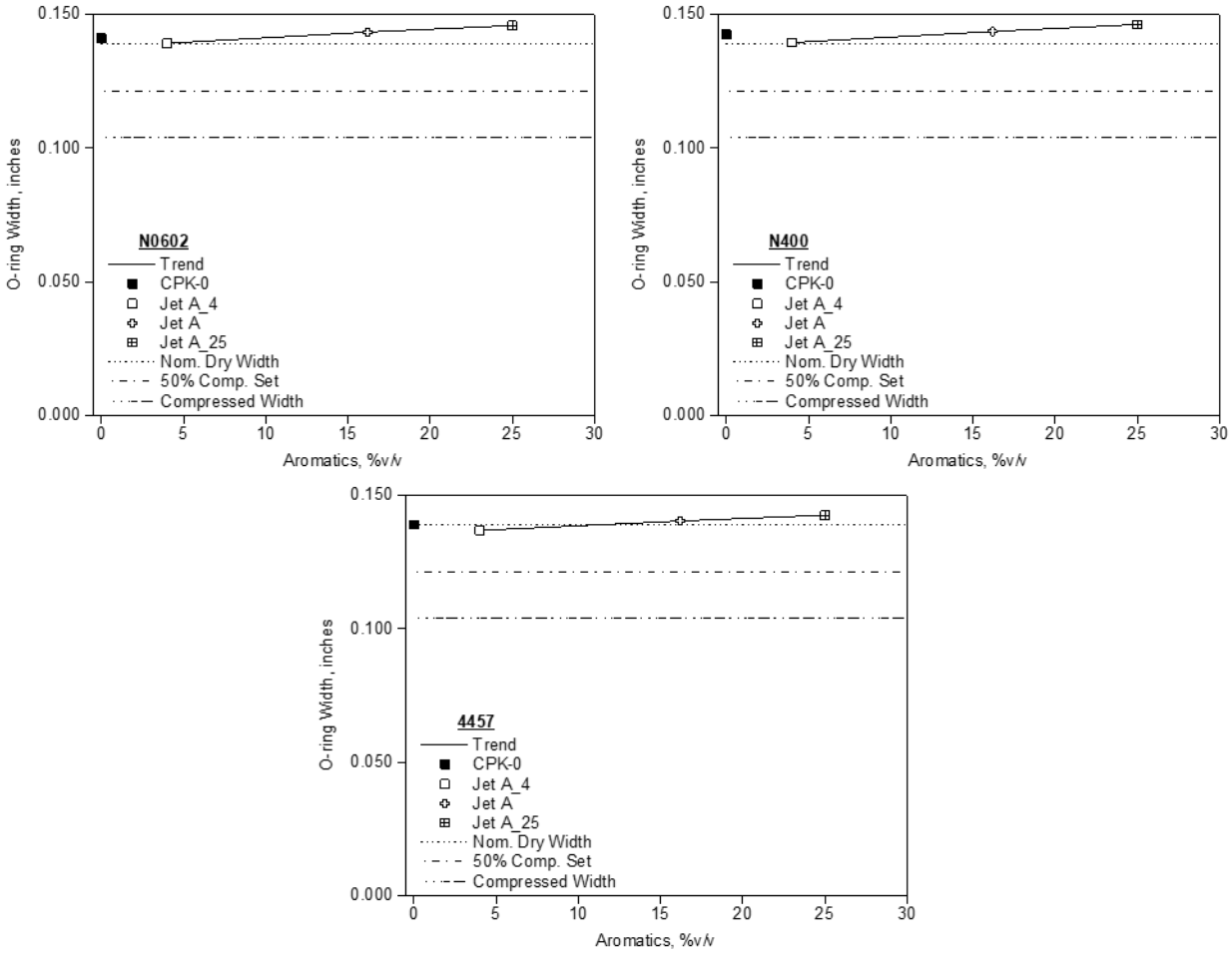

Figure 20. Equilibrium nominal width of the test O-rings at 75˚F as measured by optical dilatometry. The dashed line marks the nominal end of service condition of 50% compression set.

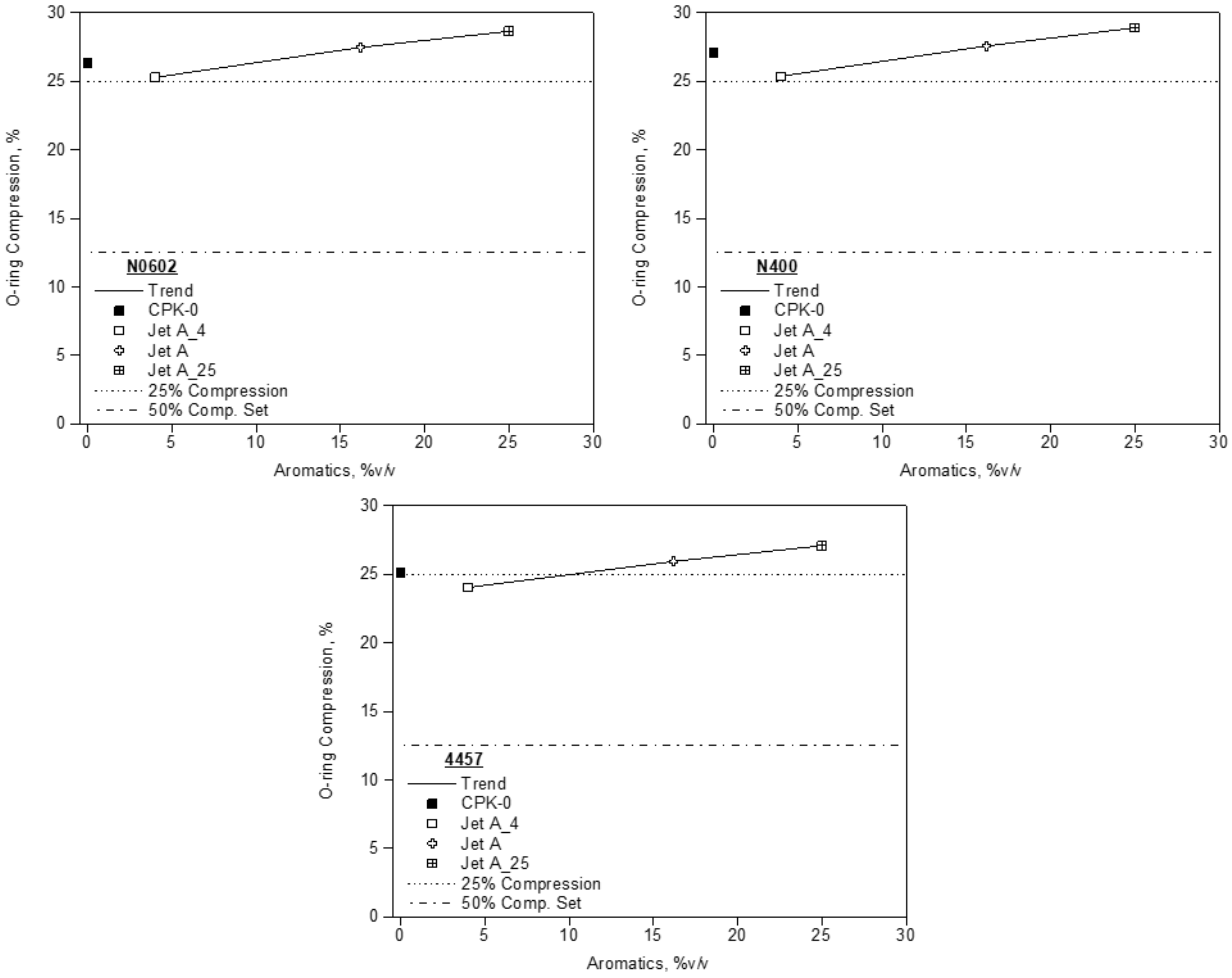

Figure 21. Equilibrium nominal compression of the test O-rings at 75˚F as measured by optical dilatometry. The dashed lines mark the nominal initial compression of 25% and the nominal end of service condition of 50% compression set.

These results illustrate that the volume swell behavior of the O-rings used here in the various fuels has a relatively small impact on the physical width of the O-rings and its subsequent impact on the compression of the O-ring seals. This emphasizes that the potential for leaks occurring as a consequence of switching from a conventional fuel to a low-swell fuel is most likely to become problematic for O-ring seals that are near the end of the normal service life where safety margins are much reduced as compared to their initial service conditions.

Note that the tolerance of +/- 0.004” is equivalent to +/- 2.9% in the width and +/- 8.6% in volume. The impact of this allowable variation in the as-produced O-rings on their width and nominal compression is summarized in Figure 22. It is interesting to note that the changes in the dimensions of the O-rings used here as a consequence of their exposure to the various test fuels is similar to the allowable variation in the as-

produced O-rings. However, in the case of fuel switching the changes occur dynamically while the O-ring is in-service. This comparison is made primarily to illustrate the magnitude of the influence of the exposure to alternative fuel in context with the normal variation in the O-ring dimensions.

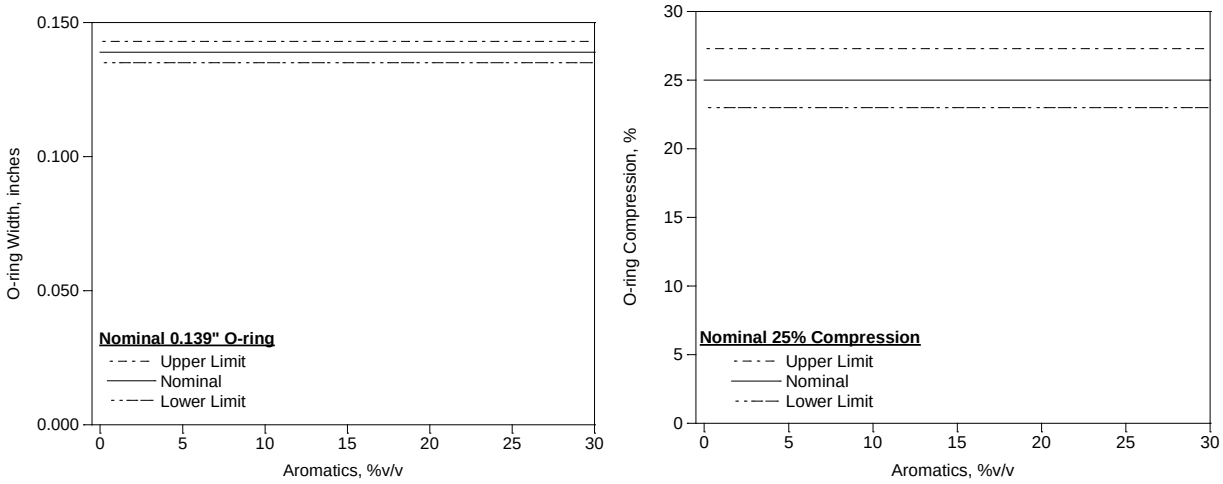

Figure 22. Graphical illustration of the influence of the +/- 0.004" tolerance on the width and compression of a 0.139" O-ring.

Overall O-ring Composition by TGA and GC-MS

The overall composition of the source O-rings was determined using TGA in nitrogen and solvent extraction GC-MS.

The TGA results are summarized in Table 9 and Figure 23. These describe the overall composition of the O-rings in terms of the mass fraction of plasticizer, elastomer, and the residual mass fraction which usually includes primarily carbon black and filler plus a small fraction of carbonaceous char from the pyrolysis of the elastomer. These results show a slight variation in the plasticizer content from 9.0% (N0602) to 10.6% (4457). Recall that when exposed to fuel these components are extracted and replaced by absorbed fuel to give the net volume swell in fuel. There is a relatively modest variation in the elastomer content from 45.7% (N400) to 32.5% (4457). The combination of the lowest elastomer content and the highest plasticizer content may contribute to the relatively low volume swell of the 4457 elastomer.

Table 9. TGA Results

O-ring	Plasticizer	Elastomer	Other*
N0602	9.0%	38.6%	52.4%
N400	10.0%	44.3%	45.7%
4457	10.6%	32.5%	56.9%

*Carbon black, filler, char

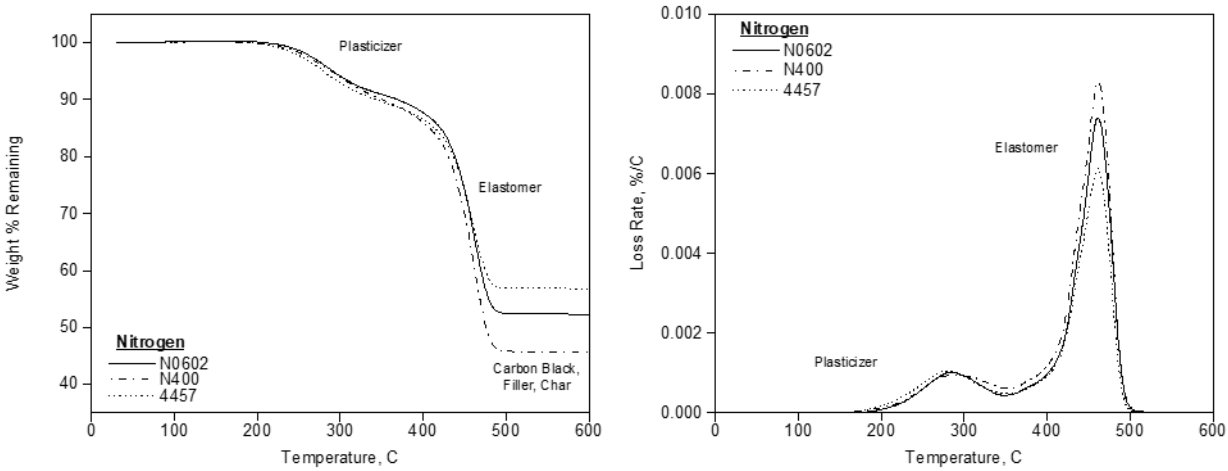

Figure 23. TGA (left) and DTGA (right) for the source O-rings in nitrogen.

The composition of the plasticizer was analyzed using solvent extraction GC-MS. For each analysis samples weighing approximately 10 mg were placed in a sealed GC vial along with 1 mL of methylene chloride solvent and allowed to extract for at least 1 hour. These were then analyzed using an Agilent 7890/5975 GC-MSD fitted with a 30 m x 0.250 mm x 0.25 μm column with an HP-5MS UI stationary phase. Each injection was 3 μL with a 5:1 split with a column head pressure of 7.4 psi. The column was initially held at 40˚C for 5 minutes, then heated to 320˚C at 20˚C/min, and held for 10 min. The MSD was turned on after a 4 minute solvent delay and scanned from 35-550 amu.

The GC-MS test results shown in Figure 24 illustrates that the plasticizer in each of the source O-rings is principally, bis[2-(2-butoxyethoxy)ethyl]adipate plus what appears to be a silicone oil. The plasticizer in 4457 also included approximately 20% dioctyl adipate, a plasticizer of a similar type as the primary component.

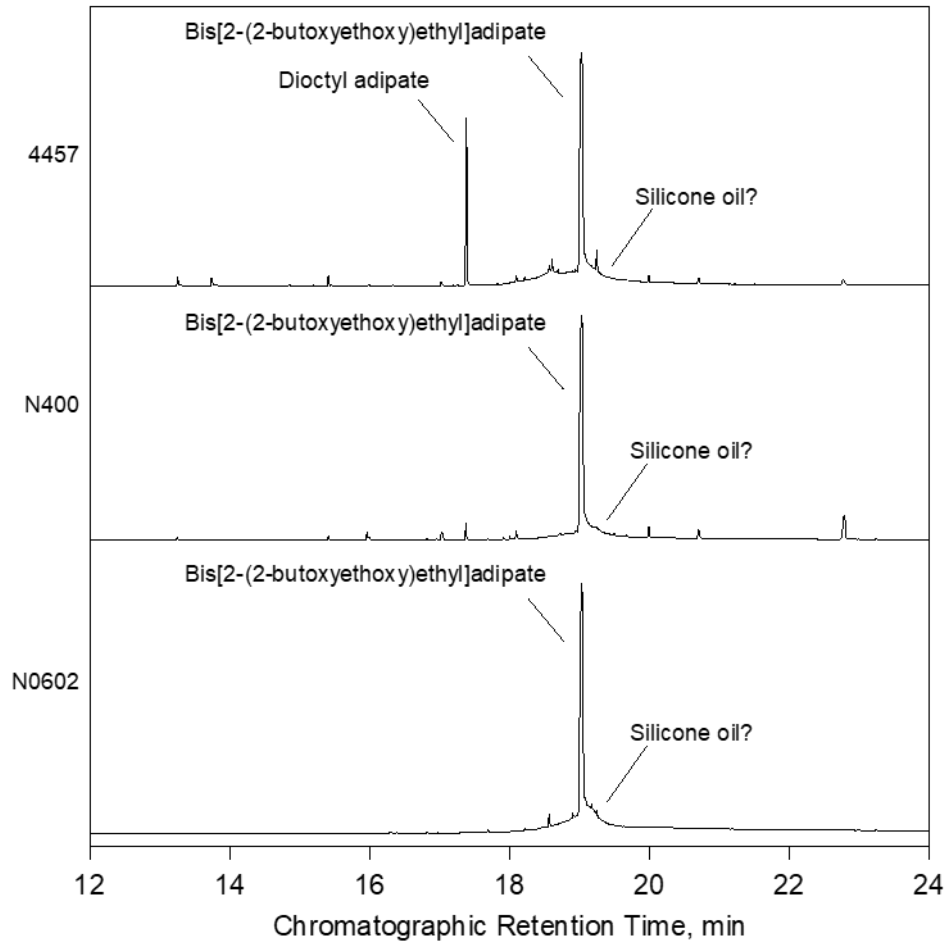

Figure 24. GC-MS analysis of the source O-rings.

Fuel Solubility

The overall composition of the test fuels is summarized in the total ion chromatograms (TICs) given in Figure 25. The overall composition of the source blending stock as determined using GCxGC are given in Table 10. The overall composition of the test fuels is given in Table 11.

Table 10. Composition of the Fuel Blending Stocks as per GCxGC

Class Fraction	SPK	A-100	Jet A	CPK-0
Aromatics	0.1%	97.7%	16.2%	0.0%
n-Paraffins	9.5%	0.3%	20.2%	2.3%
i-Paraffins	86.3%	2.0%	30.4%	1.3%
Cycloparaffins	4.2%	0.1%	33.8%	96.4%

Table 11. Composition of the Test Fuels

Class Fraction	Jet A_4*	Jet A	Jet A_25*	CPK-0
Aromatics	4.0%	16.2%	25.0%	0.0%
n-Paraffins	12.1%	20.2%	18.0%	2.3%
i-Paraffins	72.6%	30.4%	27.1%	1.3%
Cycloparaffins	11.4%	33.8%	30.0%	96.4%

*Calculated using linear blending rules

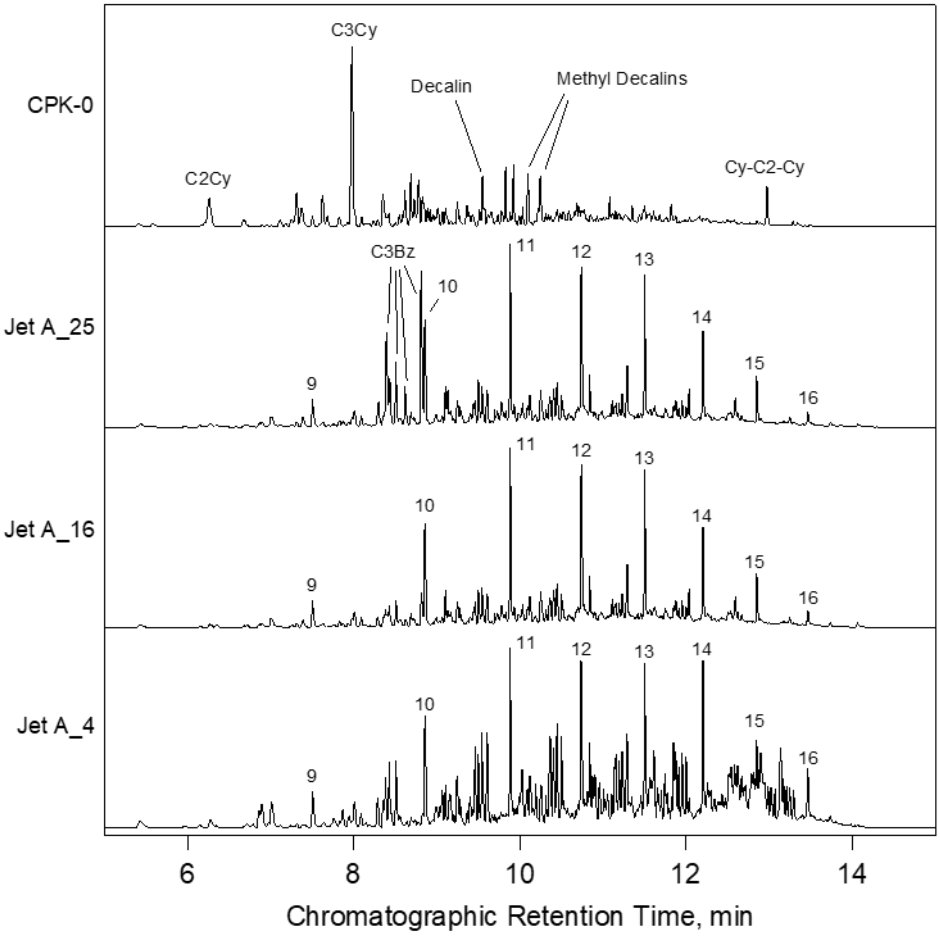

Figure 25. Overall GC-MS analysis of the test fuels: Cy = cyclohexane, Bz = benzene, Cn = n pendant carbons, 9-16 = linear paraffins with 9-16 carbons.

The TICs given in Figure 25 illustrate that the Jet A fuel is dominated by the C9-C16 normal paraffins. Between each of these peaks is a repeating series of smaller peaks that are primarily iso paraffins. Note that the aromatics are not easily seen on this scale. Recall that the Jet A_4 was derived from the Jet A by blending it with SPK. The increased size of the peaks associated with the iso paraffins reflects the relatively high concentration of iso paraffins in the SPK blending stock. Furthermore, noting that molecular weight increases with chromatographic retention time, the addition of the SPK shifted the overall molecular weight distribution to heavier and larger paraffins. Recalling that volume swell tends to decrease as molecular weight (and molar volume) increases, this would be expected to reduce the volume swell character of the fuel. This affect would be in addition to the loss of volume swell character resulting from the reduction in the aromatic content of this fuel. Furthermore, the SPK blending stock included only 4.2% cycloparaffins and this resulted in a significant decrease in the cycloparaffin content of the Jet A_4 fuel as compared to the Jet A source fuel. This would also contribute to a reduction in the volume swell character of this fuel. The Jet A_25 fuel was similarly derived from the Jet A fuel by blending it with Aromatic 100. The TICs given in Figure 25 show that this increased the concentration of relatively light alkyl benzenes to the point that they are easily seen in the chromatography on this scale. Recall that the aromatics bring some polar and hydrogen bonding character to the fuel, increasing the strength of interaction with fuel system elastomers, particularly nitrile rubber. This effect is amplified by the relatively low molecular weight (and low molar volume) of these aromatic components thereby increasing the volume swell character of this fuel. It is interesting to note that the Aromatic 100 blending stock included only 0.1% cycloparaffins and this results in a slight decrease in the cycloparaffins content of the Jet A_25 fuel as compared to the Jet A source fuel. In contrast, the CPK-0 fuel is comprised primarily of cycloparaffins. Prior work with cycloparaffins suggest that they exhibit a slight polar character and this combined with the slightly lower molar volume of these components results in a slightly higher solubility and commensurate volume swell as compared to the n,i-paraffins.

The relative solubility of the test fuels as well as selected class fractions and specific components are summarized in Figures 26-29 and Table 12. Table 12 summarizes the relative solubility in terms of the polymer/fuel partition coefficient (Kpf); the ratio of the concentration of the component or class fraction in the polymer to that in the overlying fuel. Kpf values that are <1 indicate that the concentration in the polymer is less than that in the fuel and reflects the resistance that the polymer has towards that component, Kpf values = 1 indicates no resistance, and Kpf >1 indicates that the polymer concentrates that component from the fuel. Note that the overall Kpf approximates the volume fraction of absorbed fuel and reflects the relative volume of fuel absorbed. This can be a more accurate measure of the strength of interaction between the fuel and elastomer than volume swell as the swell is a composite measure of fuel absorbed and plasticizer extracted whereas the Kpf is based only on the absorption of fuel, and it is not strongly affected by the plasticizer. Note that the overall

Kpf is only an approximation of the relative volume of absorbed fuel as it assumes that the overall GC-MS response factor for the fuel is fixed when it actually depends on the composition of the absorbed fuel.

Comparing the overall composition of the fuel absorbed by each material with the fuel in which it was aged as shown in Figures 26-29 shows that the pattern of absorption is similar for each material indicating a high degree of similarity between the 3 test materials. The chromatography for the Jet A fuel and fuel blends also show that while the concentration of aromatics in the absorbed fuel is elevated and relatively easy to see in the analysis of the absorbed fuel, it is not to the exclusion of the paraffins which remain the dominant class fraction in the absorbed fuel. It is interesting to note the exceptionally high absorption of the naphthalenes which are easily seen in the absorbed fuel, but not evident in the source fuels illustrating that these components are preferentially absorbed to a significant extent. Note that a detailed examination of the absorbed fuel shows that naphthalene is absorbed with exceptionally high efficiency, but it is not obvious in the TICs as it co-elutes with the C12 normal paraffin.

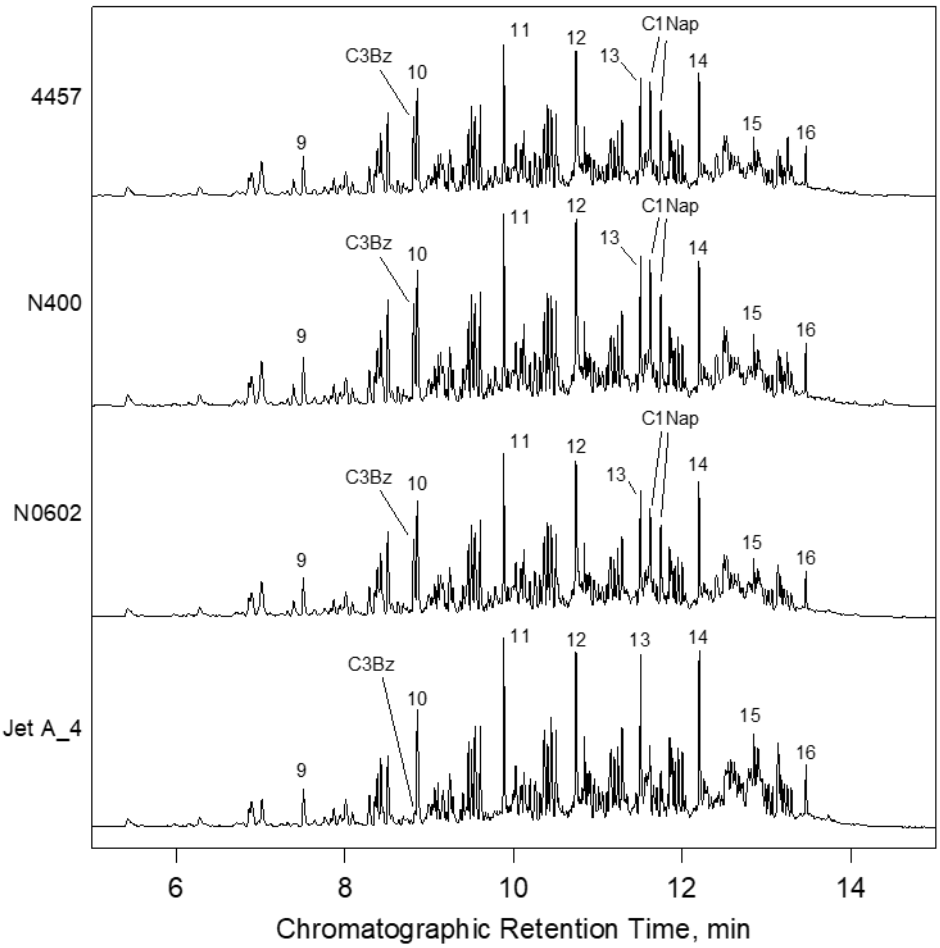

Figure 26. Overall GC-MS analysis of the Jet A_4 test fuel and the fuel absorbed by the test materials: Bz = benzene, Nap = naphthalene, Cn = n

pendant carbons, 9-16 = linear paraffins with 9-16 carbons.

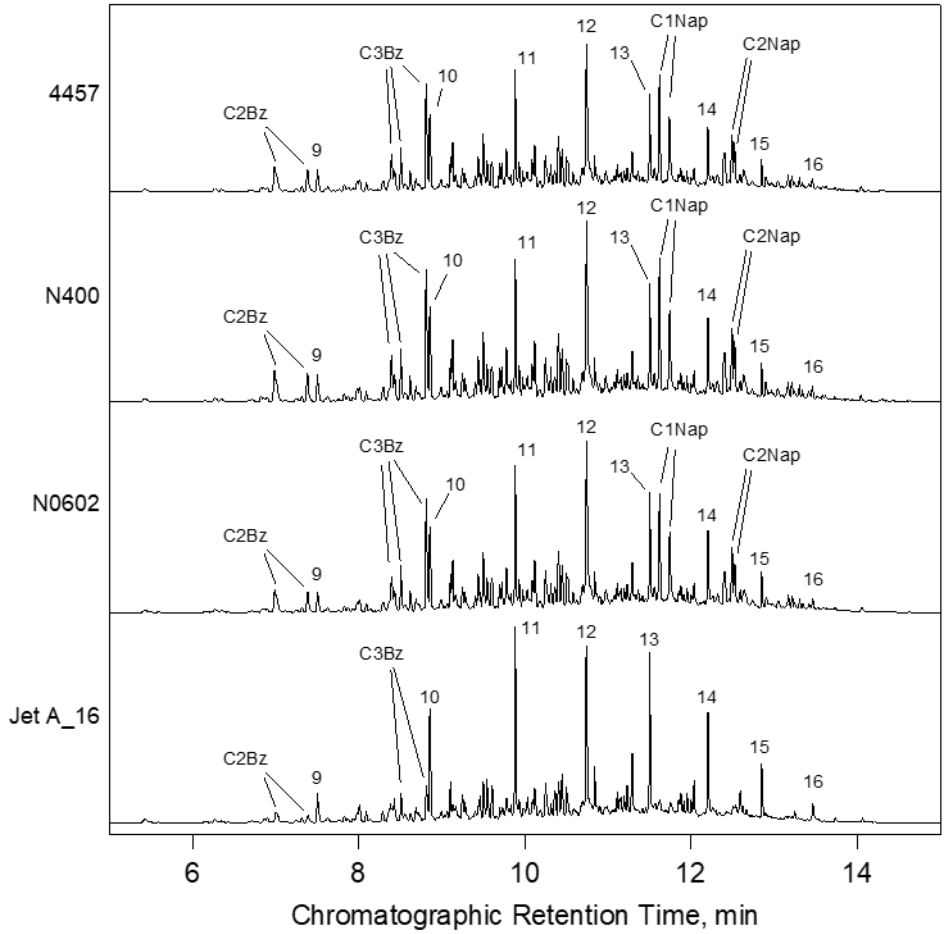

Figure 27. Overall GC-MS analysis of the Jet A test fuel and the fuel absorbed by the test materials: Bz = benzene, Nap = naphthalene, Cn = n pendant carbons, 9-16 = linear paraffins with 9-16 carbons.

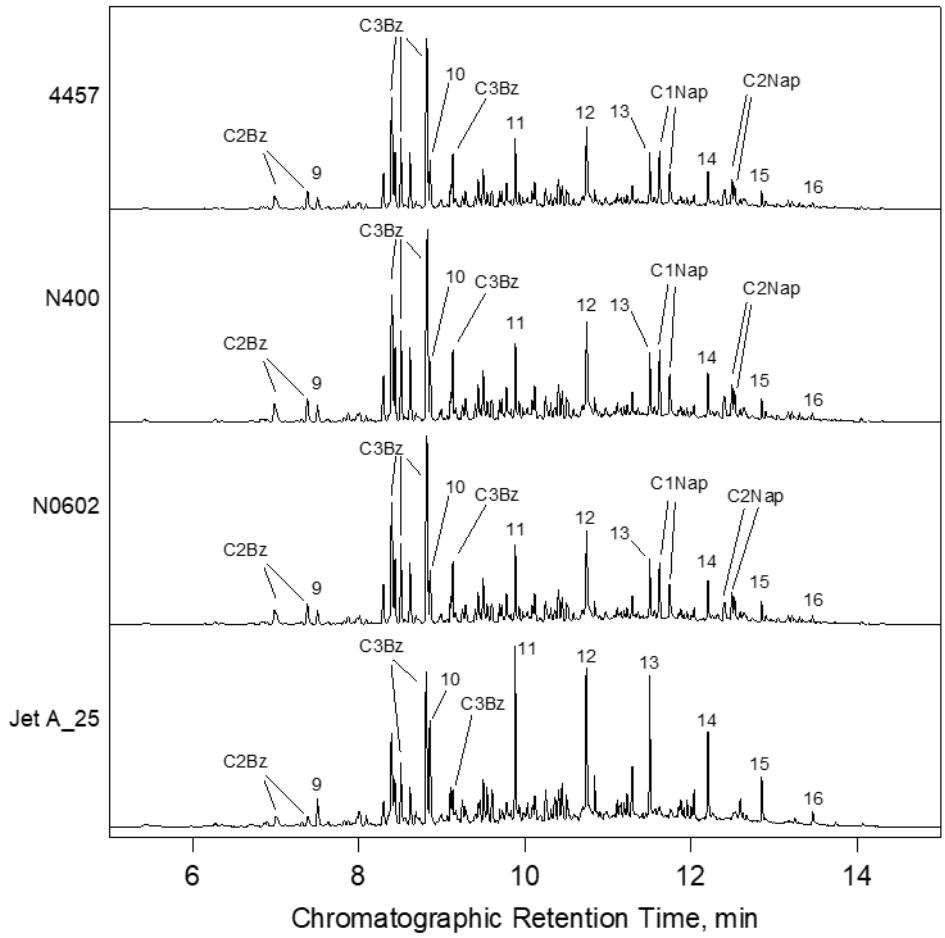

Figure 28. Overall GC-MS analysis of the Jet A_25 test fuel and the fuel absorbed by the test materials: Bz = benzene, Nap = naphthalene, Cn = n pendant carbons, 9-16 = linear paraffins with 9-16 carbons.

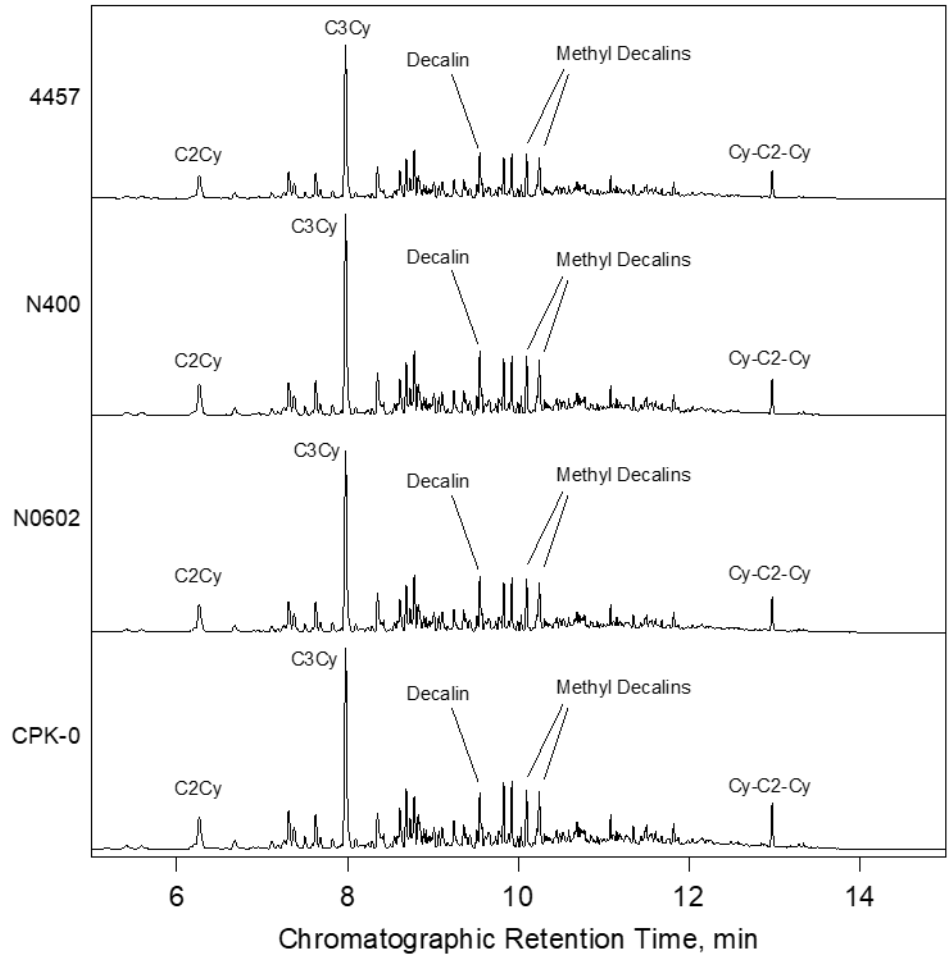

Figure 29. Overall GC-MS analysis of the CPK-0 test fuel and the fuel absorbed by the test materials: Bz = benzene, Nap = naphthalene, Cn = n pendant carbons, 9-16 = linear paraffins with 9-16 carbons.

Table 12. Polymer-Fuel Partition Coefficients, Kpf

Fuel	Class Fraction*	N0602	N400	4457	Average
Jet A_4	Overall (TIC)	0.113	0.134	0.107	0.118
	n,i-Paraffins (57)	0.088	0.102	0.072	0.088
	Cycloparaffins (83)	0.106	0.127	0.102	0.112
	C3 Aromatics (105)	0.431	0.531	0.407	0.456
	Naphthalene (128)	5.494	7.121	5.428	6.014
	Naphthalenes (141)	0.468	0.568	0.436	0.491
Jet A	Overall (TIC)	0.220	0.250	0.201	0.224
	n,i-Paraffins (57)	0.132	0.142	0.116	0.130
	Cycloparaffins (83)	0.162	0.180	0.147	0.163
	C3 Aromatics (105)	0.452	0.528	0.434	0.471
	Naphthalene (128)	1.855	2.210	1.778	1.948
	Naphthalenes (141)	0.900	1.048	0.841	0.930
Jet A_25	Overall (TIC)	0.252	0.278	0.220	0.250
	n,i-Paraffins (57)	0.143	0.151	0.120	0.138
	Cycloparaffins (83)	0.176	0.193	0.152	0.174
	C3 Aromatics (105)	0.450	0.503	0.399	0.450
	Naphthalene (128)	1.966	2.226	1.780	1.990
	Naphthalenes (141)	0.855	0.971	0.775	0.867
CPK-0	Overall (TIC)	0.164	0.180	0.136	0.160
	n,i-Paraffins (57)	0.138	0.150	0.114	0.134
	Cycloparaffins (83)	0.162	0.179	0.140	0.160
	C3 Aromatics (105)	bdl	bdl	bdl	bdl
	Naphthalene (128)	bdl	bdl	bdl	bdl
	Naphthalenes (141)	bdl	bdl	bdl	bdl

*() denotes the mass fragment used for each class fraction, TIC = total ion current

The relative solubility of the fuel can be quantified by the polymer-fuel partition coefficients as summarized in Table 12. These give the Kpf values for the overall fuel, selected class fractions including the n,i-paraffins, cycloparaffins, C3 substituted sing-ring aromatics, naphthalenes (primarily the C1 and C2 substituted naphthalenes), and naphthalene. As described above the overall Kpf approximates the volume fraction of absorbed fuel and hence gives an approximation of the volume swell resulting from the absorption of the fuel. Note that this differs from the measurement of the physical volume swell as it reflects only the absorption of fuel and does not include the volume loss resulting from the extraction of the plasticizer. Note that the overall Kpf is only an approximation of the relative volume of absorbed fuel as it assumes that the overall GC-MS response factor for the fuel is fixed when it actually depends on the composition of the absorbed fuel as it compares with the source fuel. Figure 30 summarizes both the volume swell (left) and the overall Kpf values (right). Overall, these show similar trends with the overall Kpf increasing with the aromatic content of the fuel, the Kpf of the Jet A_4 being somewhat depressed as compared with the Jet A and Jet A_25, and the Kpf for the CPK-0 showing levels comparable to a low aromatic Jet A (roughly equivalent to 8.8% aromatics). These results illustrate how the volume swell of nitrile rubber by itself does not necessarily reflect the volume swell imparted by the fuel, but

rather the composite effects of fuel absorption and plasticizer extraction. The overall Kpf values also suggest that the elastomer that comprises these 3 O-ring products are more similar than the volume swell indicates, particularly in the case of the 4457. The differences given by the overall Kpf values, which increase as 4457 < N0602 < N400, may indicate differences in extent of cure (crosslink density) or nitrile content. Recall the solubility tends to decrease as extent of cure and/or the nitrile content increases.

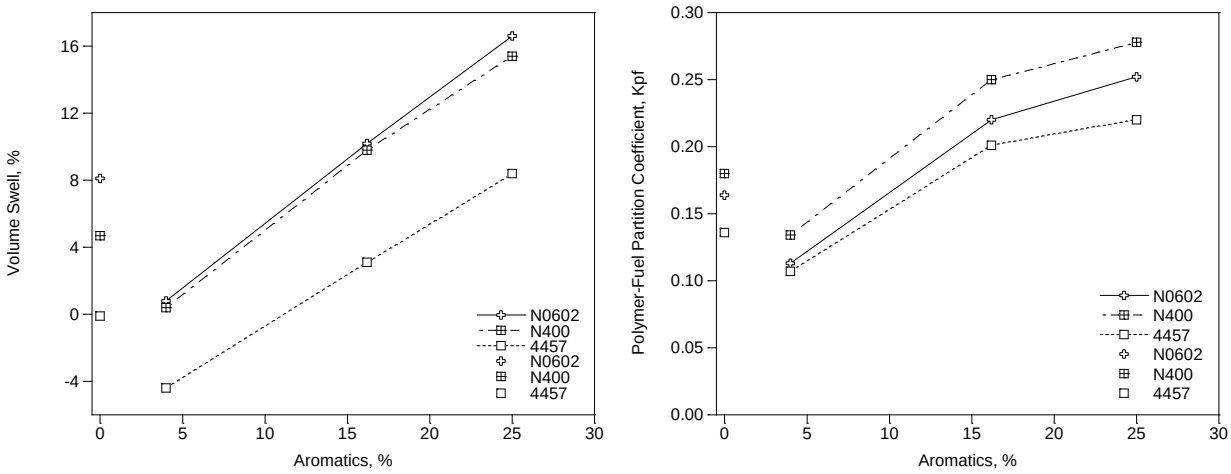

Figure 30. Summary of the volume swell (left) and the overall partition coefficients (right).

Reviewing the partition coefficients for the class fractions given in Table 12 shows a consistent pattern with their solubility increasing as n,i-paraffins < cycloparaffins < aromatics < naphthalenes < naphthalene. It is interesting to note that the Kpf value for naphthalene is typically >1 indicating that nitrile rubber is not only not resistant to this component, it actually accumulates this component from the fuel. Fortunately, the concentration of naphthalene in fuel is quite low (usually less than 1%) and while the levels of naphthalenes can be influential, they generally do not dominate the volume swell. It is also important to note that while the Kpf values for the n,i-paraffins are the lowest among these class fractions, they comprise the largest fraction of the fuel, typically 75-90%. Finally, the Kpf values for the aromatics are intermediate between the paraffins and naphthalenes and are present at sufficient levels (typically 10-25%) to be very influential in determining the volume swell character of the fuel.

Recall that the partition coefficient is the ratio of the concentration of the component or class fraction in the polymer to that in the overlying fuel. Therefore, if the concentration is known in the fuel, the concentration in the elastomer, and hence its contribution to the overall volume swell, can be estimated as given in Table 13. For the purposes of this basic evaluation the class fractions were reduced to the n,i-paraffins, cycloparaffins, and aromatics. These results show that while the aromatics have an important role in determining the volume swell character of the fuel, the paraffins should not be neglected. In particular, it has been found that the molecular weight (molar volume) distribution of the paraffins can have a measurable influence on the volume swell character of the fuel.

Table 13. Estimated Relative Contributions to Volume Swell

Fuel	Class Fraction	N0602	N400	4457	Average
Jet A_4	n,i-Alkanes	72%	71%	69%	71%
	Cycloparaffins	12%	12%	13%	12%
	C3 Aromatics	16%	17%	18%	17%
Jet A	n,i-Alkanes	34%	33%	33%	33%
	Cycloparaffins	28%	28%	28%	28%
	C3 Aromatics	38%	39%	39%	39%
Jet A_25	n,i-Alkanes	28%	27%	27%	27%
	Cycloparaffins	23%	23%	23%	23%
	C3 Aromatics	49%	50%	50%	50%
CKP-0	n,i-Alkanes	3%	3%	3%	3%
	Cycloparaffins	97%	97%	97%	97%
	C3 Aromatics	n.a.	n.a.	n.a.	n.a.

Regarding the CKP-0, the chemical analysis of this fuel shows that it is almost entirely cycloparaffins. Visual inspection of the TICs given in Figure 29 suggests that there is little in the way of preferential absorption of this fuel by the nitrile rubber O-rings used here. To examine this in more detail a cursory survey was made of the partition coefficients as a function of chromatographic retention time was conducted as shown in Figure 31. Overall, this result is consistent with the Kpf values listed in Table 12 which give the average Kpf for the CKP-0 of 0.160.

Prior work has shown that solubility within a given class fraction tends to decrease as molecular weight and molar volume increases. Recalling that molecular weight increases with chromatographic retention time for the analysis shown here a decline in the Kpf with increasing retention time would be expected as shown in Figure 31. (See the example of AMS5315 in JP-5, a fuel like Jet A, shown in Figure 32.)

It is interesting to note that the decline in Kpf over the boiling range of CPK-0 is relatively limited indicating that most of the components of this fuel contribute relatively equally to the volume swell character of the fuel. Interestingly, the prominent outlier giving a lower-than-average Kpf is pentylcyclohexane while the three examples showing elevated Kpf values are all di-cycloparaffins, which is consistent with prior work with cycloparaffins. For example, cycloparaffins with long aliphatic pendant groups are known to have reduced solubility due to an increase in molar volume and a decrease in polarity while di-cycloparaffins show an elevated solubility due to a slight reduction in molar volume and a localization of charge in the C-C bridge bond giving rise to localized polarity in their molecular structure. Overall, this is an interesting result in that it illustrates that the volume swell character of CPK-0 fuel is a general property of this fluid and does not rely on the activity of specific components and therefore should be a very stable, predictable fluid with respect to its volume swell behavior both as a neat fuel and as a blend.

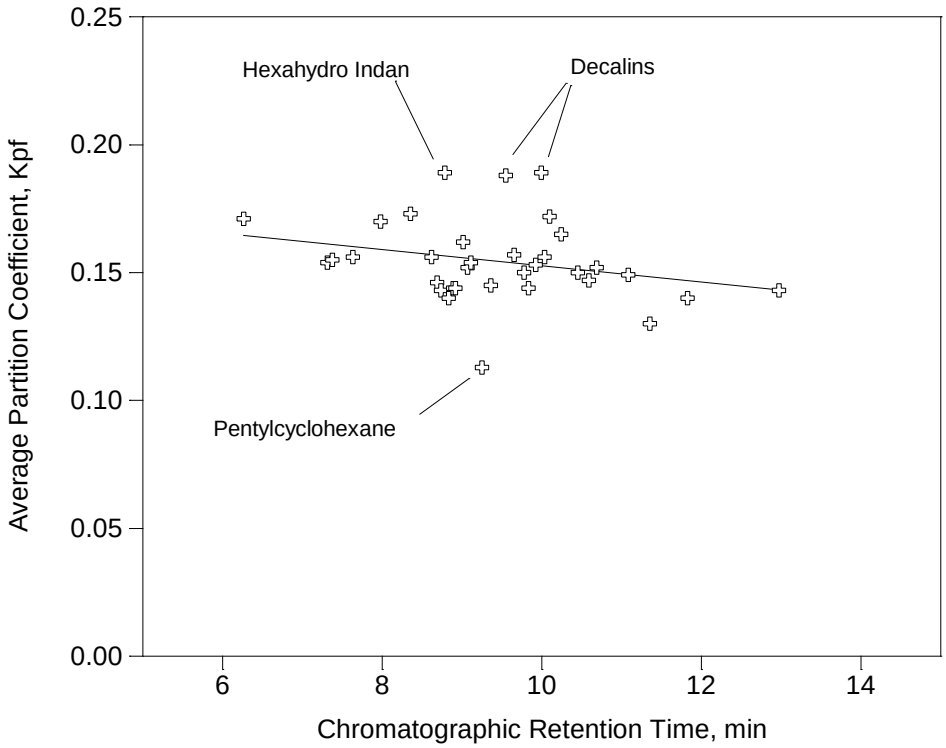

Figure 31. Summary of the average partition coefficients for the CKP-0 absorbed by the nitrile rubber O-rings.

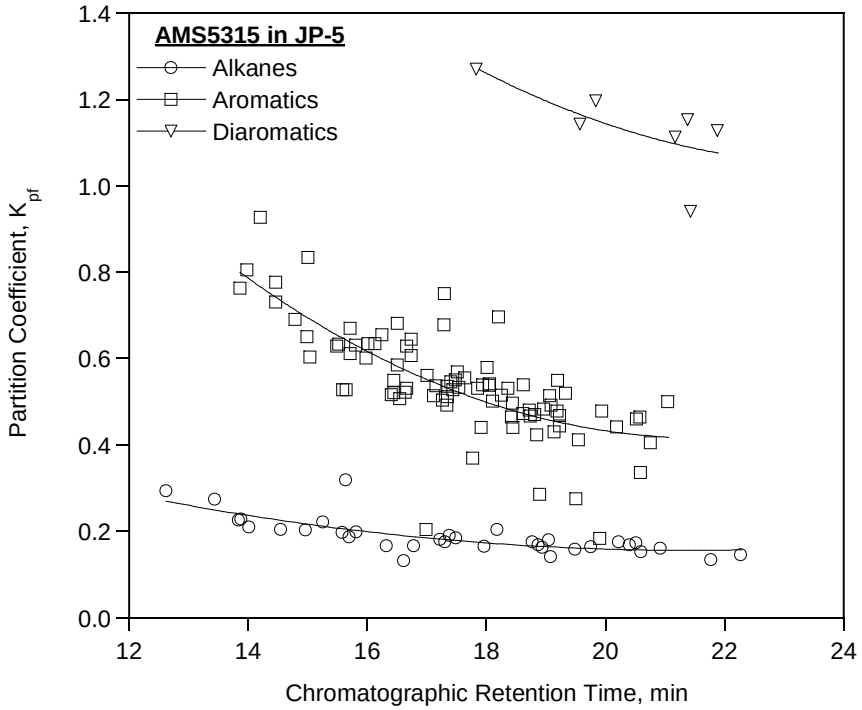

Figure 32. Example of the partition coefficients as a function of chromatographic retention time (molecular weight) for AMS5315 (N0602) O-rings in JP-5, a fuel that is similar to Jet A.

Task 2 – Compression, Compression Set, and Volume Swell

In this task the compression and compression set were measured of all of the test materials while being compressed in the UDRI compression fixtures as shown in Figure 1. The test fluids included Jet A fuels with high (25%, Jet A_25), average (16.2%, Jet A_16), and low (4%, Jet A_4) aromatics. The test fixtures were aged at 160˚F to match the conditions specified for AMS5315 O-rings in ASTM D4054. The average diameter in the axial (compressed) direction was measured every 2 weeks over a period of 25 weeks in accordance with ASTM D395 with the variance that the UDRI fixtures were used. To ensure that the results are statistically significant, and that sufficient O-rings are available for post compression set testing, 8 O-rings were used for each test. The compression and compression set values reported below are the average of these 8 specimens. A subset of 5 O-rings were used to evaluate the post-run tensile, elongation, and modulus, and 3 O-rings were used to evaluate the post-run hardness, glass transition temperature, and IR spectra.

Post Compression-Set Physical Properties

After the completion of the compression set evaluation selected physical properties were measured as summarized in Table 14. To condition the O-rings into a common state the test pieces aged in Jet A_4 and Jet A_25 were removed from their respective test fuels, dabbed dry with a laboratory tissue, and placed in Jet A_16 for 1 week at room temperature. The O-rings were then removed from the Jet A_16, dabbed dry, and placed in a fresh volume of Jet A_16 for an additional week. The test pieces were stored in Jet A_16 until their post-run testing was conducted. After these tests were completed 3 O-rings from each set were returned to their original test fuels for 2 weeks prior to additional testing.

Table 14. Task 2 Post-Compression Set Tests

Property	Method	Notes
Hardness, Type M	ASTM D2240	Shore M
Tensile	ASTM D1414	Tensile Strength
Elongation	ASTM D1414	Ultimate Elongation
Modulus	ASTM D1414	Concurrent with ASTM D1414
IR Spectrum	ATR	Attenuated Total Reflectance
Glass Transition	ASTM E1545	Thermomechanical Analysis

Initial Diameter

Prior to installing the O-rings in the test fixtures the diameter of each test piece was measured in the axial (compressed) direction. Briefly, the axial diameter was measured at 3 locations on each O-ring and the average value was taken as the mean diameter for that test piece. The global average from all 8 O-rings was taken as the mean diameter for each set. Noting that prior work has shown that once an O-ring has been placed in service it fully responds to the fuel in about 7 days at ambient temperature and at elevated temperature this process likely occurs relatively quickly, therefore the

effective average initial diameter of the O-rings was corrected by the linear swell derived from the volume swell as measured in Task 1. These data are summarized in Table 15 which lists the initial average dry diameter and estimated wet diameter for each material and each fuel. Note that this correction has a small influence on the calculation of the compression set by using the initial swollen diameter as the reference state rather than the initial dry diameter. This has no effect on the calculation of the important engineering performance value of O-ring compression as this is based solely on the measured axial diameter.

Table 15. Average Diameter

Material	Fuel	Aromatics % v/v	Swell % v/v	Swell % l/l	Dry D0 in.	Wet D0 in.
N0602	Jet A_4	4.0	0.8	0.3	0.1380	0.1384
	Jet A_16	16.2	10.2	3.3	0.1376	0.1422
	Jet A_25	25.0	16.6	5.3	0.1379	0.1451
N400	Jet A_4	4.0	0.4	0.1	0.1379	0.1380
	Jet A_16	16.2	9.8	3.2	0.1378	0.1421
	Jet A_25	25.0	15.4	4.9	0.1377	0.1444
4457	Jet A_4	4.0	-4.4	-1.5	0.1390	0.1369
	Jet A_16	16.2	3.1	1.0	0.1390	0.1404
	Jet A_25	25.0	8.4	2.7	0.1379	0.1425

Average Compression Diameter

The measured average compression diameter is the primary metric used to evaluate the root behavior of the O-rings when aged in the different fuels and the parameter used to calculate the compression and compression set. The measured average compression diameter as a function of time, fuel, and material is summarized in Table 16. These results are grouped by material in Figures 33-35, and by fuel in Figures 36-38. Overall, the results grouped by material in Figure 33-35 show that the behavior of the N0602 and N400 were very similar and showed the greatest change in the compression diameter as the aromatic content of the fuel declined from 25% to 4%. In contrast, the decline in the compression diameter of the 4457 material was relatively modest. The results grouped by fuel in Figures 36-38 show that as the aromatic content of the fuel declined there was greater discrimination between the materials with the compression diameter declining as N0602 < N400 < 4457. Interestingly, the O-rings aged in the Jet A_25 fuel showed little difference in the average compression diameter.

Table 16. Average Diameter

Time wks	N0602 Average Diameter, in			N400 Average Diameter, in			4457 Average Diameter, in		
	Jet A_4	Jet A_16	Jet A_25	Jet A_4	Jet A_16	Jet A_25	Jet A_4	Jet A_16	Jet A_25
0	0.1384	0.1422	0.1451	0.1380	0.1421	0.1444	0.1369	0.1404	0.1425
2	0.1289	0.1330	0.1342	0.1290	0.1329	0.1340	0.1289	0.1325	0.1333
4	0.1266	0.1307	0.1330	0.1271	0.1307	0.1326	0.1273	0.1311	0.1323
6	0.1254	0.1289	0.1318	0.1256	0.1292	0.1315	0.1266	0.1298	0.1316
8	0.1234	0.1278	0.1305	0.1240	0.1281	0.1304	0.1251	0.1291	0.1303
10	0.1223	0.1270	0.1293	0.1229	0.1273	0.1292	0.1246	0.1282	0.1294
12	0.1213	0.1259	0.1286	0.1224	0.1266	0.1286	0.1238	0.1276	0.1286
14	0.1201	0.1245	0.1274	0.1215	0.1255	0.1275	0.1228	0.1266	0.1275
16	0.1192	0.1236	0.1262	0.1204	0.1242	0.1262	0.1219	0.1254	0.1263
18	0.1185	0.1229	0.1253	0.1197	0.1235	0.1256	0.1215	0.1247	0.1256
20	0.1182	0.1222	0.1248	0.1196	0.1230	0.1251	0.1212	0.1243	0.1248
22	0.1171	0.1211	0.1233	0.1185	0.1218	0.1240	0.1204	0.1234	0.1237
24	0.1170	0.1202	0.1226	0.1183	0.1213	0.1235	0.1199	0.1227	0.1230
26	0.1163	0.1196	0.1216	0.1178	0.1209	0.1226	0.1194	0.1219	0.1222

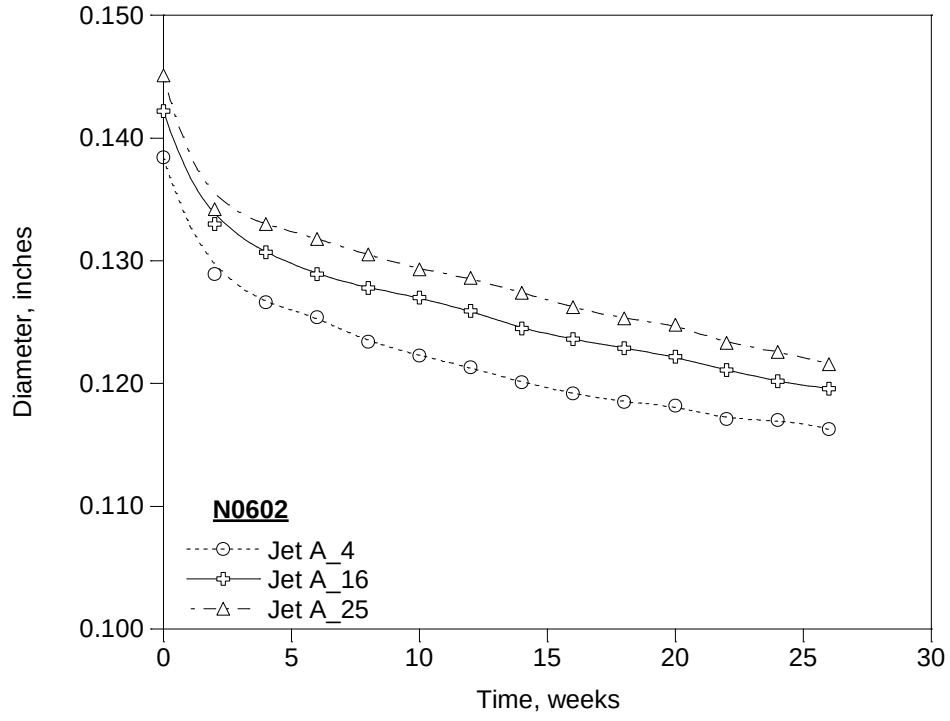

Figure 33. The average diameter of the N0602 O-rings in the test fuels.

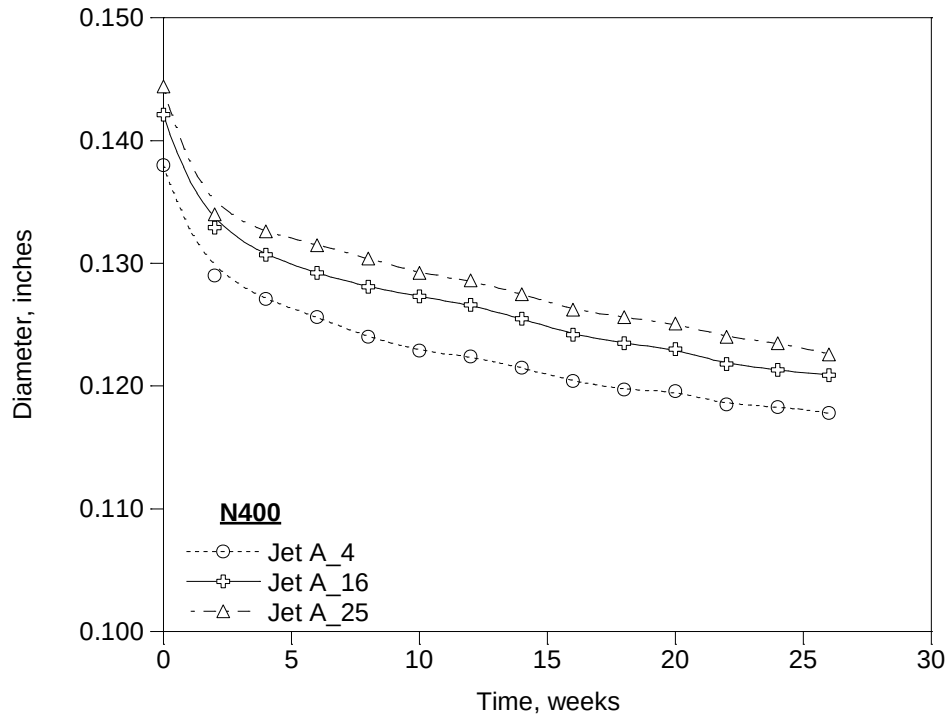

Figure 34. The average diameter of the N400 O-rings in the test fuels.

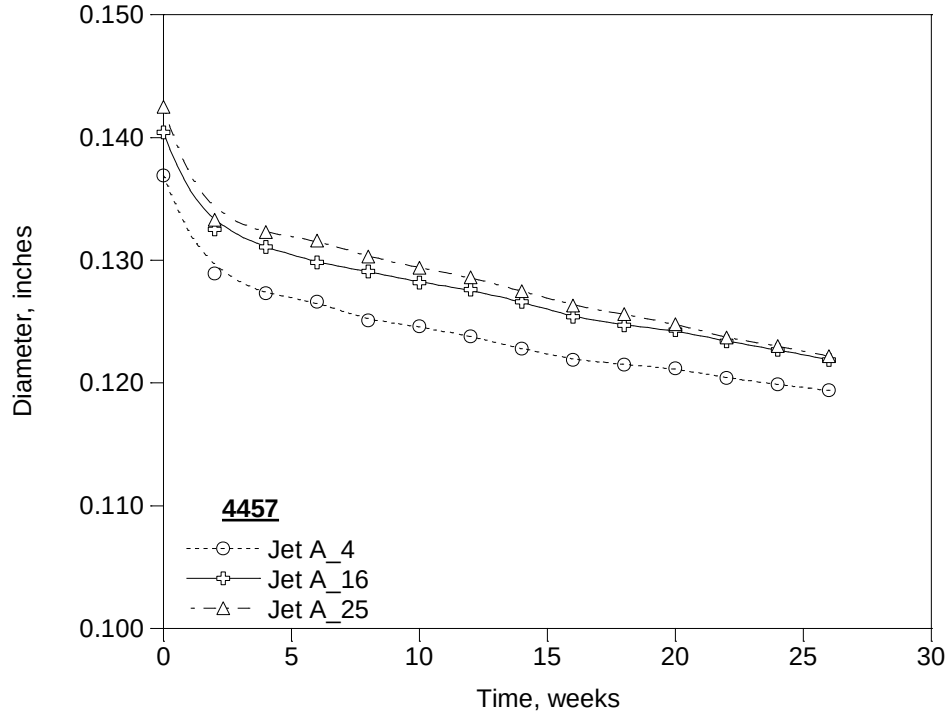

Figure 35. The average diameter of the 4457 O-rings in the test fuels.

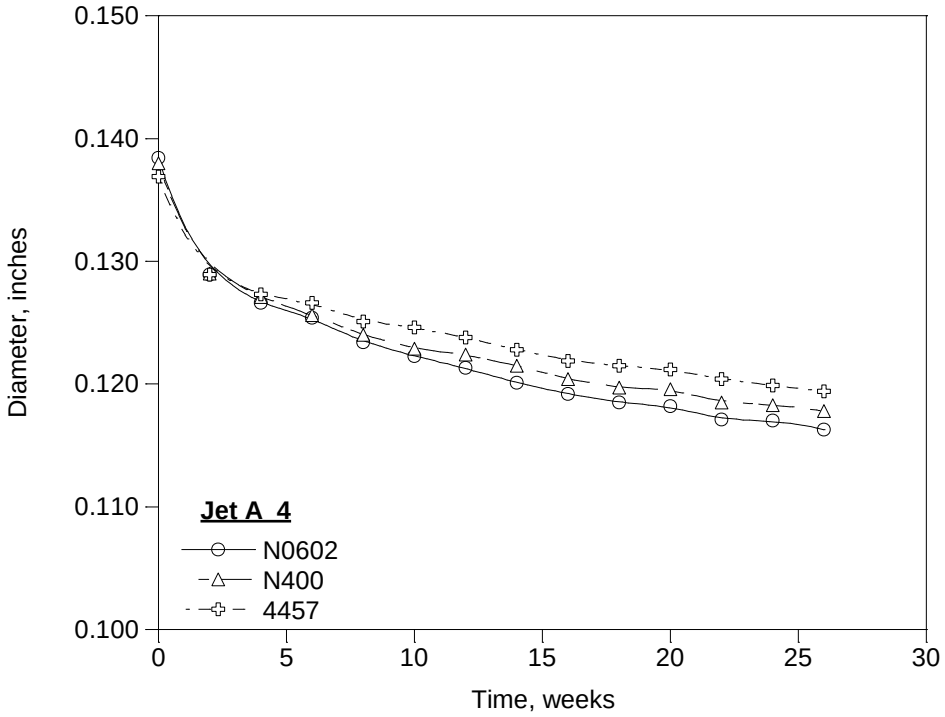

Figure 36. The average diameter of the test O-rings in the Jet A_4 fuel.

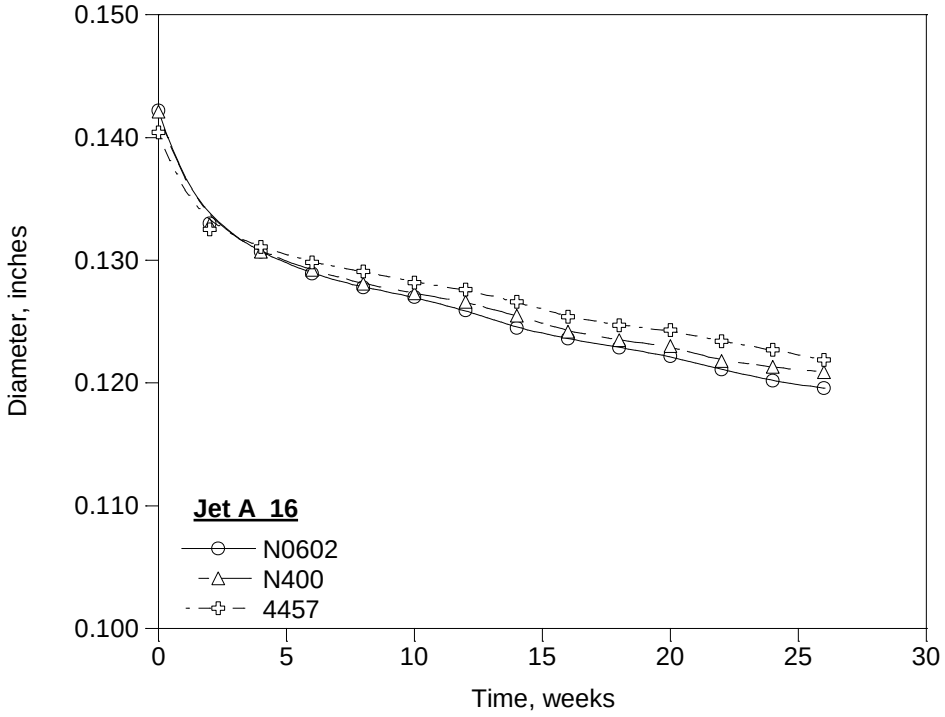

Figure 37. The average diameter of the test O-rings in the Jet A_16 fuel.

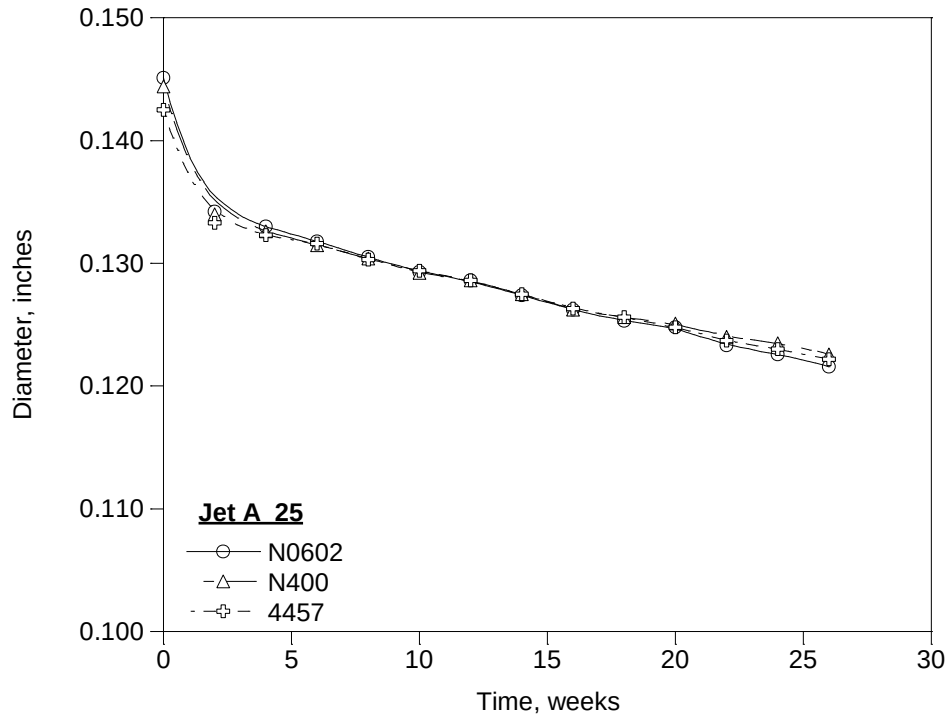

Figure 38. The average diameter of the test O-rings in the Jet A_25 fuel.

To illustrate the effect of the aromatic content more clearly on the diameter of the test O-rings the average final compression diameter for each of the test materials in each of the test fuels is summarized in Table 17 and Figure 39. These illustrate how the compression diameter increases with the aromatic content, though the magnitude of the variation is relatively small. For example, these results show that as the fuel is switched from Jet A_25 to Jet A_4 the compression diameter of the N0602 O-rings will shrink by approximately 0.005" and the 4457 O-rings will shrink by 0.003". This suggests that to transition from a sealing condition to a leaking condition when the fuel is switched from Jet A_25 to Jet A_4 the diameter of the O-rings need to be within 0.003-0.005" of an end of service condition.

Table 17. Final Average Diameter

Fuel	Aromatics	Final Diameter, in.		
		N0602	N400	4457
Jet A_4	4.0%	0.1163	0.1178	0.1194
Jet A_16	16.2%	0.1196	0.1209	0.1219
Jet A_25	25.0%	0.1216	0.1226	0.1222
Variation, in		0.0053	0.0048	0.0028

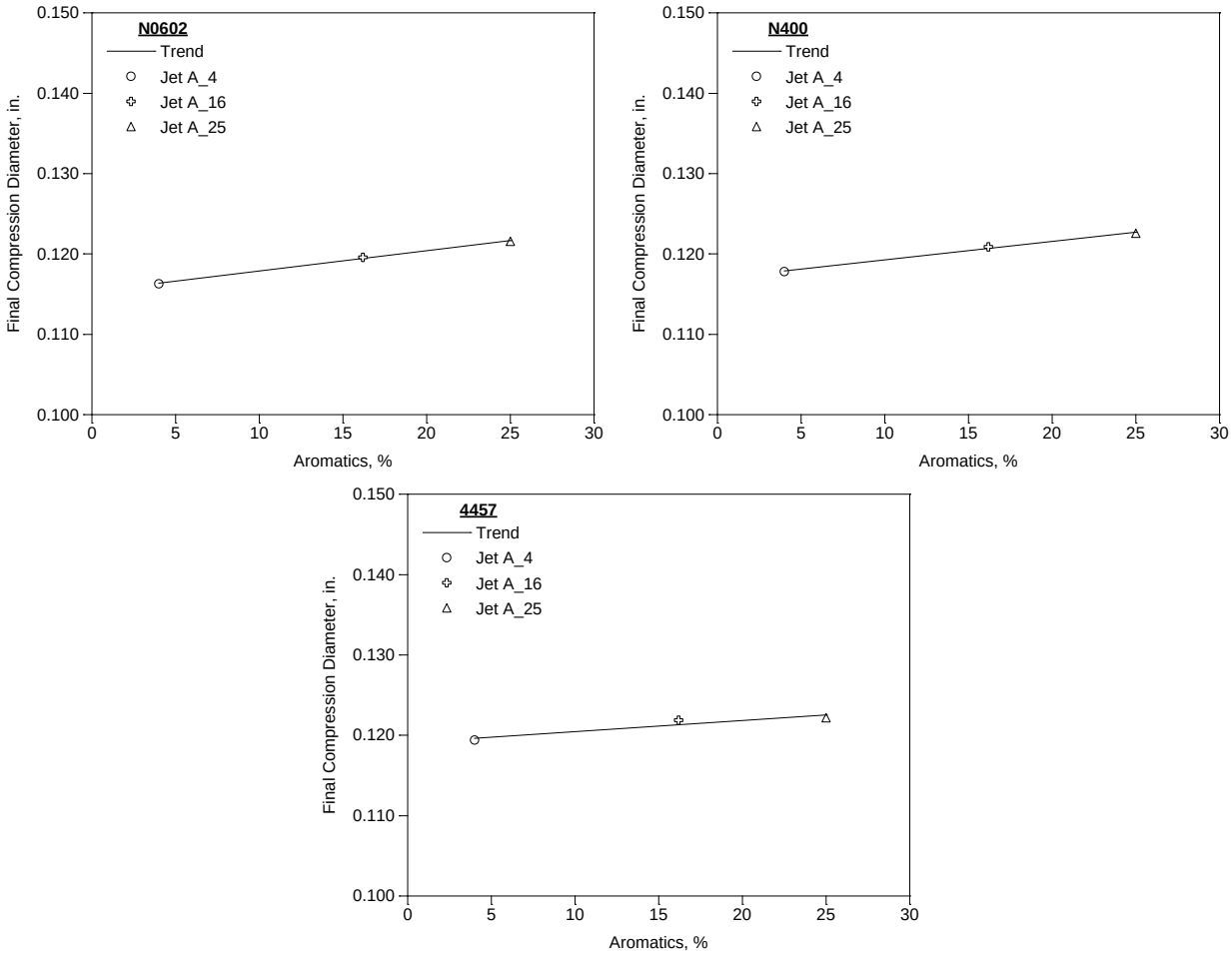

Figure 39. The average final diameter of the test O-rings as a function of the aromatic content of the test fuels.

Average Compression

Compression is one of the most important parameters that reflect the engineering performance of an O-ring seal. Static compression seals are typically design around an initial compression of 25% based on the as-received diameter of the O-ring and prior work as shown that static O-ring seals can become vulnerable to leaks at pressures up to 60 psi when the compression drops below approximately 5%.

The measured average compression as a function of time, fuel, and material is summarized in Table 18. These results are grouped by material in Figures 40-42, and by fuel in Figures 43-45. Overall, the results grouped by material in Figure 30-42 show that the behavior of the N0602 and N400 were very similar and showed the greatest change in compression as the aromatic content of the fuel declined from 25% to 4%. In contrast, the decline in the compression of the 4457 material was relatively modest, though still significant as the aromatic content declined from 16.2% to 4.0%. The results grouped by fuel in Figures 43-45 show that as the aromatic content of the fuel

declined there was greater discrimination between the materials with the compression declining as N0602 < N400 < 4457. Interestingly, the O-rings aged in the Jet A_25 fuel showed little difference in the average compression.

Table 18. Average Compression

Time	N0602			N400			4457		
	Average Compression, %			Average Compression, %			Average Compression, %		
wks	Jet A_4	Jet A_16	Jet A_25	Jet A_4	Jet A_16	Jet A_25	Jet A_4	Jet A_16	Jet A_25
0	24.1	26.1	27.7	23.9	26.1	27.3	23.3	25.2	26.3
2	18.5	21.1	21.8	18.6	21.0	21.7	18.5	20.8	21.2
4	17.1	19.7	21.1	17.4	19.6	20.8	17.5	19.9	20.6
6	16.3	18.5	20.4	16.4	18.7	20.1	17.1	19.1	20.2
8	14.9	17.8	19.5	15.4	18.0	19.5	16.1	18.7	19.4
10	14.1	17.3	18.8	14.6	17.5	18.7	15.7	18.1	18.9
12	13.5	16.6	18.4	14.2	17.0	18.3	15.2	17.7	18.3
14	12.6	15.7	17.6	13.6	16.4	17.6	14.5	17.0	17.7
16	11.9	15.1	16.8	12.8	15.5	16.8	13.9	16.3	16.9
18	11.4	14.5	16.2	12.3	15.0	16.4	13.6	15.8	16.4
20	11.2	14.1	15.8	12.2	14.6	16.0	13.4	15.5	15.9
22	10.4	13.3	14.9	11.4	13.8	15.3	12.8	14.9	15.1
24	10.3	12.7	14.4	11.2	13.4	15.0	12.4	14.4	14.6
26	9.7	12.2	13.6	10.8	13.2	14.4	12.0	13.8	14.1

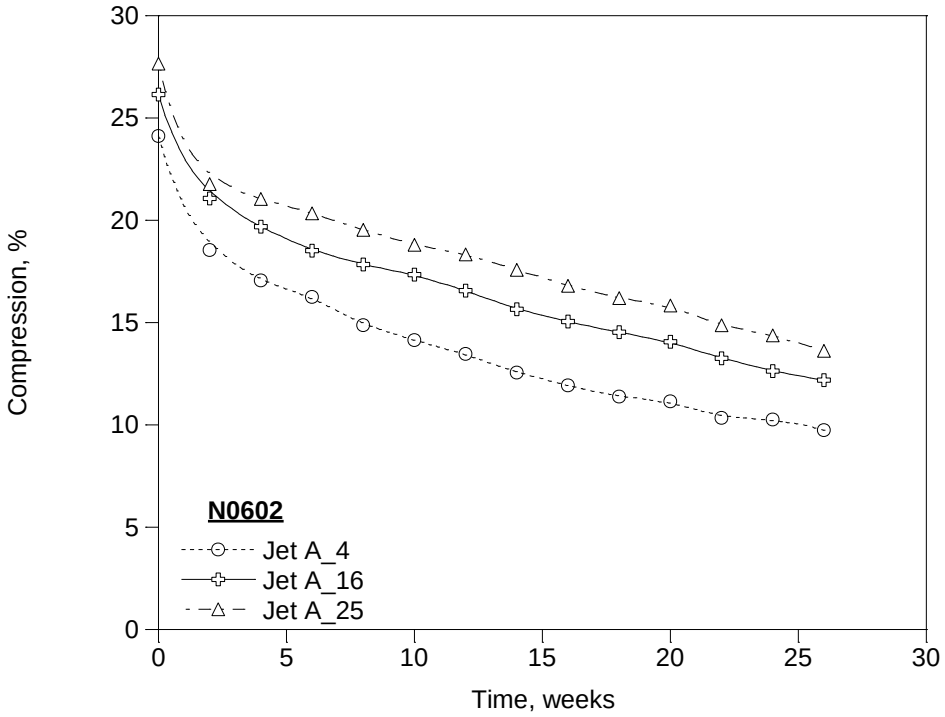

Figure 40. The average compression of the N0602 O-rings in the test fuels.

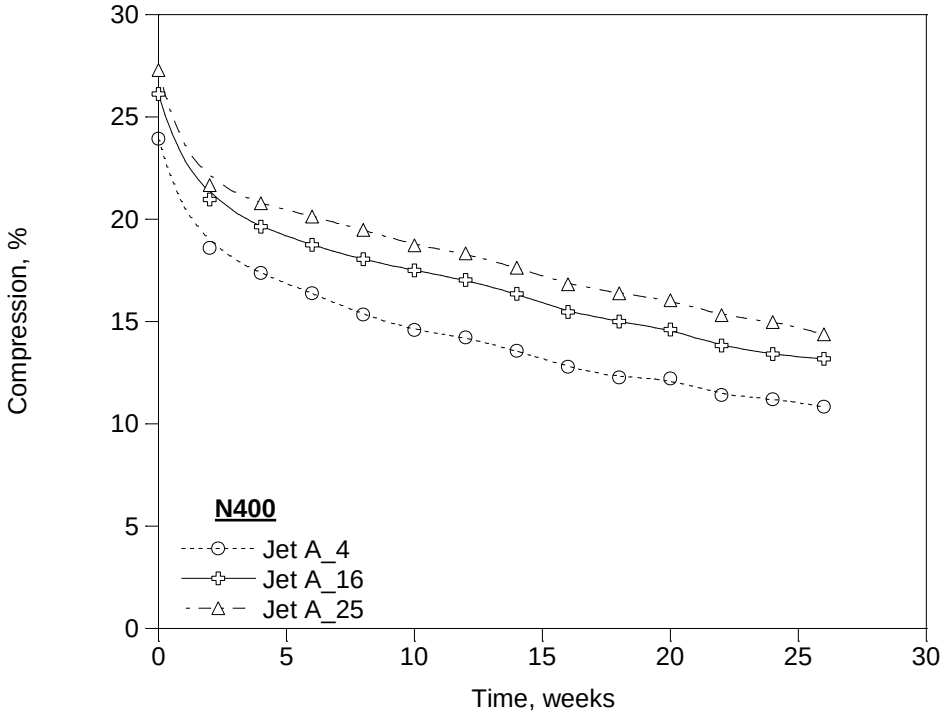

Figure 41. The average compression of the N400 O-rings in the test fuels.

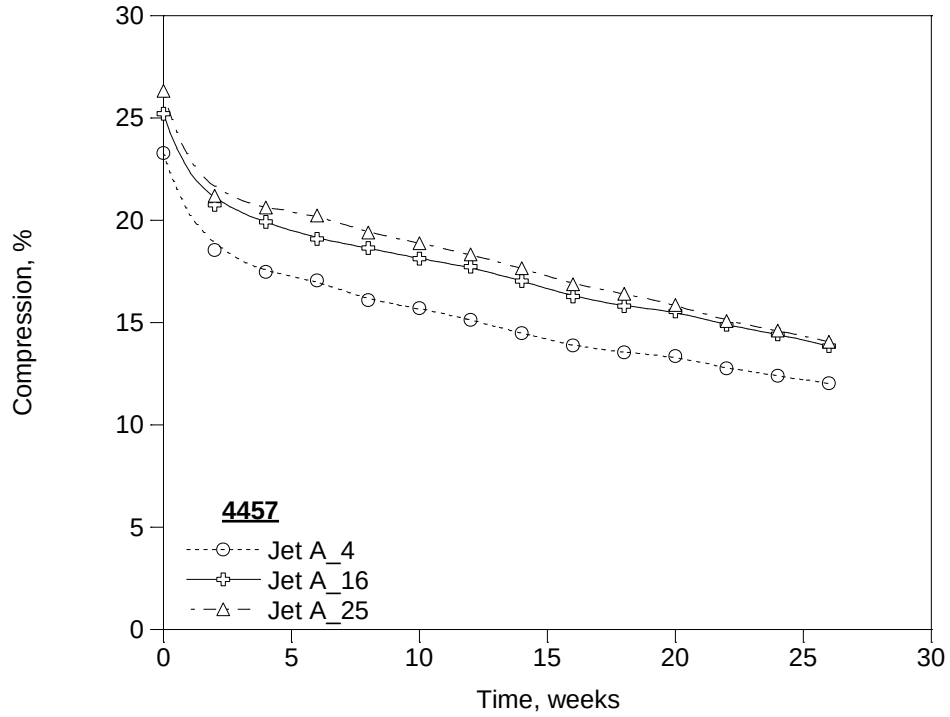

Figure 42. The average compression of the 4457 O-rings in the test fuels.

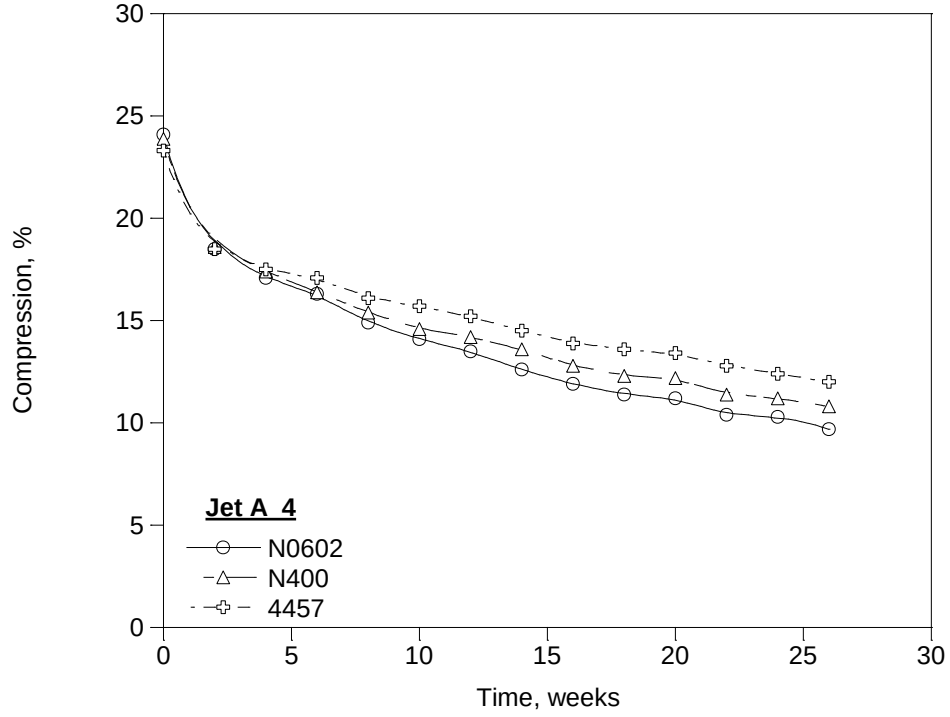

Figure 43. The average compression of the test O-rings in the Jet A_4 fuel.

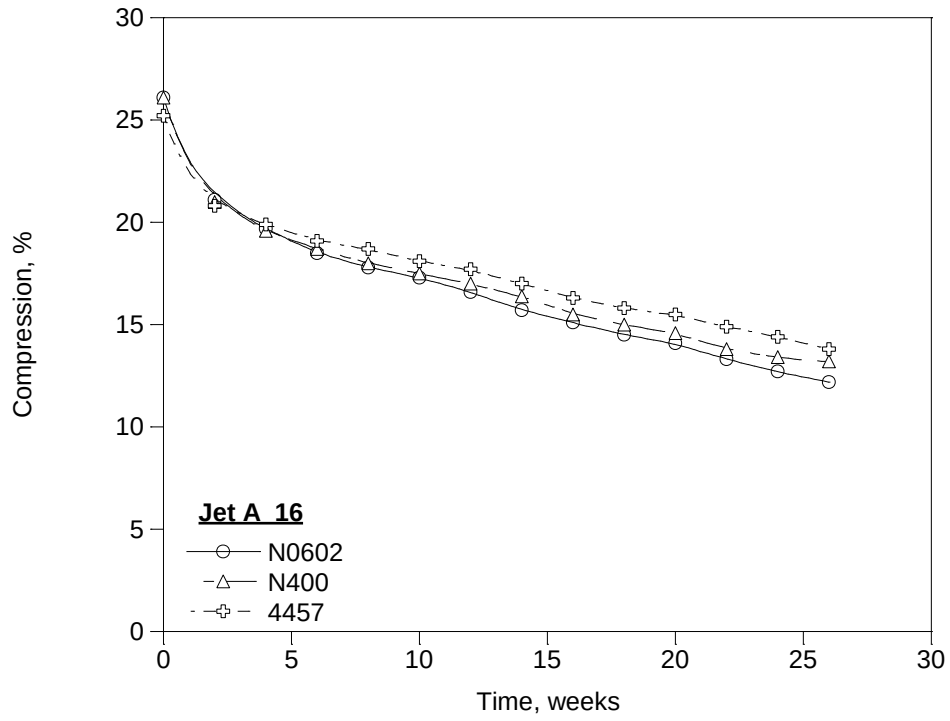

Figure 44. The average compression of the test O-rings in the Jet A_16 fuel.

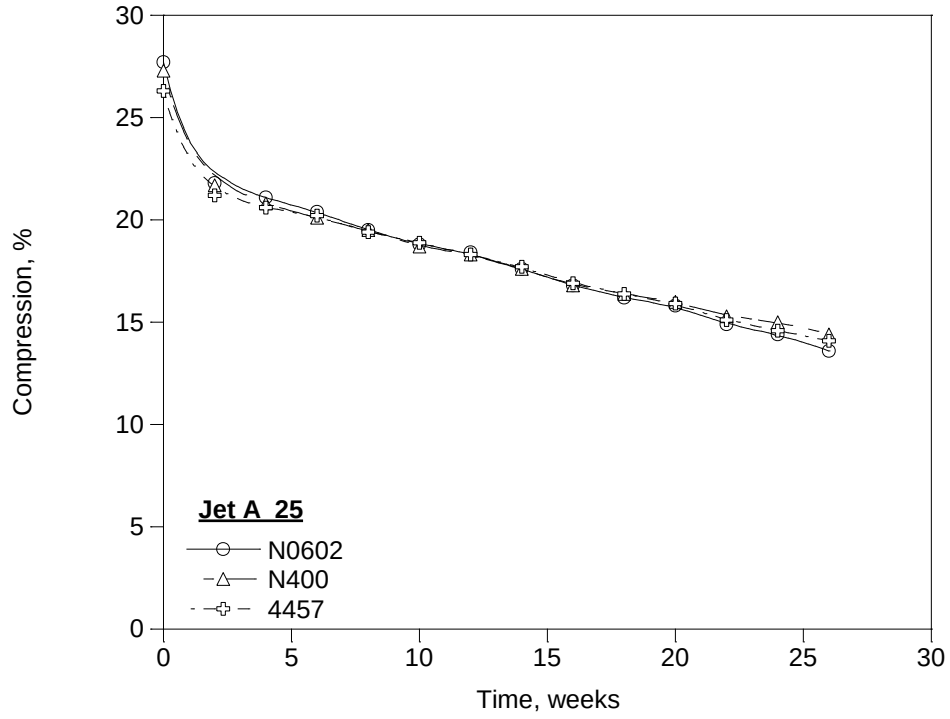

Figure 45. The average compression of the test O-rings in the Jet A_25 fuel.

To illustrate the effect of the aromatic content on the compression of the test O-rings the average final compression for each of the test materials in each of the test fuels is summarized in Table 19 and Figure 46. These illustrate how the compression increases with the aromatic content, though the magnitude of the variation is relatively small. For example, these results show that as the fuel is switched from Jet A_25 to Jet A_4 the compression of the N0602 O-rings lose 2.3% compression, and the 4457 O-rings lose 0.5% compression. This suggests that to transition from a sealing condition to a leaking condition when switching from Jet A_25 to Jet A_4 the compression of the O-rings need to be within 0.5-2.3% of an end of service condition.

Table 19. Final Average Compression

Fuel	Aromatics	Final Compression, %		
		N0602	N400	4457
Jet A_4	4.0%	9.7	12.2	13.6
Jet A_16	16.2%	10.8	13.2	14.4
Jet A_25	25.0%	12.0	13.8	14.1
Variation, %		2.3	1.6	0.5

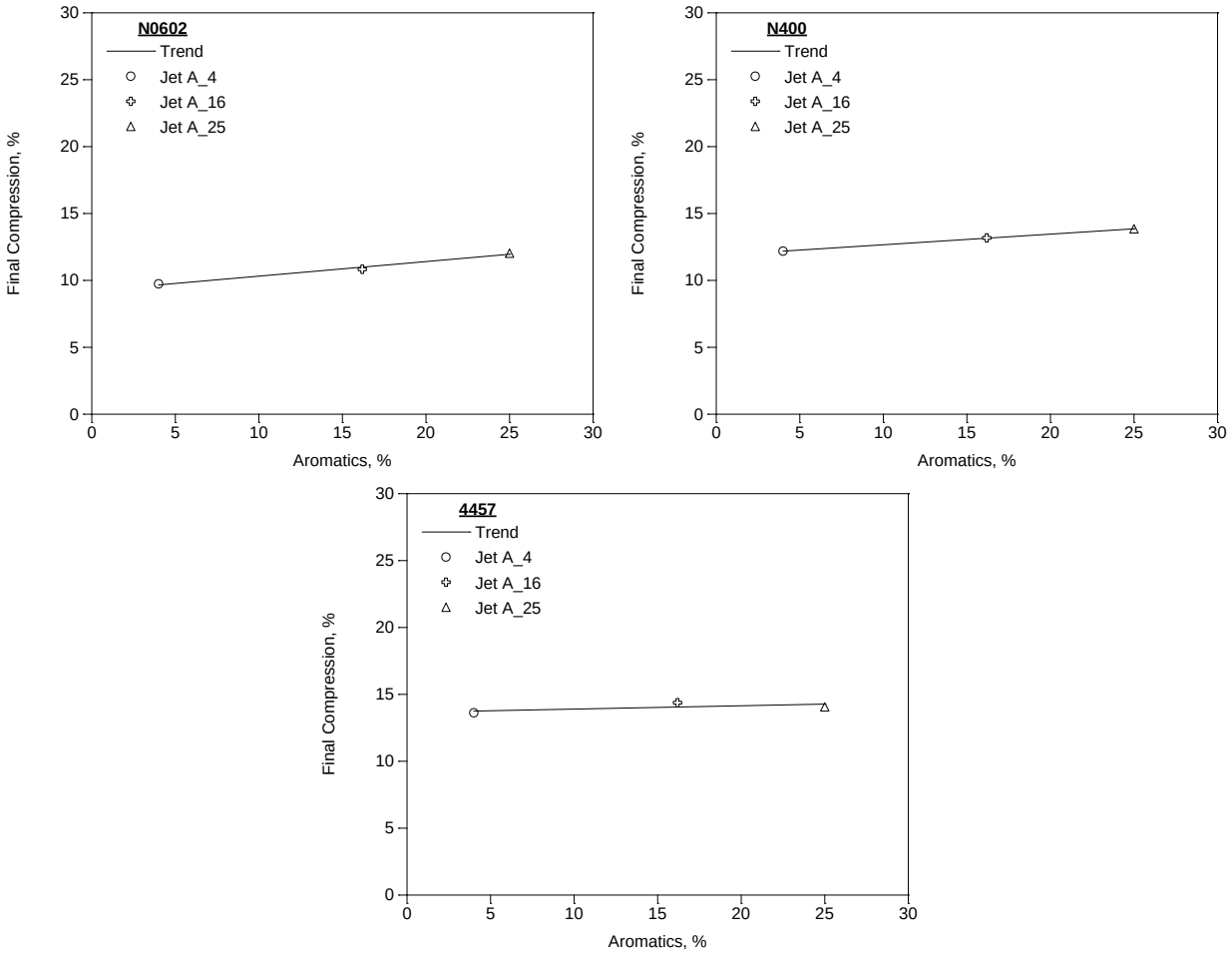

Figure 46. The average final compression of the test O-rings as a function of the aromatic content of the test fuels.

Average Compression Set

Compression set is a measure of the loss of compression due to the viscoelastic flow of the O-ring elastomer while it is compressed in a gland and is often used as an indicator of the relative age of an O-ring. For example, 50% compression set is often taken as an estimate of the end of service condition for an O-ring seal, though the actual end of service condition will depend on the service environment. Prior work with static O-ring seals in fuel service suggests that the actual end of service condition is closer to 80-90% compression set.

The measured average compression set as a function of time, fuel, and material is summarized in Table 20. These results are grouped by material in Figures 47-49, and by fuel in Figures 50-52. Overall, the results grouped by material in Figure 47-49 show that the behavior of the N0602 and N400 were very similar and showed the greatest change in compression set as the aromatic content of the fuel declined from 25% to 4%. In contrast, the increase in the compression set of the 4457 material was relatively modest. The results grouped by fuel in Figures 50-52 show that as the aromatic content

of the fuel declined there was greater discrimination between the materials with the compression set increasing as N0602 > N400 > 4457. Interestingly, the O-rings aged in the Jet A_25 fuel showed comparatively small differences in the average compression set.

Table 20. Average Compression Set

Time	N0602			N400			4457		
	Average Compression Set, %			Average Compression Set, %			Average Compression Set, %		
wks	Jet A_4	Jet A_16	Jet A_25	Jet A_4	Jet A_16	Jet A_25	Jet A_4	Jet A_16	Jet A_25
0	0.0	0.0	0.0	0.0	0.0	0.0	0.0	0.0	0.0
2	28.4	24.5	27.2	27.4	25.0	26.3	25.0	22.3	24.7
4	35.2	30.8	30.2	33.2	30.9	30.0	30.2	26.2	27.3
6	38.9	35.8	33.2	37.8	34.8	32.8	32.2	30.0	29.0
8	45.0	38.6	36.5	42.4	37.8	35.5	36.8	32.0	32.6
10	48.2	40.7	39.4	45.7	40.0	38.6	38.6	34.4	34.9
12	51.0	43.9	41.2	47.3	42.0	40.2	41.2	36.1	37.2
14	54.8	47.5	44.2	50.1	44.7	42.9	44.2	39.1	40.0
16	57.3	49.9	47.2	53.4	48.2	46.1	46.9	42.3	43.2
18	59.6	52.0	49.5	55.6	50.1	47.8	48.4	44.3	45.1
20	60.5	53.8	50.8	55.8	51.6	49.1	49.2	45.4	47.2
22	63.6	56.8	54.3	59.0	54.7	51.8	51.8	48.1	50.3
24	64.0	59.1	56.1	59.9	56.2	53.0	53.3	50.0	52.1
26	66.0	60.8	58.7	61.4	57.1	55.3	55.0	52.3	54.2

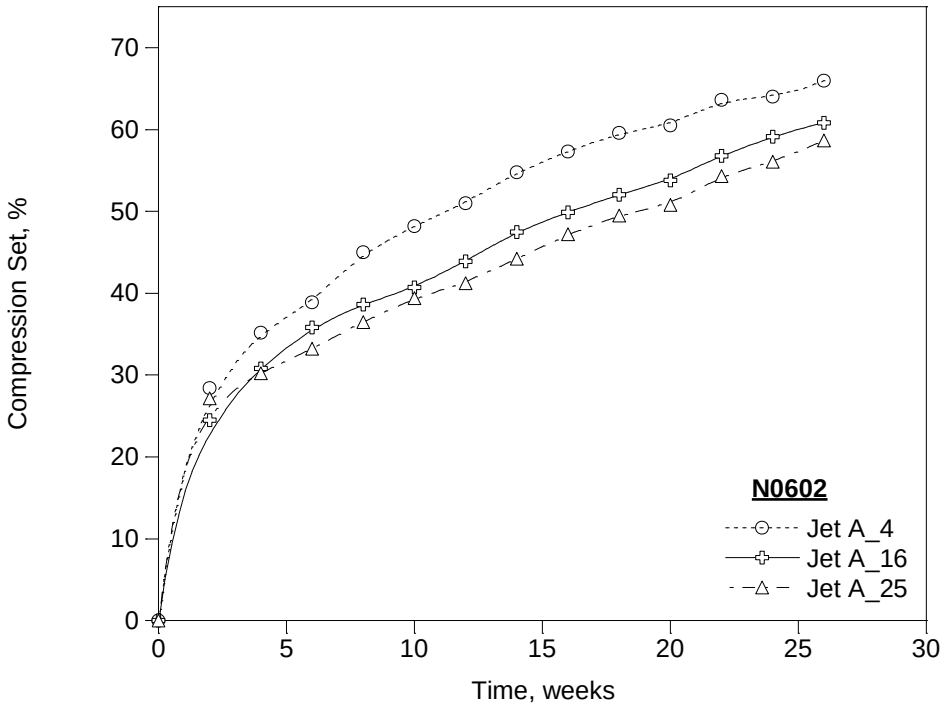

Figure 47. The average compression set of the N0602 O-rings in the test fuels.

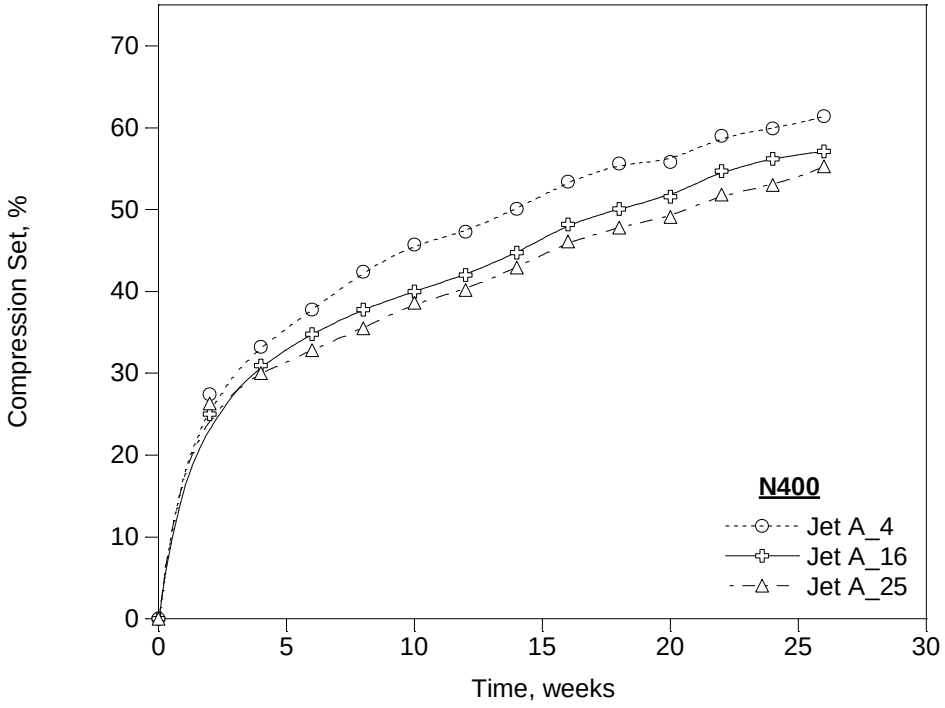

Figure 48. The average compression set of the N400 O-rings in the test fuels.

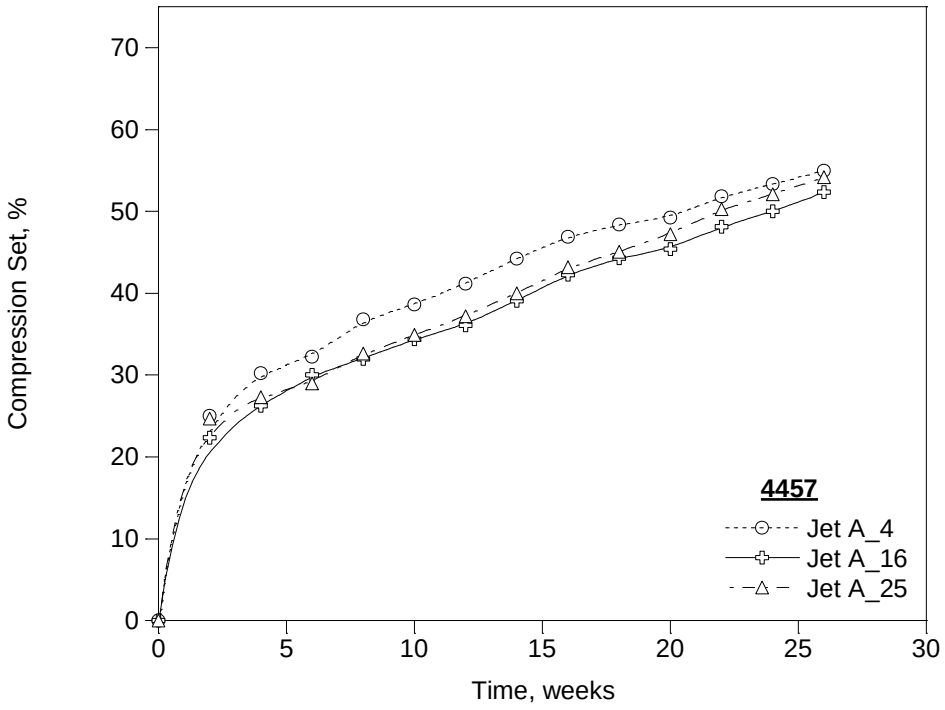

Figure 49. The average compression set of the 4457 O-rings in the test fuels.

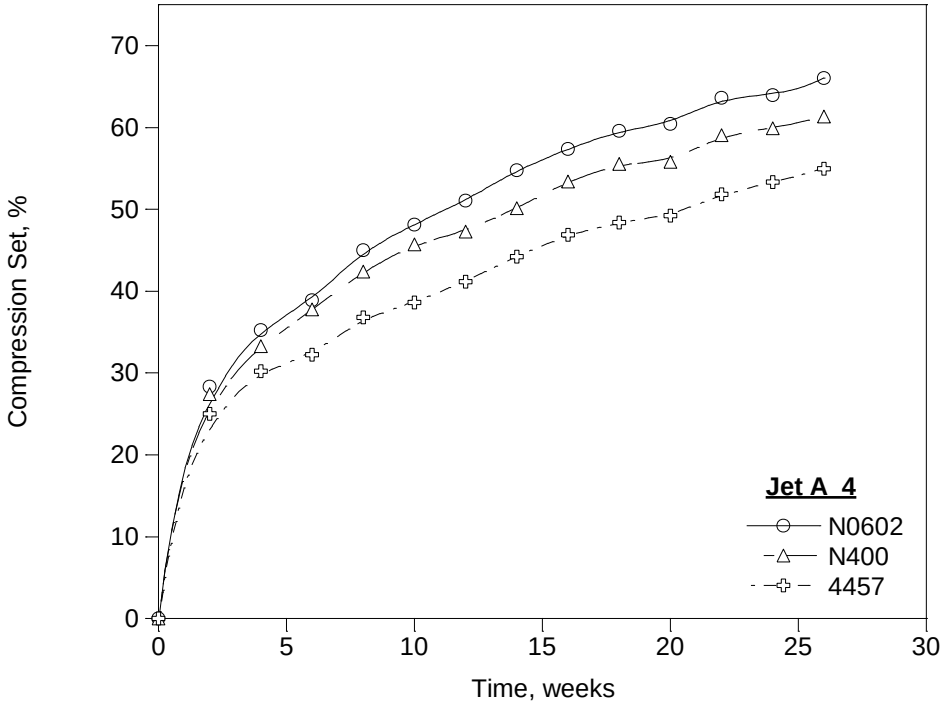

Figure 50. The average compression set of the test O-rings in the Jet A_4 fuel.

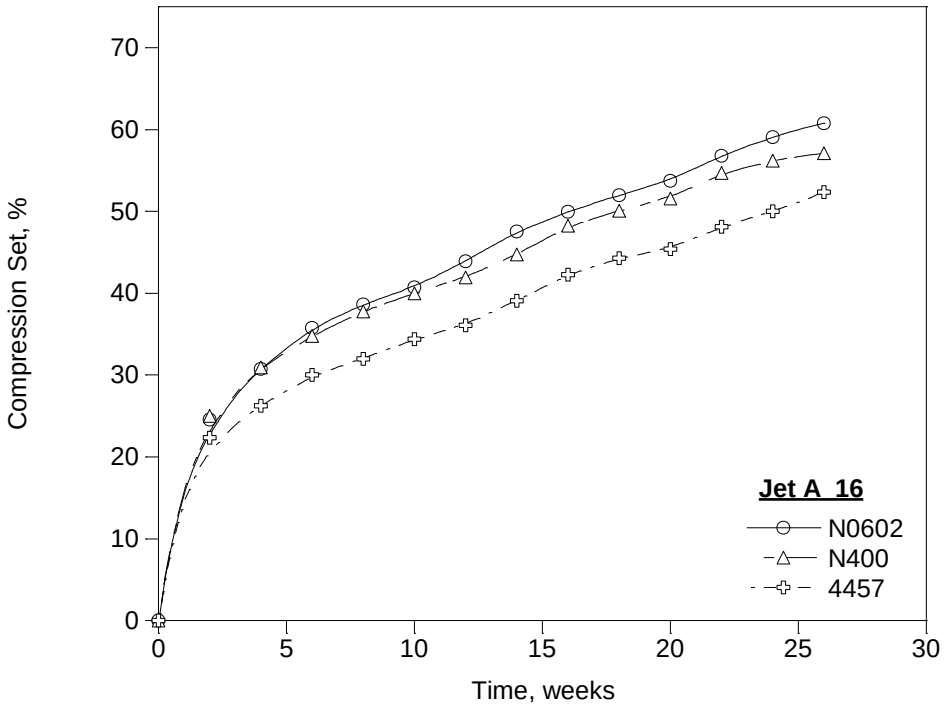

Figure 51. The average compression set of the test O-rings in the Jet A_16 fuel.

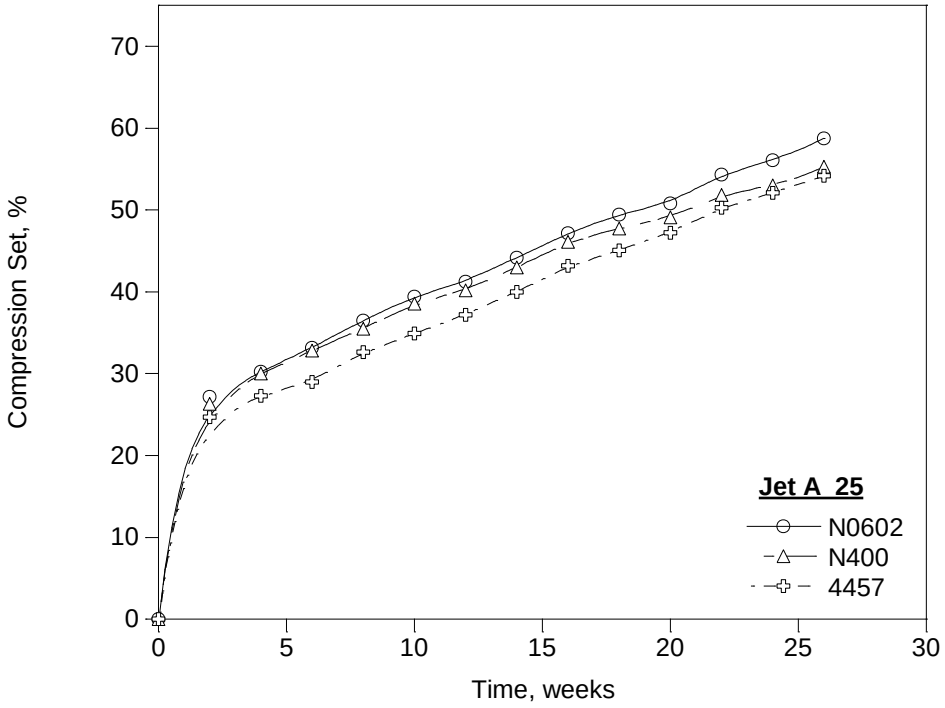

Figure 52. The average compression set of the test O-rings in the Jet A_25 fuel.

To illustrate the effect of the aromatic content on the compression set of the test O-rings the average final compression set for each of the test materials in each of the test fuels is summarized in Table 21 and Figure 53. These show how the compression set decreases with the aromatic content, though the magnitude of the variation is relatively modest. For example, these results show that as the fuel is switched from Jet A_25 to Jet A_4 the compression set of the N0602 O-rings increases by 11.1% and the compression set of the 4457 O-rings increases by 4.6%. This suggests that in order to transition to a nominal end of service condition of 50% compression set when switching from Jet A_25 to Jet A_4 the compression set of the O-rings need to be on the order of 38.9-45.4%. (Note that prior work suggested that the actual end of service condition for static O-ring seals is closer to 80-90% compression set.)

Table 21. Average Final Compression Set

Fuel	Aromatics	Final Compression Set, %		
		N0602	N400	4457
Jet A_4	4.0%	66.0	60.8	58.7
Jet A_16	16.2%	61.4	57.1	55.3
Jet A_25	25.0%	55.0	52.3	54.2
Variation, %		11.1	8.4	4.6

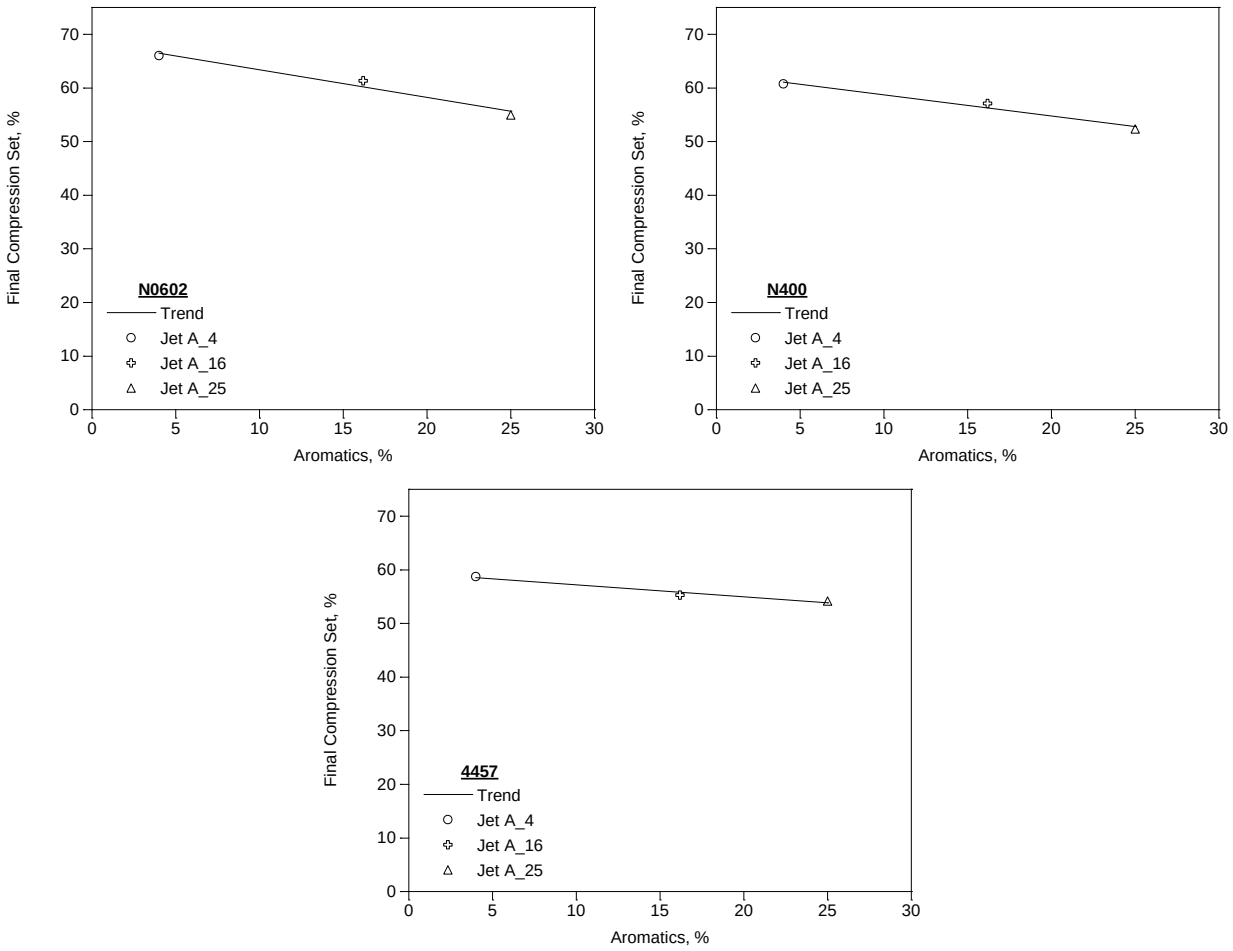

Figure 53. The average final compression set of the test O-rings as a function of the aromatic content of the test fuels.

Post-Compression Physical Properties

As described above, after the completion of the compression set evaluation the O-rings were conditioned into a common state to eliminate fuel matrix effects making a direct comparison of the state of NBR material of O-rings aged in different fuels possible. Briefly, the test pieces aged in Jet A_4 and Jet A_25 were removed from their respective test fuels, dabbed dry with a laboratory tissue, and placed in Jet A_16 for 1 week at room temperature. The O-rings were then removed from the Jet A_16, dabbed dry, and placed in a fresh volume of Jet A_16 for an additional week. The test pieces were stored in Jet A_16 until their post-run testing was conducted. With all the O-rings conditioned in Jet A_16 the tests listed in Table 14 were performed. The results are summarized below.

Hardness

The type M hardness test results are summarized in Table 22 and Figure 54. These

show that the hardness in the post-run O-rings conditioned in Jet A_16 declined as the aromatic content of the test fuel increased. It is interesting to note that the O-rings stressed in the Jet A_4 tended to be somewhat softer than the baseline O-rings, the O-rings stressed in Jet A_16 were similar in hardness to the baseline O-rings, and the O-rings stressed in Jet A_25 tended to be somewhat harder than the baseline O-rings.

Table 22. Type M Hardness

Fuel	Aromatics	Hardness, Type M		
		N0602	N400	4457
None	n.a.	76.5	79.0	77.1
Jet A_4	4.0%	82.3	80.4	81.3
Jet A_16	16.2%	79.3	78.2	79.1
Jet A_25	25.0%	72.3	75.3	77.8

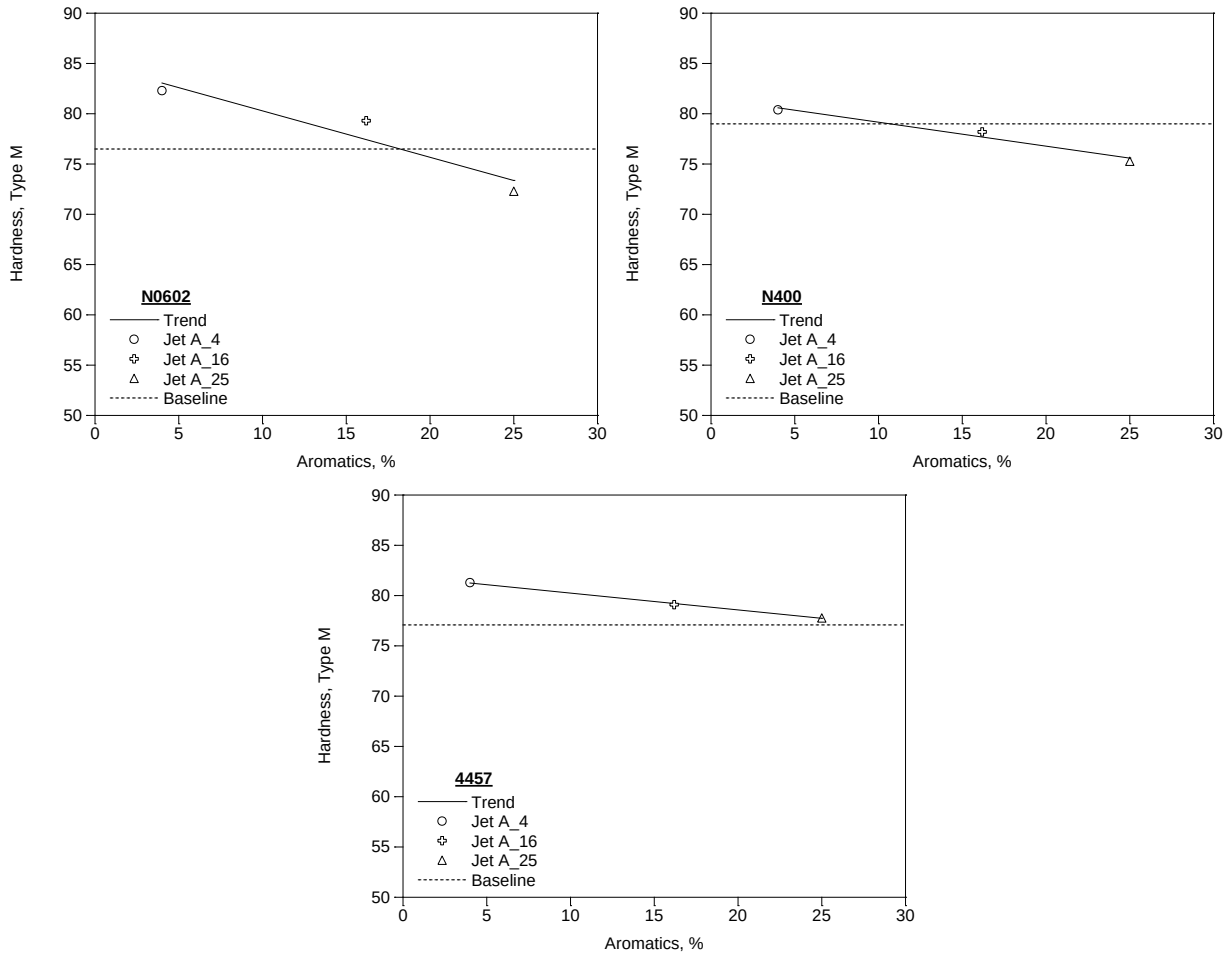

Figure 54. Summary of the post-compression set Type M hardness along with the baseline hardness as measured in Task 1.

Tensile

The tensile test results are summarized in Table 23 and Figure 55. These show that the tensile in the post-run O-rings conditioned in Jet A_16 declined as the aromatic content of the test fuel increased. This is most notable for the N0602 O-rings which showed a tensile in Jet A_4 that was similar to the baseline O-rings, but sharply declined as the aromatic content of the fuel increased. The decline in tensile for the N400 and 4457 O-rings were more modest, but the tensile of the N400 O-rings were always less than the baseline values while the tensile of the 4457 was higher than the baseline in Jet A_4 and less than the baseline in Jet A_25.

Table 23. Tensile

Fuel	Aromatics	Tensile, psi		
		N0602	N400	4457
None	n.a.	1757	1937	1429
Jet A_4	4.0%	1772	1710	1649
Jet A_16	16.2%	1203	1618	1507
Jet A_25	25.0%	926	1472	1115

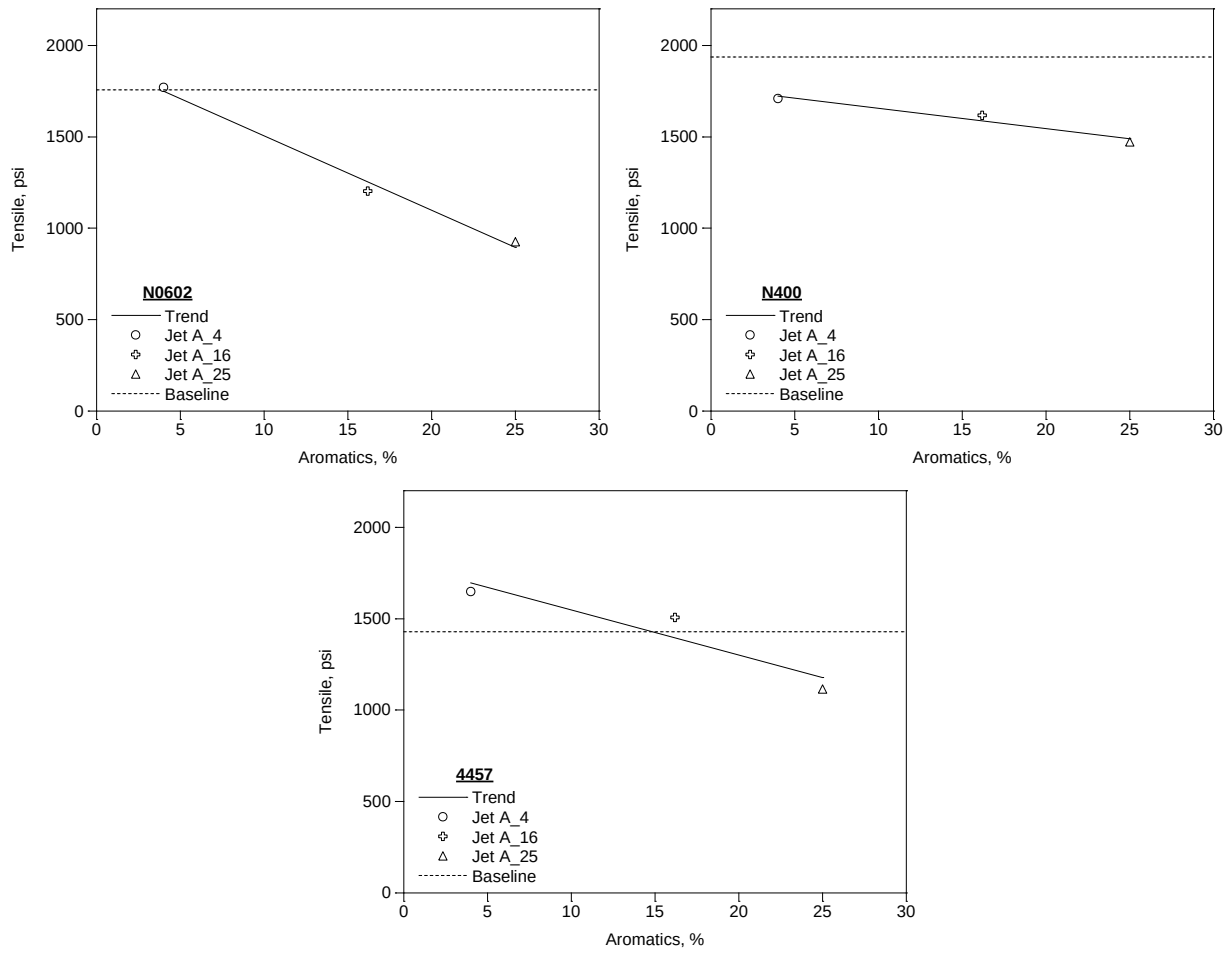

Figure 55. Summary of the post-compression set tensile along with the baseline tensile as measured in Task 1.

Elongation

The elongation test results are summarized in Table 24 and Figure 56. These show that the elongation in the post-run O-rings conditioned in Jet A_16 declined as the aromatic content of the test fuel increased. Most notably, all of the O-rings showed a significant reduction in elongation in all of the test fuels as compared to their respective baselines.

Table 24. Elongation

Fuel	Aromatics	Elongation, %		
		N0602	N400	4457
None	n.a.	308	255	234
Jet A_4	4.0%	135	153	142
Jet A_16	16.2%	103	150	132
Jet A_25	25.0%	81	143	102

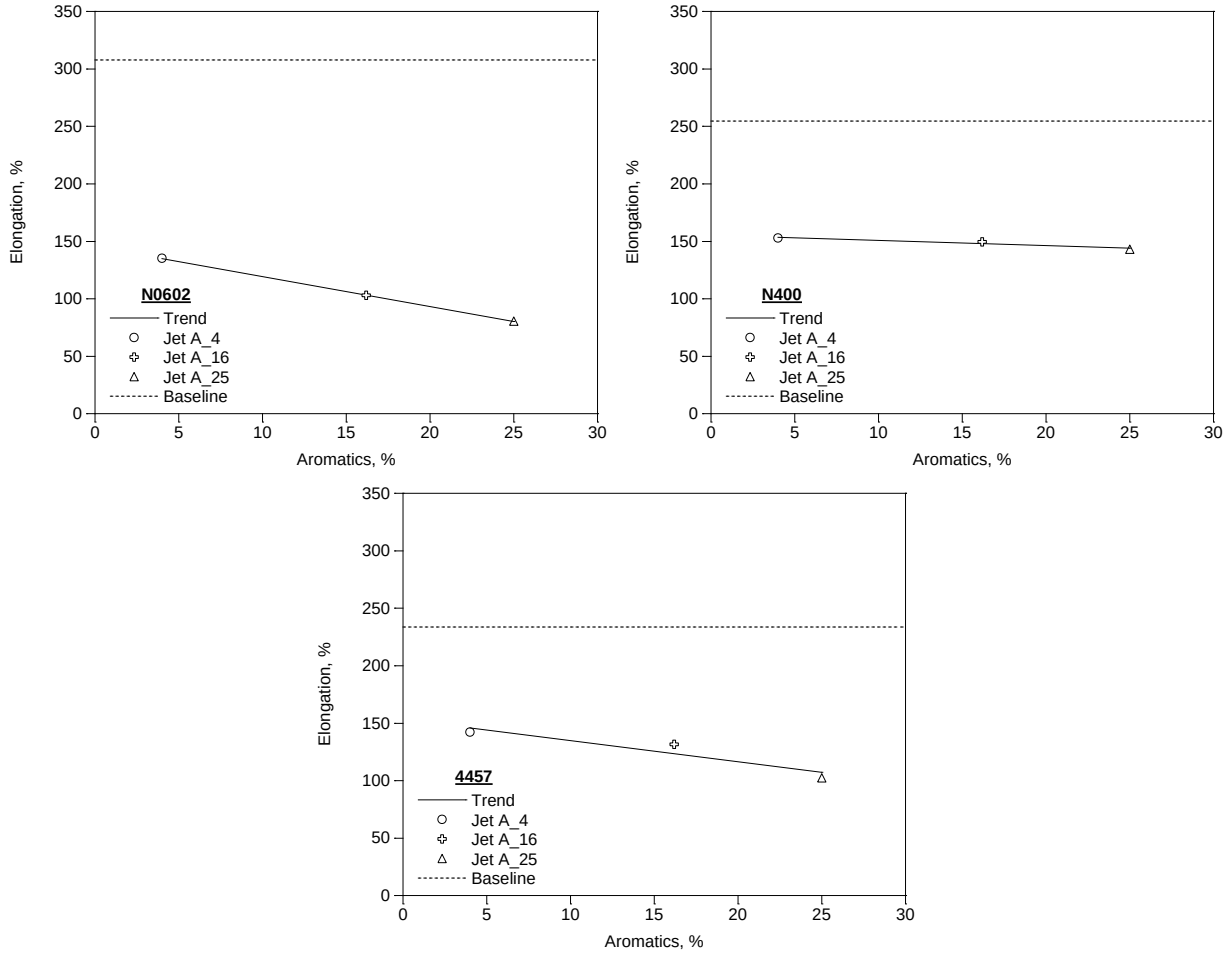

Figure 56. Summary of the post-compression set elongation along with the baseline elongation as measured in Task 1.

Modulus at 100% Elongation

The stress/strain test results extracted from the tensile and elongation tests are summarized in Figure 57. The resulting modulus at 100% elongation (M100) test results are summarized in Table 25 and Figure 58. These show that the M100 in the post-run O-rings conditioned in Jet A_16 was significantly higher in the stressed O-rings as compared to the baseline O-rings. However, the variation with the aromatic content of the test fuels was mixed and relatively small suggesting that the aromatic content of

the test fuel did not have a significant influence on the stress/strain behavior of the O-rings materials. This implies that the molecular structure of the elastomers were not significantly effected by the aromatic content of the fuel and therefore did not have a significant effect on the aging of the test materials.

Table 25. Modulus at 100% Elongation

Fuel	Aromatics	Modulus @ 100% El, psi		
		N0602	N400	4457
None	n.a.	423	634	616
Jet A_4	4.0%	1595	1347	1295
Jet A_16	16.2%	1549*	1240	1275
Jet A_25	25.0%	1738*	1231	1330*

*Estimated

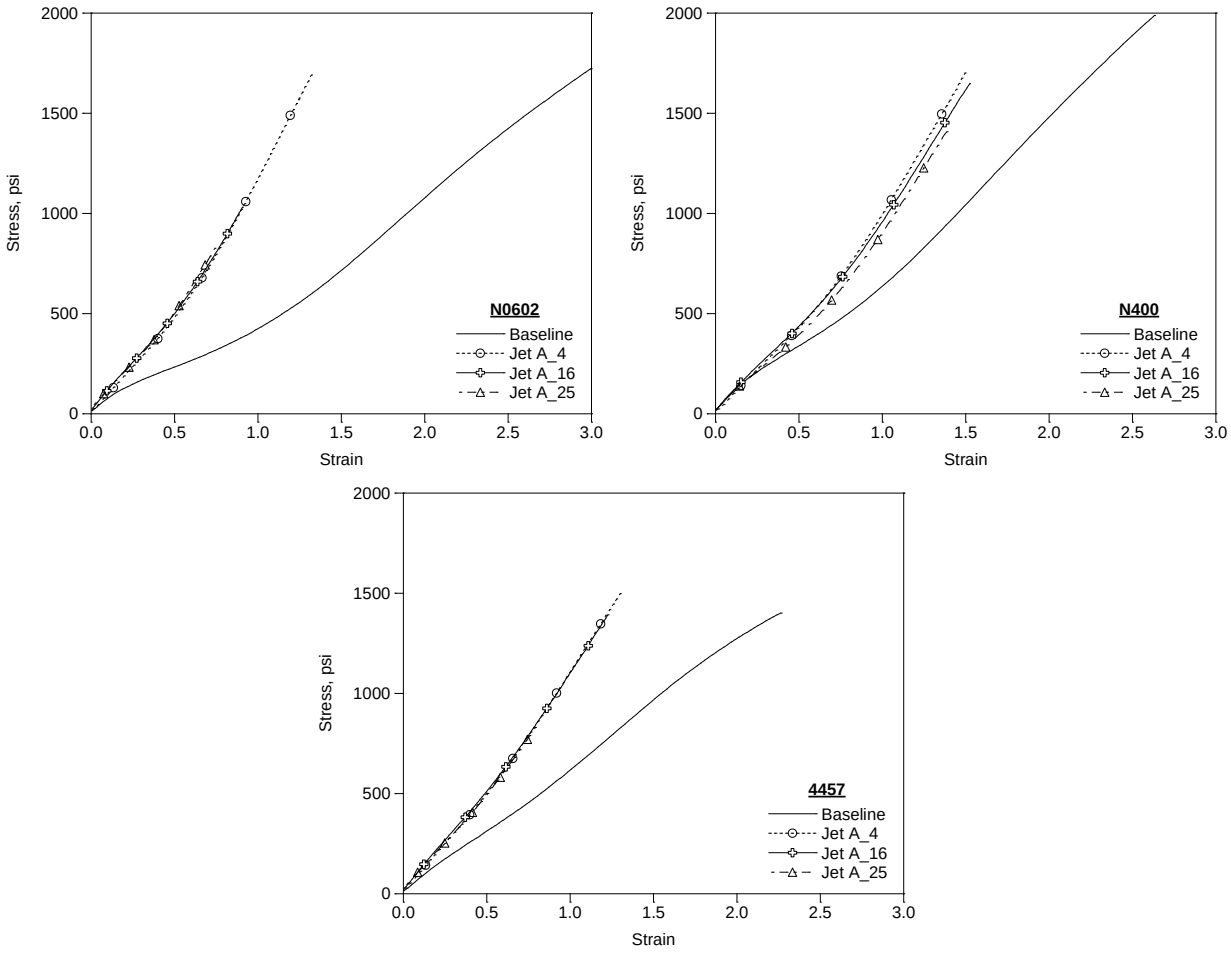

Figure 57. Summary of the post-compression set stress/strain along with the baseline stress/strain as measured in Task 1.

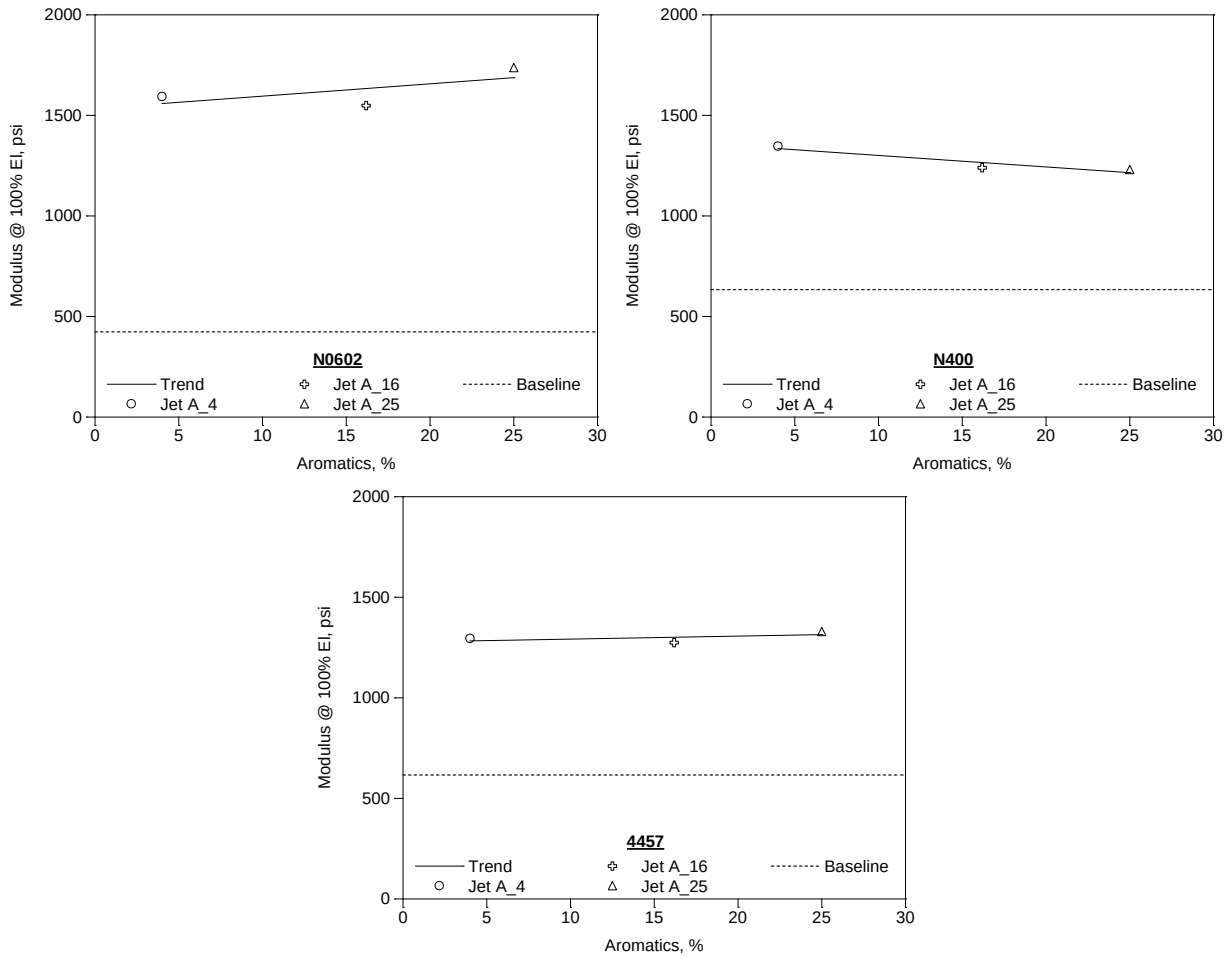

Figure 58. Summary of the post-compression set modulus measured at 100% elongation along with the baseline modulus as measured in Task 1.

O-ring Cross Sections

As described above, after the completion of the physical property tests 3 of the O-rings were returned to their respective test fuels for 2 weeks to return them to their post-compression set condition. This conditioned them for testing that reflected the engineering performance of the as-tested materials. For this task that was principally measuring the glass transition temperature as described below. Part of the sample prep for these measurements involved cutting small sections from one of the O-rings from each fuel and this provided an opportunity to photograph the O-rings cross sections as shown in Figure 59. This illustrates that while all the tested O-rings show a significant amount of compression set, visually they all appear to be very similar to each other. Also, note the characteristic "D" shape of the compressed O-rings where the outside face has been flattened by the outside radius of the glad. This shape is also seen in fully captured O-rings from face and pressurized piston seals where the rounded face is pushed away from the inside radius by the pressure of the fuel. This illustrates how the UDRI O-ring fixture stressed the O-rings in a manner similar to that of a typical compression seal.

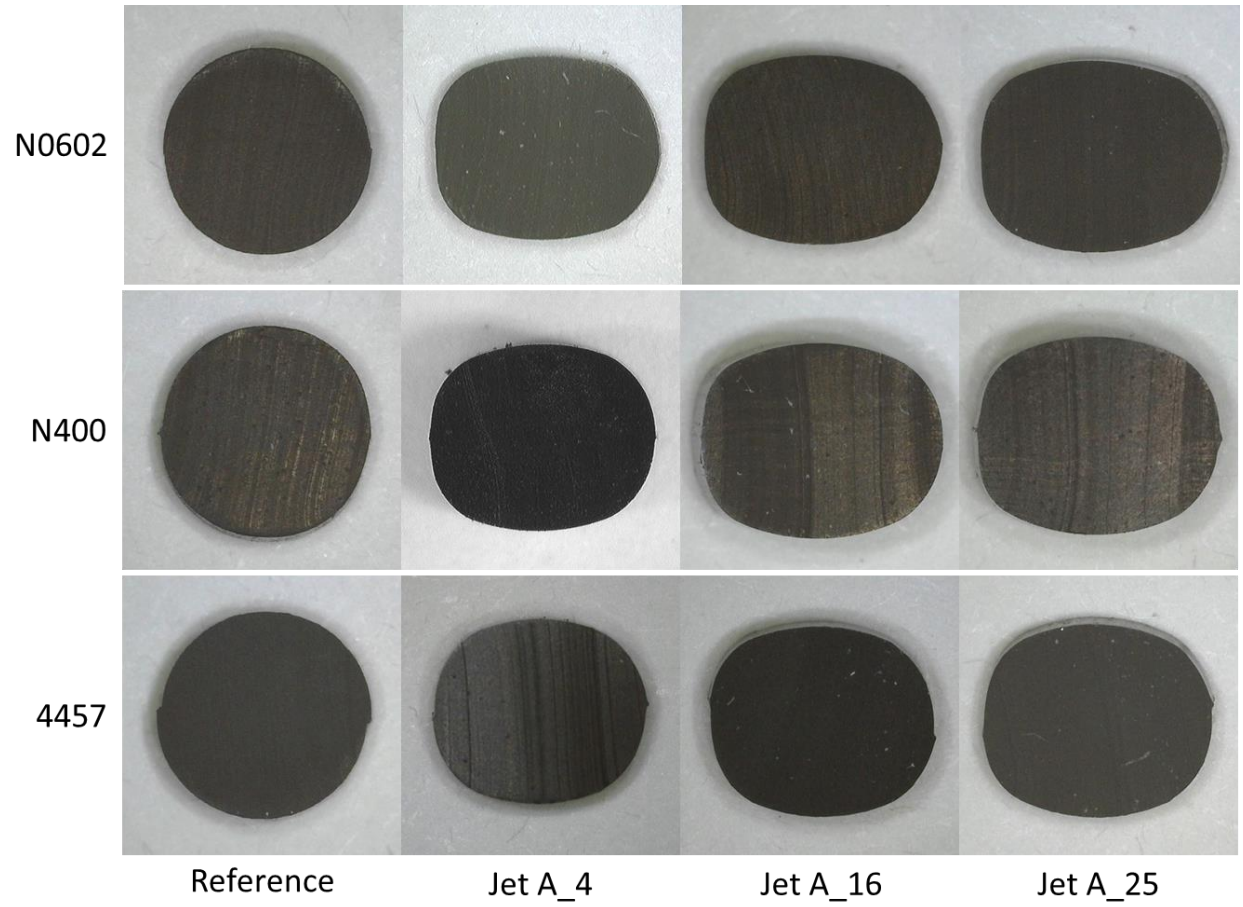

Figure 59. Photographs of the O-ring cross sections.

Glass Transition Temperature

The glass transition temperature (Tg) of the O-ring materials in their respective test fuels along with the baseline Tg values as measured in Task 1 are summarized in Table 26 and Figure 60. These show that the Tg of the post-run O-rings in their respective test fuels was lower than their baseline values and decreased with increasing aromatic content. This is consistent with the measured volume swell behavior of these materials with the Tg decreasing as the volume swell increases.

Table 26. Glass Transition Temperature of the As-Stressed O-rings

Fuel	Aromatics	Tg, ˚C		
		N0602	N400	4457
None	n.a.	-51.2	-49.5	-50.8
Jet A_4	4.0%	-54.6	-57.8	-55.5
Jet A_16	16.2%	-61.2	-64.5	-59.4
Jet A_25	25.0%	-66.1	-66.3	-64.3

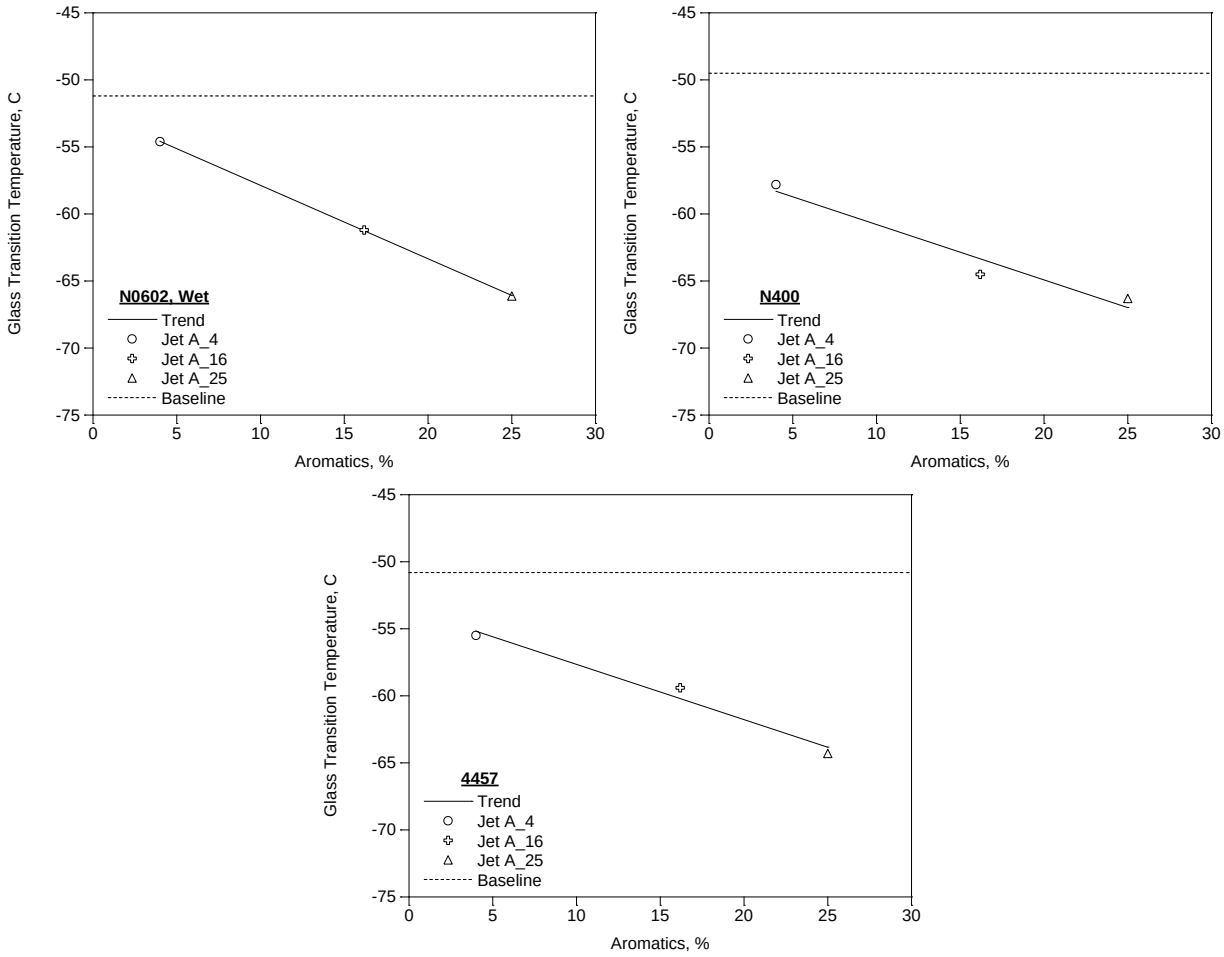

Figure 60. Summary of the post-compression set glass transition temperature of the O-ring materials in their respective test fuels along with the baseline values as measured in Task 1.

The Tg values for the O-ring materials after having been extracted using methylene chloride dried along with similarly prepared source materials are summarized in Table 27 and Figure 61. The process of extracting and drying these O-rings served to remove the fuel absorbed from the test materials and the plasticizer from the source materials so that the measured Tg values reflect the condition of the nitrile rubber without the presence of modifiers. Briefly, the test pieces were extracted in approximately 40 mL of methylene chloride for 24 hours. The solvent was decanted off, and the pieces were extracted for approximately 16 hours (overnight) with a fresh volume of solvent. This was also decanted off, and the process repeated a third time with the pieces being extracted for 4 hours. The solvent was decanted off, the test pieces were dabbed dry with a laboratory tissue and air dried at room temperature for 16 hours (overnight) and then for 60 minutes at 40°C in a forced convection oven. Prior work has shown that this process effectively removes any residual plasticizer, fuel, or solvent from the test pieces.

The tests results summarized in Table 27 and Figure 61 show that the Tg values of the post-run O-rings was slightly higher than the source materials, suggesting a slight reduction in the chain mobility possibly as a consequence of the chain ordering resulting from the viscoelastic flow and chain slip. It is interesting to note that the effect of test fuel an aromatic type is very small, suggesting that the effects of the SAF on the factors effecting Tg (chain mobility, cross-link density, etc.) would be nearly identical to conventional jet turbine fuel.

Table 27. Glass Transition Temperature of the Extracted & Dried O-rings

Fuel	Aromatics	Tg, C		
		N0602	N400	4457
None	n.a.	-44.9	-46.0	-45.6
Jet A_4	4.0%	-44.4	-42.3	-44.1
Jet A_16	16.2%	-44.2	-42.1	-45.3
Jet A_25	25.0%	-44.5	-41.1	-42.0

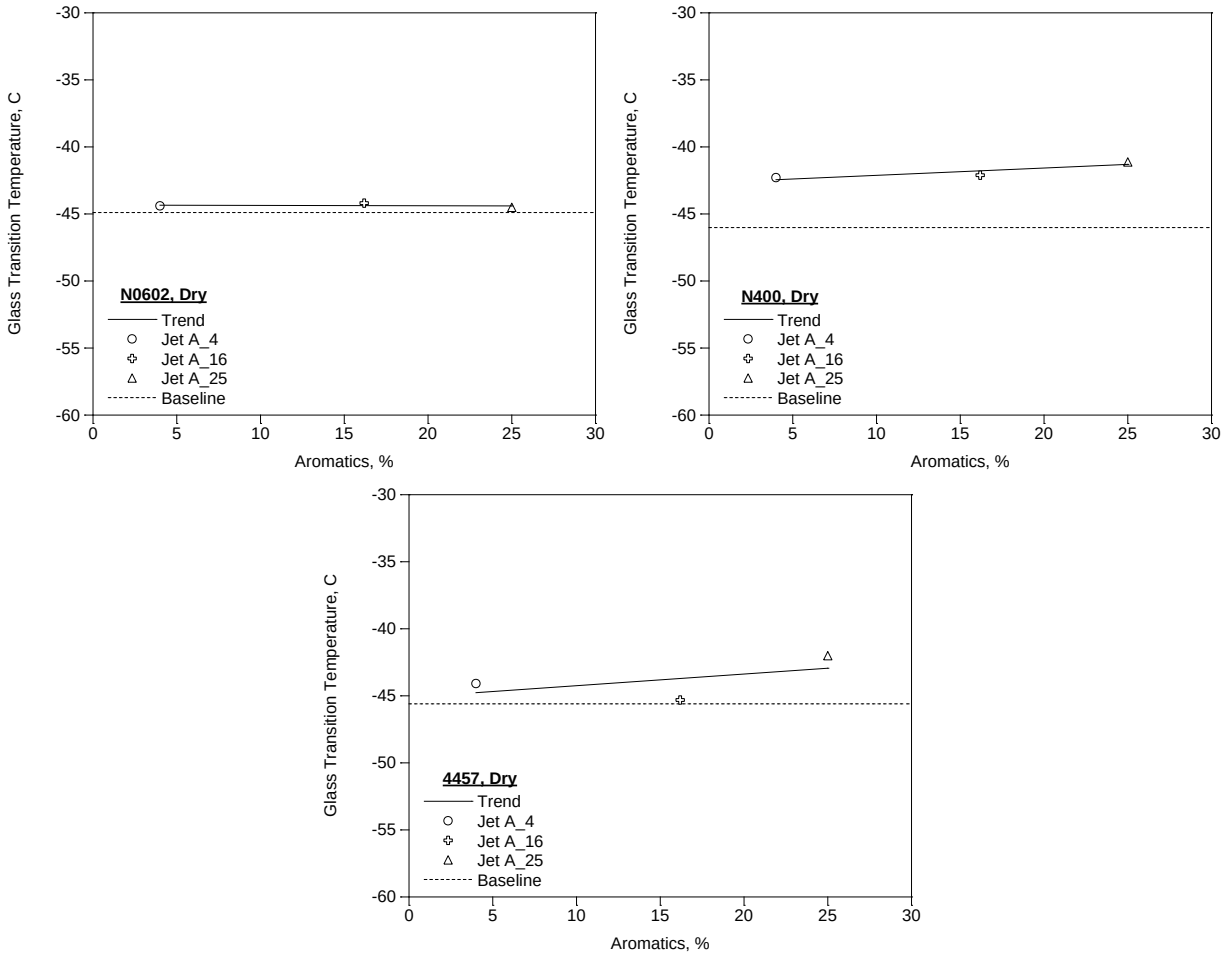

Figure 61. Summary of the post-compression set glass transition temperature of the O-ring materials after being extracted and dried along with the baseline values of the source materials.

Infrared Spectra

Infrared spectra were obtained for the source and test O-rings using a Fourier-transform infrared spectroscopy using a diamond micro-ATR crystal sampling technique in a manner similar to that used in Task 1. Samples were prepared as O-rings cross sections that were extracted with methylene chloride and dried to remove the absorbed fuel (and plasticizer from the source samples) and to condition the samples to a common state. Spectra were obtained from the cut face of each sample to access the cleanest possible elastomer in the bulk sample. The results are summarized in Figure 62. Overall, these show that the IR spectra from each sample is very similar. Unfortunately, these data do not show a clear absorption feature at ~2250 cm^{-1} that is characteristic of the –CN group, reflecting the challenge associated with obtaining quantitative IR spectra on commercially produced O-ring that are heavily filled with carbon black. However, these spectra suggest that the exposure to the different fuels had little, if any, effect on the bulk composition of the elastomer.

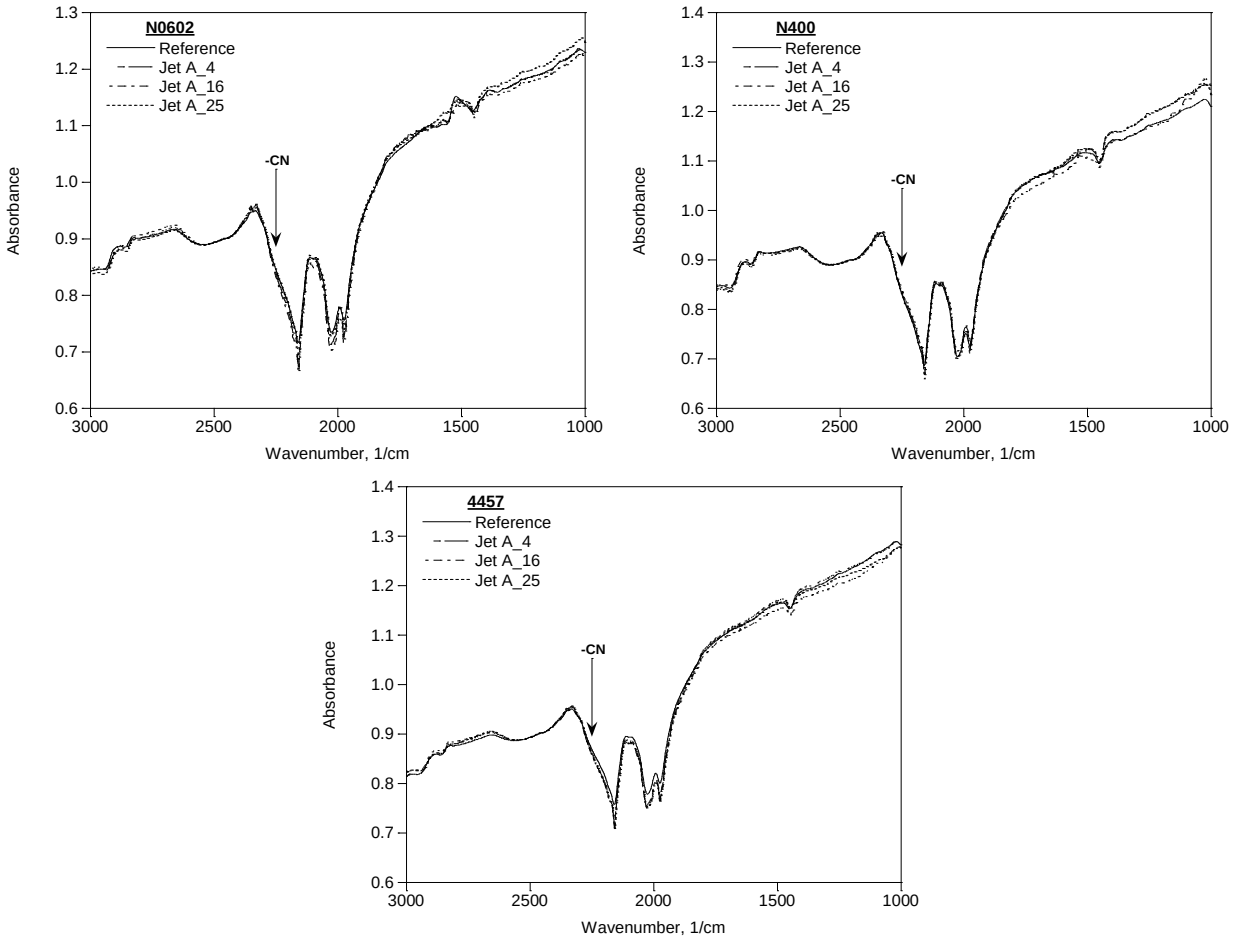

Figure 62. Summary of the post-compression set IR spectra of the O-ring materials after being extracted and dried along with the spectra of the source materials. The expected absorption region for the –CN group (~2250 cm^{-1}) is indicated.

Task 3 – Compression and Compression Set with fuel Switch-loading

In this task the compression and compression set was measured for selected test materials compressed 25% (nominal) in the UDRI compression fixtures (see Figure 1 above) at 160˚F while being exposed alternatively to Jet A_4 (4% aromatics) and Jet A_25 (25% aromatics). The compression and compression set were measured every 2 weeks over a period of 27 weeks in accordance with ASTM D395 with the variance that the UDRI fixtures were used.

The UDRI Compression set fixtures are shown in Figure 1. These fixtures are designed to constrain the test pieces in a manner comparable to that of an internally pressurized face seal. Specifically, compressed nominally 25% in the axial (vertical) direction with the outside diameter of the O-ring pressing up against the outside radius of the gland. The O-ring typically does not contact the inside radius of the gland, so this face has been removed from the fixture, allowing unrestricted access to the test fluid along the

O-ring's inner face in a manner comparable to an in-service condition.

Results and Discussion

The test results expressed in terms of compression is summarized in Table 28. For comparison the compression from Task 2 (single fuel exposure) are summarized in Table 29. These test results are combined in Figures 63-65 for the N0602, N400, and 4457 O-rings, respectively. The test results expressed in terms of compression set is summarized in Table 30. For comparison the compression set from Task 2 (single fuel exposure) are summarized in Table 31. These test results are combined in Figures 66-68 for the N0602, N400, and 4457 O-rings, respectively. Note that the compression set was calculated using the initial dry diameter of the O-rings as the reference state. Also note that the switch-loading point values were fit using a cubic spline model and the curves may not reflect the actual temporal behavior of the O-rings.

Overall, the test results from Task 2 and Task 3 suggest that switch-loading did not have a significant effect on the rates of the accumulation of compression set and the loss of compression when compared to Task 2 static conditions. While there is some slight variation, it is not consistent between the test materials. For example, the N0602 and N400 show a slight increase in compression set during the switch-loading as compared to the single fuel exposures, while the 4457 shows a slight decrease in set, and these small variances may be within the variability of the test and materials. This suggests that the fuel switching does not alter the chemical or physical condition of the O-rings and that their behavior is similar to that of a state function and that the O-rings respond to their current environment and are not influenced by their prior exposure to fuels of varying composition as long as those fuels are non-reactive.

Table 28. Switch-load Compression, %

	N0602		N400		4457	
Weeks	Jet A_4	Jet A_25	Jet A_4	Jet A_25	Jet A_4	Jet A_25
0 (Dry)	23.8	23.8	23.7	23.7	24.5	24.5
2		22.5		22.1		22.1
4	17.8		17.3		18.5	
6		20.1		19.9		20.5
8	15.8		15.5		17.3	
10		18.0		18.1		19.1
12	14.1		14.2		16.4	
15		15.6		16.4		17.4
17	11.6		12.3		12.3	
19		14.2		15.2		16.2
21	10.6		11.5		11.5	
23		13.2		14.4		15.6
25	9.4		10.7		10.7	
27		12.0		13.5		14.5

Table 29. Single Fuel Compression, % (Task 2)

	N0602		N400		4457	
Weeks	Jet A_4	Jet A_25	Jet A_4	Jet A_25	Jet A_4	Jet A_25
0 (Dry)	23.9	23.9	23.8	23.7	24.4	24.4
2	18.5	21.8	18.6	21.7	18.5	21.2
4	17.1	21.1	17.4	20.8	17.5	20.6
6	16.3	20.4	16.4	20.1	17.1	20.2
8	14.9	19.5	15.4	19.5	16.1	19.4
10	14.1	18.8	14.6	18.7	15.7	18.9
12	13.5	18.4	14.2	18.3	15.2	18.3
14	12.6	17.6	13.6	17.6	14.5	17.7
16	11.9	16.8	12.8	16.8	13.9	16.9
18	11.4	16.2	12.3	16.4	13.6	16.4
20	11.2	15.8	12.2	16.0	13.4	15.9
22	10.4	14.9	11.4	15.3	12.8	15.1
24	10.3	14.4	11.2	15.0	12.4	14.6
26	9.7	13.6	10.8	14.4	12.0	14.1

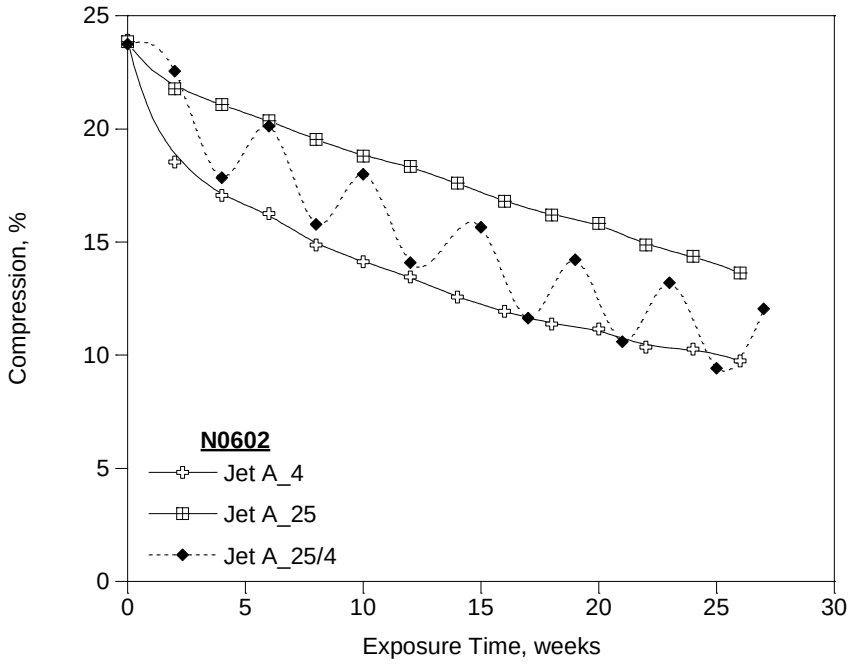

Figure 63. Compression as a function of time for N0602 O-rings when exposed to a single fuel (Task 2) and periodically switched between Jet A_4 and Jet A_25. Note that the switch-load data points are joined using a cubic spline fit and this curve may not reflect the true temporal behavior.

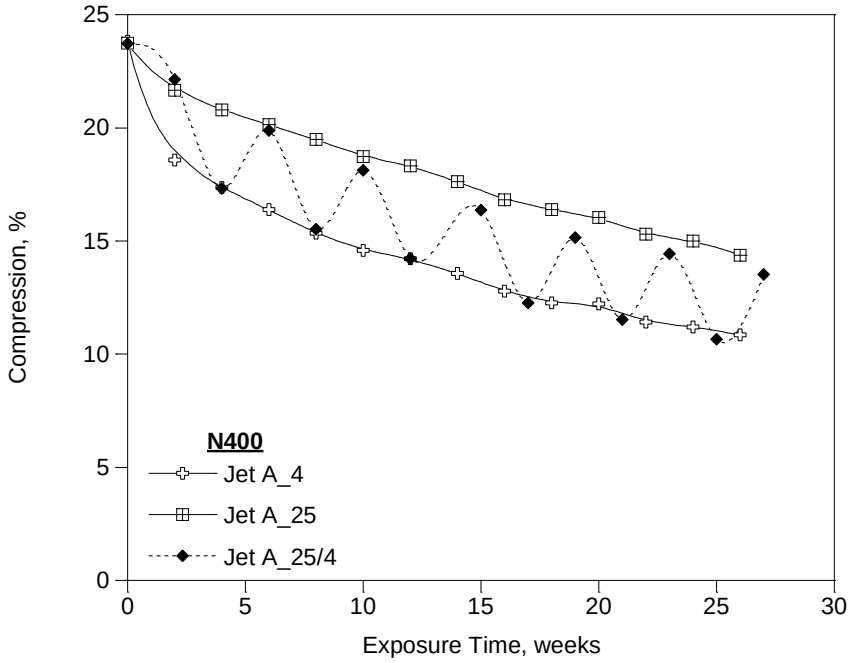

Figure 64. Compression as a function of time for N400 O-rings when exposed to a single fuel (Task 2) and periodically switched between Jet A_4 and Jet A_25. Note that the switch-load data points are joined using a cubic spline fit and this curve may not reflect the true temporal behavior.

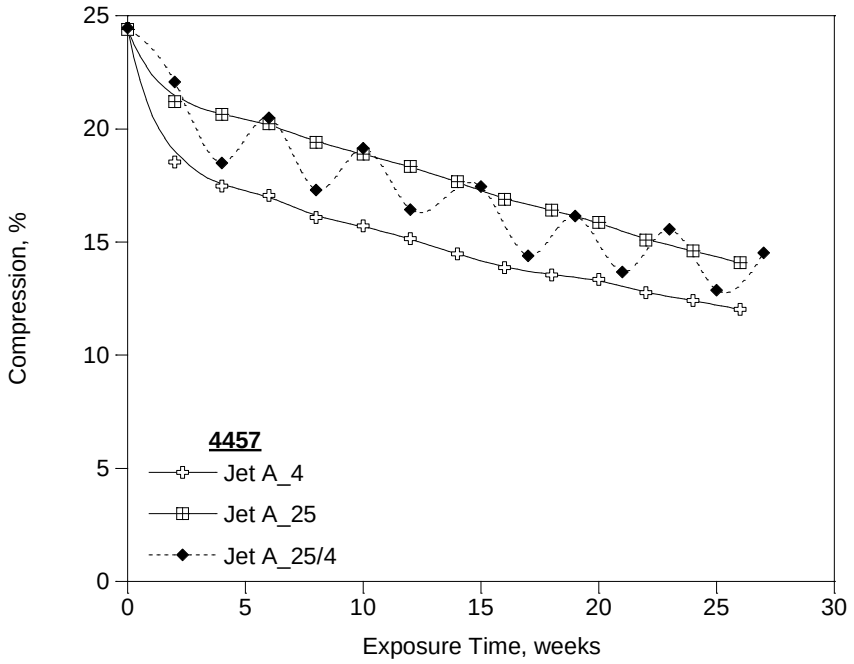

Figure 65. Compression as a function of time for 4457 O-rings when exposed to a single fuel (Task 2) and periodically switched between Jet A_4 and Jet A_25. Note that the switch-load data points are joined using a cubic spline fit and this curve may not reflect the true temporal behavior.

Table 30. Switch-load Compression Set, %

	N0602		N400		4457	
Weeks	Jet A_4	Jet A_25	Jet A_4	Jet A_25	Jet A_4	Jet A_25
0	0.0	0.0	0.0	0.0	0.0	0.0
2		6.5		8.5		12.6
4	30.2		32.6		30.0	
6		19.1		20.2		20.4
8	39.8		40.9		35.4	
10		29.4		28.8		26.9
12	47.3		46.6		39.3	
15		40.4		37.1		34.7
17	57.7		55.1		55.1	
19		46.8		42.6		40.5
21	61.9		58.1		58.1	
23		51.2		45.8		43.1
25	66.5		61.6		61.6	
27		56.0		49.7		47.5

Table 31. Single Fuel Compression Set, % (Task 2)

	N0602		N400		4457	
Weeks	Jet A_4	Jet A_25	Jet A_4	Jet A_25	Jet A_4	Jet A_25
0	0.0	0.0	0.0	0.0	0.0	0.0
2	27.6	11.0	27.0	11.1	29.6	16.6
4	34.5	14.7	32.8	15.7	34.5	19.5
6	38.2	18.3	37.4	19.0	36.4	21.4
8	44.3	22.4	42.0	22.2	40.7	25.4
10	47.6	26.0	45.4	25.9	42.4	27.9
12	50.5	28.1	47.0	27.9	44.8	30.4
14	54.3	31.8	49.8	31.2	47.7	33.6
16	56.8	35.4	53.1	35.1	50.2	37.1
18	59.1	38.2	55.3	37.0	51.5	39.2
20	60.0	39.9	55.5	38.6	52.3	41.6
22	63.2	44.2	58.8	41.9	54.8	44.9
24	63.5	46.3	59.7	43.3	56.2	47.0
26	65.6	49.6	61.1	46.1	57.7	49.2

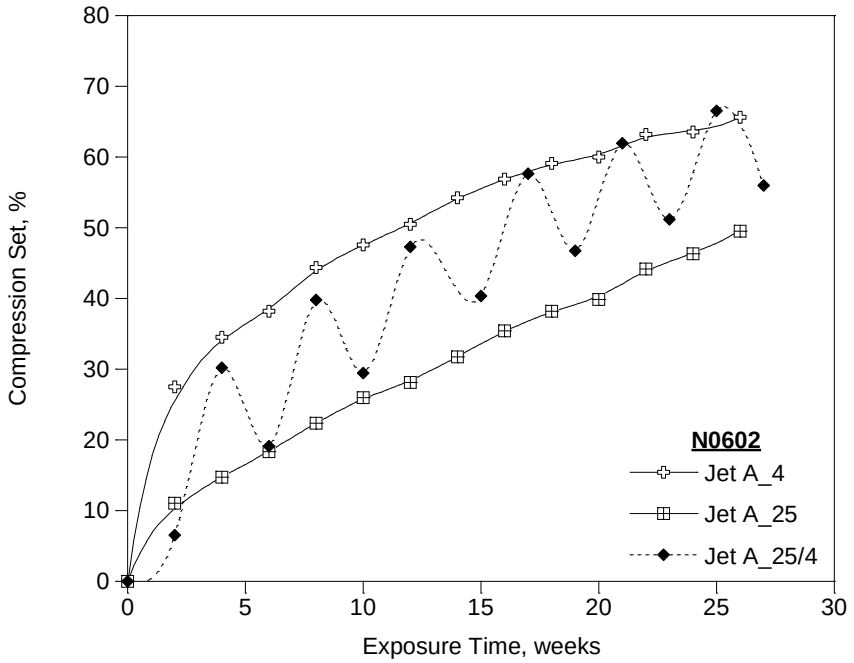

Figure 66. Compression set as a function of time for N0602 O-rings when exposed to a single fuel (Task 2) and periodically switched between Jet A_4 and Jet A_25. Note that the switch-load data points are joined using a cubic spline fit and this curve may not reflect the true temporal behavior.

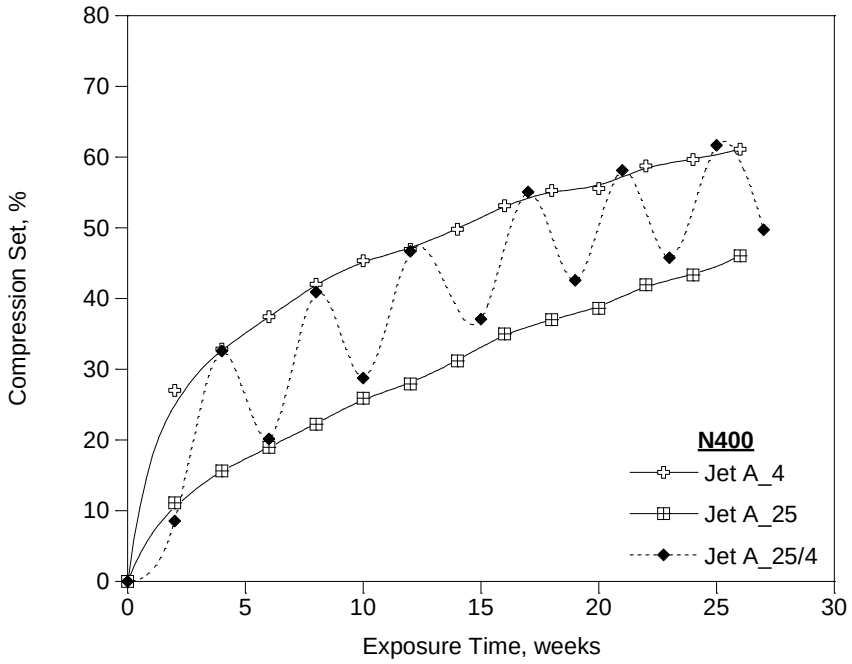

Figure 67. Compression as a function of time for N400 O-rings when exposed to a single fuel (Task 2) and periodically switched between Jet A_4 and Jet A_25. Note that the switch-load data points are joined using a cubic spline fit and this curve may not reflect the true temporal behavior.

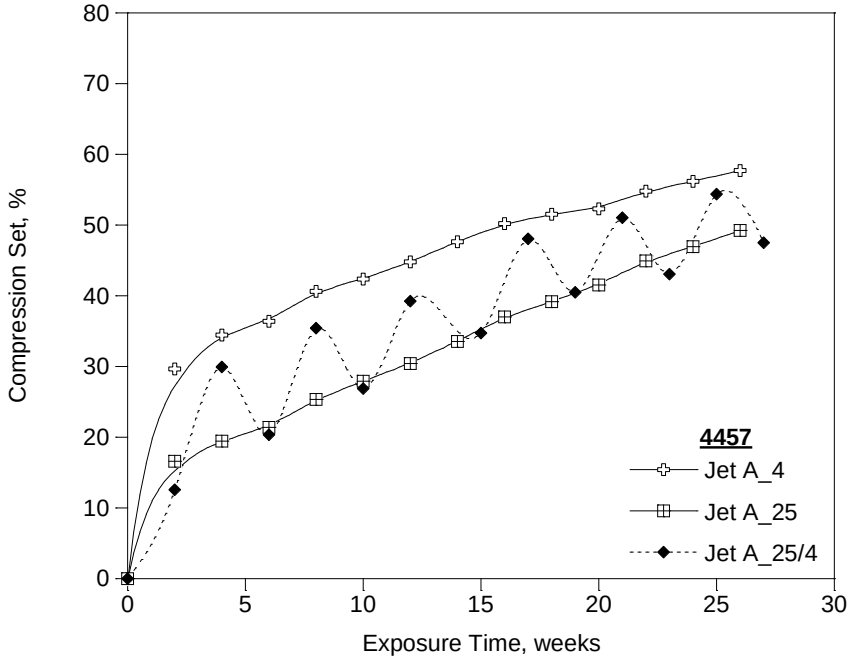

Figure 68. Compression as a function of time for 4457 O-rings when exposed to a single fuel (Task 2) and periodically switched between Jet A_4 and Jet A_25. Note that the switch-load data points are joined using a cubic spline fit and this curve may not reflect the true temporal behavior.

Post-Run Physical Properties

After the completion of the compression set evaluation selected physical properties were measured as summarized in Table 32. To condition the O-rings into a common state the test pieces were removed from their respective test fuels, dabbed dry with a laboratory tissue, and placed in Jet A_16 for 1 week at room temperature. The O-rings were then removed from the Jet A_16, dabbed dry, and placed in a fresh volume of Jet A_16 for an additional week. The test pieces were stored in Jet A_16 until their post-run testing was conducted.

Table 32. Task 3 Post-Run Set Tests

Property	Method	Notes
Hardness, Type M	ASTM D2240	Shore M
Tensile	ASTM D1414	Tensile Strength
Elongation	ASTM D1414	Ultimate Elongation
Modulus at 100% Elongation	ASTM D1414	Concurrent with ASTM D1414
IR Spectrum	ATR	Attenuated Total Reflectance
Glass Transition	ASTM E1545	Thermomechanical Analysis

Hardness

The type M hardness test results are summarized in Table 33 and Figure 69. Note that the O-rings from Task 1 were the dry source O-rings, while the O-rings from Task 2 were tested and conditioned in Jet A_16 in the same manner as the O-rings from Task 3. These show that the hardness of the N400 O-rings was relatively constant across Tasks 1-3 while the hardness of the N0602 and 4457 O-rings increased slightly across Tasks 2 and 3 and compared to the baseline Task 1.

Table 33. Type M Hardness

Source	Hardness, Type M		
	N0602	N400	4457
Task 1	77	79	77
Task 2	79	78	79
Task 3	81	79	81

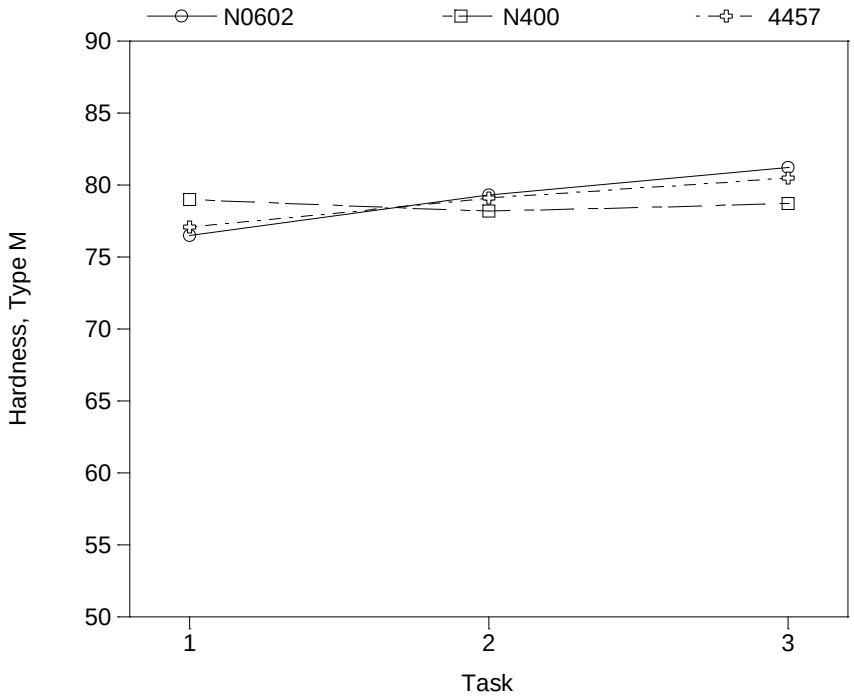

Figure 69. Summary of the post-compression set Type M hardness as measured in Task 1, 2, and 3.

Tensile

The tensile test results are summarized in Table 34 and Figure 70. Note that the O-rings from Task 1 were the dry source O-rings, while the O-rings from Task 2 were tested and conditioned in Jet A_16 in the same manner as the O-rings from Task 3. These show that the tensile of the 4457 O-rings was relatively constant across Tasks 1-3 while the tensile of the N0602 and 4457 O-rings was somewhat variable across Tasks 2 and 3 and compared to the baseline Task 1.

Table 34. Tensile

	Tensile, psi		
Source	**N0602**	**N400**	**4457**
Task 1	1757	1937	1429
Task 2	1203	1618	1507
Task 3	1884	1904	1429

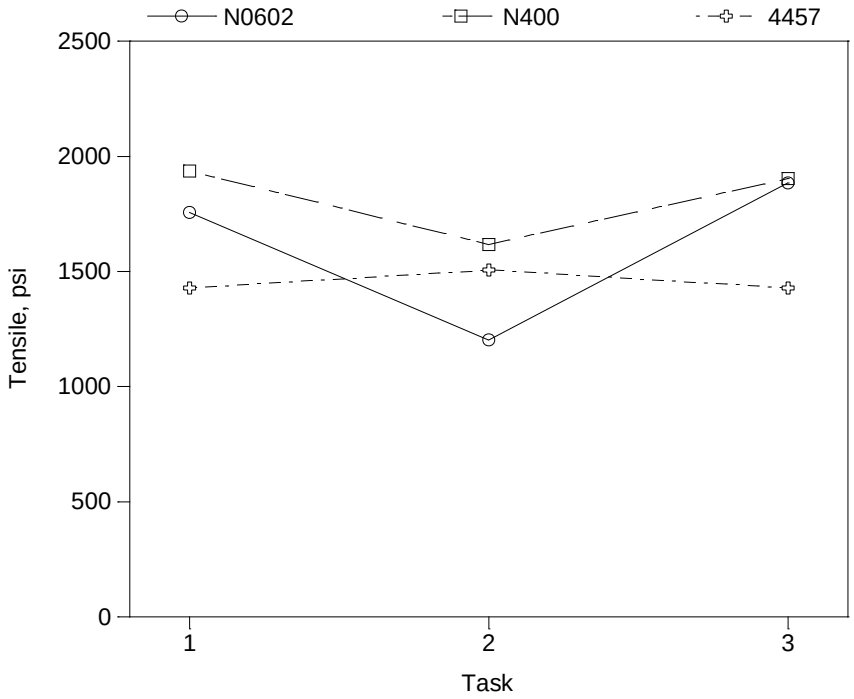

Figure 70. Summary of the post-compression set tensile as measured in Task 1, 2, and 3.

Elongation

The elongation test results are summarized in Table 35 and Figure 71. Note that the O-rings from Task 1 were the dry source O-rings, while the O-rings from Task 2 were tested and conditioned in Jet A_16 in the same manner as the O-rings from Task 3. These show that the elongation of the O-rings was lower following Tasks 2 and 3 as compared to the baseline Task 1 while the values following Tasks 2 and 3 were comparable to each other.

Table 35. Elongation

	Elongation, %		
Source	**N0602**	**N400**	**4457**
Task 1	308	255	234
Task 2	103	150	132
Task 3	124	168	119

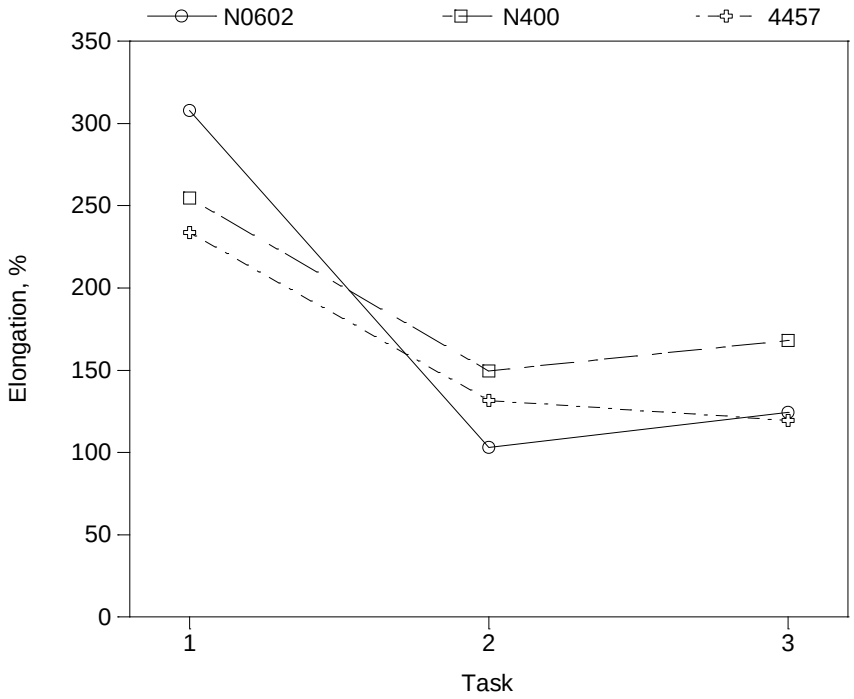

Figure 71. Summary of the post-compression set elongation as measured in Task 1, 2, and 3.

Modulus at 100% Elongation

The modulus at 100% elongation, M(100), test results are summarized in Table 36 and Figure 72. Note that the O-rings from Task 1 were the dry source O-rings, while the O-rings from Task 2 were tested and conditioned in Jet A_16 in the same manner as the O-rings from Task 3. These show that the M(100) of the O-rings was higher following Tasks 2 and 3 as compared to the baseline Task 1 while the values following Tasks 2 and 3 were comparable to each other.

Table 36. Modulus at 100% Elongation

	Modulus at 100% Elongation		
Source	**N0602**	**N400**	**4457**
Task 1	474	728	680
Task 2	1549	1240	1275
Task 3	1610	1234	1248

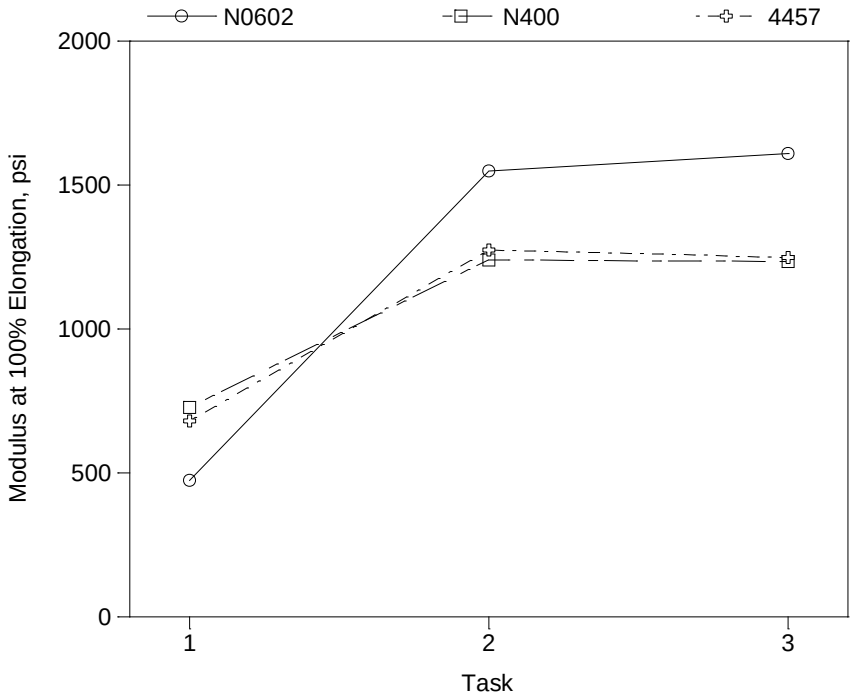

Figure 72. Summary of the post-compression set modulus at 100% elongation as measured in Task 1, 2, and 3.

Glass Transition Temperature, Tg

The glass transition temperature (Tg) of the source, as-received O-ring materials (no conditioning) and the test O-rings from Task 2 and 3 after being conditioned in Jet A_16 are summarized in Table 37 and Figure 73. These results show how the Tg was lower for the test O-rings conditioned in Jet A_16 as compared to the original source O-rings as expected due to the net volume swell of these materials with the commensurate plasticizing effects of the absorbed fuel.

Table 37. Glass Transition Temperature of the Test O-rings Conditioned in Jet A_16

	Tg, C		
Source	**N0602**	**N400**	**4457**
Reference*	-51.2	-49.5	-50.8
Task 2	-61.2	-64.5	-59.4
Task 3	-62.1	-63.0	-59.7

*As received, no conditioning

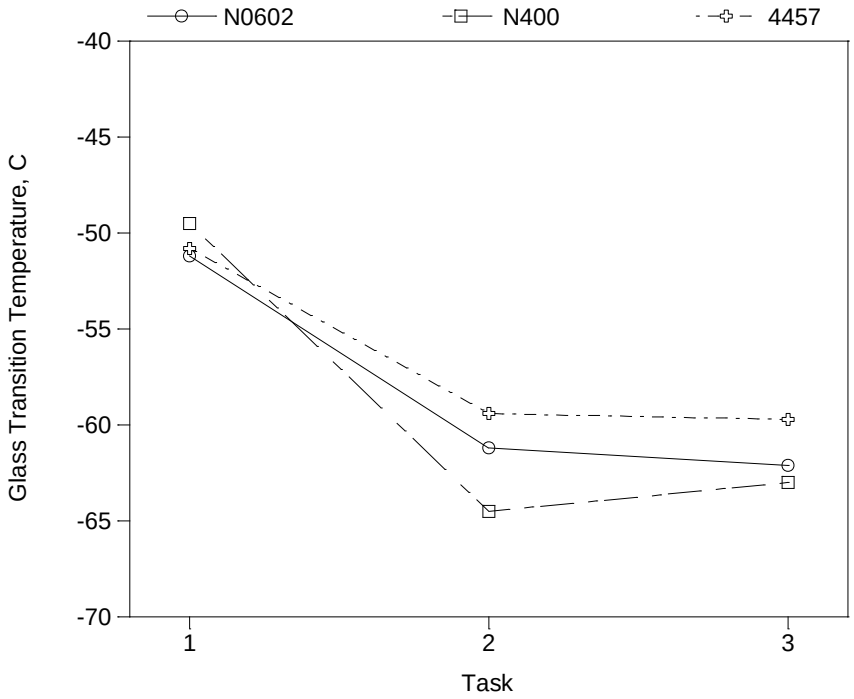

Figure 73. Summary of the post-compression set glass transition temperature as measured in Task 1, 2, and 3.

The glass transition temperature (Tg) of the source, as-received O-ring materials and the test O-rings from Task 2 and 3 after being extracted with methylene chloride and dried are summarized in Table 38 and Figure 74. This drying process was used to remove all of the plasticizer and absorbed fuel, giving the Tg of the elastomer itself without any interference from absorbed species. These results show how the Tgs for the test O-rings from Tasks 2 and 3 are similar to each other and to the source O-rings, suggesting that the aging of these O-rings in Tasks 2 and 3 did not have a significant effect on the molecular structure of the elastomer.

Table 38. Glass Transition Temperature of the Test O-rings Extracted & Dried

	Tg, C		
Source	**N0602**	**N400**	**4457**
Reference	-44.9	-46.0	-45.6
Task 2	-44.2	-42.1	-42.0
Task 3	-44.8	-43.5	-44.6

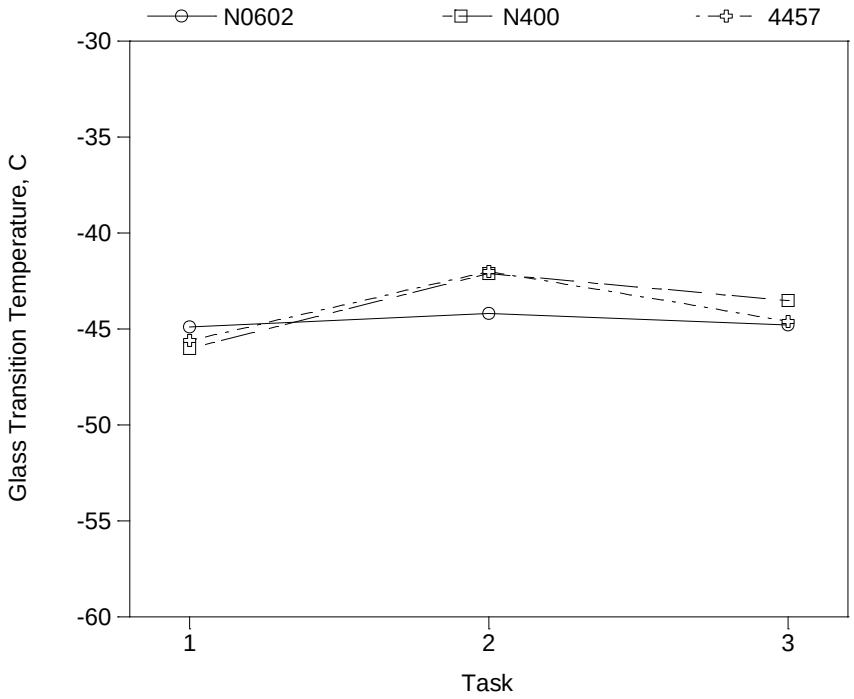

Figure 74. Summary of the post-compression set glass transition temperature as measured in Task 1, 2, and 3.

Infrared Spectra

Infrared spectra were obtained for the source and test O-rings using a Fourier-transform infrared spectroscopy using a diamond micro-ATR crystal sampling technique in a manner similar to that used in Task 1. Samples were prepared as O-rings cross sections that were extracted with methylene chloride and dried to remove the plasticizer from the source samples and the fuel absorbed by the test materials, conditioning the samples to a common state. Spectra were obtained from the cut face of each sample to access the cleanest possible elastomer in the bulk sample. The results are summarized in Figure 75. Overall, these show that the IR spectra from each sample is very similar. Unfortunately, these data do not show a clear absorption feature at ~2250 cm^{-1} that is characteristic of the –CN group, reflecting the challenge associated with obtaining quantitative IR spectra on commercially produced O-ring that are heavily filled with carbon black. However, these spectra suggest that the exposure to the switch-loading had little, if any, effect on the bulk composition of the elastomer.

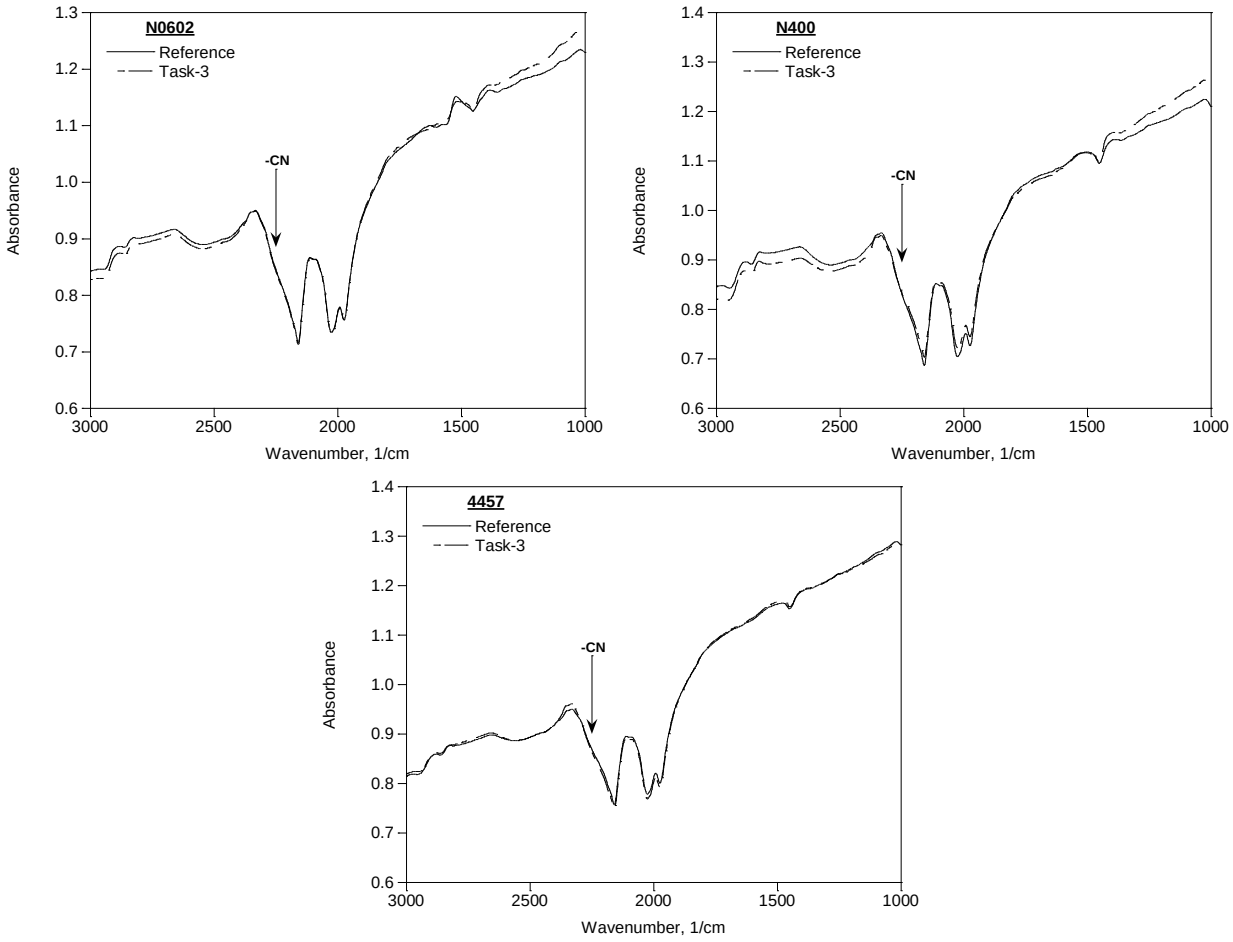

Figure 75. Summary of the post-compression set IR spectra of the O-ring materials after being extracted and dried along with the spectra of the source materials. The expected absorption region for the –CN group (~2250 cm^{-1}) is indicated.